2019

Nuclear properties with effective operators

Robert A. M. Basili
Iowa State University

Nuclear properties with effective operators

by

Robert A. M. Basili

A dissertation submitted to the graduate faculty

in partial fulfillment of the requirements for the degree of

DOCTOR OF PHILOSOPHY

Major: Nuclear Physics

Program of Study Committee:
James P. Vary, Co-major Professor
Pieter Maris, Co-major Professor
John M. Hauptman
James I. Lathrop
Kirill Tuchin

The student author, whose presentation of the scholarship herein was approved by the program of study committee, is solely responsible for the content of this dissertation. The Graduate College will ensure this dissertation is globally accessible and will not permit alterations after a degree is conferred.

Iowa State University

Ames, Iowa

2019

DEDICATION

To my mom and dad, for all you have done
To help me to learn and grow.
For putting up with such a goofy son-
The one who oft goes by Bo.

Now my thesis is done and comes in view,
So for all who'll care to see,
I would write this work is my gift to you,
Were it not your gift to me.

TABLE OF CONTENTS

Page

LIST OF TABLES

LIST OF FIGURES

ACKNOWLEDGMENTS

I express my sincere gratitude to those who helped me conduct this research and prepare this thesis. I thank Dr. James P. Vary and Dr. Pieter Maris, for their support, guidance, and unwavering patience throughout my research here at Iowa State University. Dr. Vary's relentless encouragement has inspired me to never stop improving myself, not just as a physicist but as a person, and Dr. Maris's level-headed guidance has taught me the importance of staying focused on achievable goals. I would also like to thank Dr. John Hauptman for his guidance throughout the initial stages of my graduate career, and my other committee members, Dr. Kirill Tuchin and Dr. James Lathrop, for the lessons they taught me and the elegant teaching styles by which they did so. I would additionally like to thank my fellow members of the Iowa State Nuclear Structure group for their hard work and aid in developing both this research and my own understanding. Dr. Hugh Potter and Dr. Weijie Du were instrumental in the development of the two-nucleon codes, and Matthew Lockner provided very helpful guidance on certain technical aspects of using supercomputing resources at NERSC. Soham Pal and Shiplu Sarker were similarly critical to the development and study of SRG, as well as deriving electroweak current operators under Chiral Effective Field Theory. I further extend my gratitude to Dr. Mark Caprio and Patrick Fasano of the University of Notre Dame, Dr. Jon Engel of the University of North Carolina, and Dr. Jiangming Yao and Dr. Heiko Hergert of Michigan State University, for their pivotal support throughout both the collaborative projects considered here and others that are presently underway. I offer my appreciation to the librarians at Iowa State for their guidance, review, and publishing of this work. It has been and continues to be a true honor working with everyone, and I am proud to be a part of such fulfilling work. Thank you.

ABSTRACT

Recent developments in theoretical Nuclear Physics offer new effective tools that improve the predictive power of modern low-energy Nuclear Structure. Specifically, the high-quality results achievable with *ab initio* methods allow us to test our knowledge of the strong interaction and to quantify the uncertainty in that knowledge. We review the progress and challenges of Nuclear Structure up to the present and perform uncertainty studies for several modern methods being developed to improve current solutions to the nuclear many-body problem. The *ab initio* No-Core Shell Model (NCSM) approach is employed throughout this study, though much of the discussion relates to other *ab initio* approaches as well.

We demonstrate the effects of basis truncation on the approximation of two-nucleon (2N) wavefunctions and observables in a relative Harmonic Oscillator (HO) basis, and investigate two approaches for matrix renormalization. We illustrate the effects of Okubo-Lee Suzuki renormalization on 2N observables for the root-mean-square point-proton radius, electric quadrupole moment, magnetic dipole moment, Gamow-Teller transition and neutrinoless double-beta decay operator using nucleon-nucleon interactions from Chiral Effective Field Theory (χEFT), both with and without a confining HO trap. We examine the 2N observables at each chiral order of the potential, verify agreement with experiment to at least a few percent (where applicable), and set the stage for comparing the results to a theoretically consistent χEFT-treatment in a future study. Renormalization effects tend to be largest in the weaker traps and smaller basis spaces, suggesting applications to heavier nuclei with transitions dominated by weakly-bound nucleons would be subject to more significant renormalization effects.

In another study, we use the NCSM approach to benchmark the results of the Multi-Reference In-Medium Similarity Renormalization Group (MR-IMSRG) approach when calculating the matrix elements of neutrinoless double-beta decay mediated by light Majorana neutrino exchange in a light

nucleus. The goal is to identify the MR-IMSRG approach as a possible candidate for calculating the decay's matrix elements in heavy nuclei. We compare results of the two approaches as a function of the basis cutoffs, and determine their predictions through extrapolation. Differences between the two approaches are observed for the square nuclear radii, and signal the effects of correlations that are omitted by the MR-IMSRG(2) truncation at the two-body level. The ground-state energies and neutrinoless double-beta decay matrix elements show good agreement, and the implications for calculations in heavier nuclei are discussed.

CHAPTER 1. INTRODUCTION

This work is centered around performing *ab initio* (i.e. "from the beginning") Nuclear Structure calculations, where the goal is to solve the Nuclear Many-Body Problem (NMBP) in a way that preserves the predictive power of realistic inter-nucleon interactions. In particular, we focus on these calculations as they are done via the No-Core Shell Model (NCSM). Several aspects of the model approach and formalism, as well as tools to support its performance, are discussed, and examples of their implementation and results are provided. A broad description of both Nuclear Structure calculation and the challenges posed by the NMBP are also discussed.

The field of Nuclear Physics is witnessing rapid development in multiple directions. The end of the 20th century saw several key developments in understanding the nature of scale in physical models, and significant progress has been made in the implementation of these ideas. The development of Effective Field Theory (EFT) and, consequently, Chiral EFT (χEFT) has opened a path towards a realistic description of the nuclear interaction. Despite a number of formidable challenges, χEFT has seen rapid advancement in the past decade, and the development of realistic two-nucleon (2N) interactions with roots in Quantum Chromodynamics (QCD) continues to progress. χEFT also opens new possibilities for defining a realistic three-nucleon (3N) interaction, a subject that has otherwise remained poorly understood and limited by the available data. What's more, χEFT provides for all levels of the interaction (2N, 3N, etc.), along with the operators describing other observables to be defined within a consistent theoretical treatment.

The benefits of these developments are manifold. On the one hand, it is thought that the current differences between theoretical modeling results and experiment could be explained by the adoption of a χEFT treatment. On the other hand, discrepancies that remain despite such a treatment could lead to the discovery of further improvements or perhaps even new physics. In a broader sense, χEFT also offers a path to validate the governing theory (i.e. QCD) in ways never before

possible, and may provide meaningful QCD-roots to effective models that otherwise primarily rely on phenomenological descriptions.

The developments provided by EFT are not the only form of significant recent progress. Several methods for reducing the complexity of Nuclear Structure approaches (and consequently for increasing the range of nuclei they can meaningfully model) have been developed, as well as other, entirely new approaches to the NMBP.

Coupled with the constant improvements of computer technology and the adaptation of Nuclear Structure methods to their rapid development, the need for efficiently evaluating, benchmarking, and validating the results and codes of both new and venerable modeling approaches and tools has grown ever more important in recent years. The computational requirements of *ab initio* solutions to the NMBP grow rapidly with nucleon count, and while this does not prevent their use for testing methods, the consideration of the general many-body problem can make such tests unwieldy and stifle the investigation of these tools.

However, the problem becomes far more manageable in the two-nucleon (2N) system, where only a single Jacobi coordinate is required for effective modeling. Thus, to aid in the development and validation of these new effective interactions, operators, and tools, it is helpful to first explore their implementation in the 2N system before considering the computationally-demanding calculations required by larger systems. The following work reflects both studies benchmarking the methods of *ab initio* calculation, as well as the development and implementation of a specialized 2N NCSM framework used for testing and diagnostic purposes.

The discussion will proceed as follows. In the remainder of the introduction, we will establish the context of Nuclear Structure by considering its history and define both its modern perspective and the NMBP. In Chapter 2 we define the formalism of the NCSM calculations performed in this work. We proceed to define and discuss the finer details of basis regularization inherent to the NCSM process as well as some techniques by which we may correct it in Chapter 3. With the groundwork complete, we next include a published work regarding the implementation of OLS renormalization in the two-nucleon system using a recently constructed χEFT potential in Chapter 4. From there

we consider a separate benchmark study currently under review by a journal that compares results from the NCSM and Multi-Reference In-Medium Similarity Renormalization Group (MR-IMSRG) approaches when calculating a hypothetical neutrinoless double-beta decay in a light nucleus in Chapter 5. Finally, we provide our conclusions and closing remarks in Chapter 6.

For the remainder of the introduction, we begin with an overview of Nuclear Structure's historical developments in Section 1.1 to provide context to the subsequent discussion. This leads us to a brief description of *ab initio* Nuclear Structure in Section 1.3. We conclude the introduction by briefly describing the NMBP in Section 1.4.

1.1 Brief history of Nuclear Structure

We briefly outline the history and development of Nuclear Structure, to address the varied problems and methods that define it. See the corresponding sections of Ref. [1] for a comprehensive review of the theoretical development, and Ref. [2] for the development of the various Nuclear Structure approaches used to define it. Throughout, our discussion follows two closely entwined narratives: the development of the effective inter-nucleon interaction, and the development of Nuclear Structure approaches used to solve the NMBP.

We begin with the foundations of the nucleus and other components contributing to the NMBP in Subsection 1.1.1. We follow with the development of the first Nuclear Structure models in Subsection 1.1.2. This leads our discussion to the development of Nuclear Structure calculation in Subsection 1.1.3, and modern efforts of developing a realistic, effective nuclear interaction in Subsection 1.1.4.

1.1.1 Foundations of the nuclear paradigm

The NMBP possesses a long history, containing components that span a great swath of historical developments. The description of a classical many-body problem using solely a two-body interaction dates back to Newton's theory of gravity near the end of the 17th century, and was found to successfully predict the motion of celestial bodies to very high precision. The method involves

treating the net force acting on a single body to be the additive sum of all forces between that body and every other individual body in the system. The same principle is valid for descriptions of many-body systems subject to the Coulomb interaction of Maxwell's theory of electromagnetism in the 19th century.

However, near the end of the 19th century, it was observed that, unlike Newtonian Mechanics, Maxwell's equations did not display Galilean invariance, and physicists struggled to identify which theory required correction. Further, other puzzling phenomena, such as black-body radiation (observed by Gustav Kirchhoff in the 1850s) and the photo-electric effect (observed by Heinrich Hertz in the 1880s), had long since been observed but could not yet be defined or modelled effectively by the current theory.

Following a series of theoretical developments on these subjects, Max Planck offered his hypothesis on the quantum nature of light in 1900, which would prove critical for the development of Quantum Mechanics later in the 1920s. Shortly after, Albert Einstein proposed his theory of Relativity in 1905, which, after some further development, would become widely accepted by the 1920s. Relativity resolved the inconsistency between Maxwell's electromagnetism and Newton's mechanics by introducing Lorentz invariance, and showed that a relativistic treatment of mechanics reduces to Newtonian Mechanics at sufficiently low velocities. Together these theories would largely resolve much of the aforementioned phenomena that had not yet been explained.

Meanwhile, following the discovery of the electron by J. J. Thomson and the introduction of his plum-pudding model in 1900, the description of matter at the atomic level also received significant attention by the scientific community. The idea of an atomic nucleus was arguably first posed in 1904 by Hantaro Nagaota as it appeared in his Saturnian model, which posed the existence of a central positive mass surrounded by light, negative electronic rings. There were several serious problems with the idea however, the most notable being that the current theory suggested the electrons should lose energy through electromagnetic radiation and all atoms should collapse in on themselves in a matter of picoseconds.

Though Nagaota later abandoned the Saturnian model in 1908 for this and other reasons, many of the model's key features later reappeared in the Rutherford-Bohr model of the atom in 1913 following the Rutherford gold-foil experiment. The model was still plagued by a number of problems, but after several experimental discoveries (spin, protons, isotopes, neutrons) and the development of both quantum mechanics and quantum electrodynamics (QED), these problems would be largely resolved by the mid-1930s. The 1920s also marked the beginning of the atomic shell model and the Configuration Interaction (CI) methods used in quantum chemistry. Both would eventually prove instrumental for modeling nuclei decades later.

However, a new problem had emerged by the 30s: the discovery of separate nucleons suggested there must be some new force that kept the nucleus together despite coulomb repulsion. To explain this, Werner Heisenberg proposed in 1932 the idea that the neutron might be a composite particle of a proton and electron, and that by exchanging an electron with another proton, the nucleus is kept together. There were problems with the description, the most notable being that two spin $1/2$ particles like the proton and electron cannot add to a spin $1/2$ neutron, though the idea would prove useful and also lay the foundations for the concept of isospin.

In addition to the former issue, various weak decays, such as β-decay, had been observed but not yet explained. Starting from Heisenberg's idea, Enrico Fermi proposed his theory of the weak interaction in 1933 to explain such phenomena, and resolved the issue of conserving linear and angular momentum through the introduction of the neutrino. This too would ultimately prove insufficient, as it was demonstrated the emission of the neutrino and electron would be insufficient force to hold nuclei together.

Following the works of Heisenberg and Fermi, Hideki Yukawa combined their ideas in 1935 by proposing a short-range interaction mediated by boson exchange, and defined what would subsequently be called the Yukawa potential. The potential included an inverse power of radial separation for coulomb repulsion at longer ranges, but was dominated by an exponential associated with the boson exchange at short-ranges. Unlike the massless photon of Quantum Electrodynamics, Yukawa estimated the boson (called the "meson" due to having mass between the electron and proton) in-

volved in the short-range interaction would need to be roughly 200 times more massive than the electron, and his description would be proven correct around a decade later with the discovery of the pion. Moreover, his potential is commonly seen to represent the first working description of the NN potential, and would prove key to the development of mean-field approaches, meson-exchange theory, and various phenomenological interactions that would form the bedrock upon which all modern Nuclear Structure calculation is founded. Even still, it wouldn't be until the 60s that the true nature of the strong force would be discovered.

Nevertheless, this time saw developments in other directions. While classical field theories had been used to great success already for electromagnetism since the 18th century the work of Dirac QED marked the first Quantum Field Theory (QFT) [3], which continued to develop with the introduction of the Dirac equation in 1927, a relativistically invariant treatment of QED in 1938, and the path-integral formalism of Feynman diagrams in the late 40s. However, the higher-order terms of QED always produced infinite contributions, and a method to resolve this problem (which would be called renormalization), would not appear until 1949 with the works of Feynman and Schwinger.

The main thrust of renormalization in this context is to add counter-terms to the Lagrangian that cancel the infinities, and redefine a finite number of physical quantities to account for the effects. While the procedure was long considered suspect even by some of its progenitors, renormalization would eventually be embraced and prove vital to understanding how different physical scales can be connected; a concept that is critical to modern Nuclear Structure and the foundation of EFT. At the time however, though renormalization resolved the remaining issues of QED, it did not ultimately resolve all the problems faced by using QFT to describe microscopic particle interactions, and it would be another two decades before another major step forward was made. For a more comprehensive review of the developments of QFT and the nuclear paradigm through the first half of the 20th century, see Ref. [4].

1.1.2 Early Nuclear Structure models

Returning to the development of Nuclear Structure, the first collective nuclear model predictions were made in the 30s using the liquid-drop model, where one calculates the binding energies in a way similar to calculating the surface tension of a spherical drop of fluid. The model proved very effective at approximating nuclear binding energies observed by experiment, and, with the addition of several correction terms following various other discoveries up to the 50s, would eventually evolve into the Semi-Empirical Mass Formula (SEMF), which is still considered a useful approximation today.

On the other hand, all attempts at a microscopic nuclear model failed until 1949, when the independent particle model (IPM) was developed [5, 6]. While the presence of "magic" nuclei (i.e. nuclei with greater binding than those with slightly different nucleon counts) had been observed since the 30s and a shell structure considered, all attempts at describing the nuclear potential failed to correctly predict these magic numbers until the development of a spin-orbit term in 1946. The IPM involves treating each nucleon independently in a central mean-field plus a spin-orbit term, while still requiring Pauli exclusion for fermions (much like one solves the electron orbitals of the atomic shell model), such that the nuclear wavefunction is expressed as a Slater determinant of the individual particle wavefunctions.

While the IPM successfully predicted the binding energies of closed-shell nuclei and established the legitimacy of a shell structure to the nucleus, it failed to offer accurate predictions for observables of most other nuclei, and was generally not seen as an accurate description of most microscopic Nuclear Structure. Indeed, despite the relatively straightforward force laws of gravity and electromagnetism, the nuclear force did not appear nearly so well-behaved, and only an effective interaction could be defined.

For this purpose, two types of solutions appeared; the first were phenomenological approaches that attempted to define more general forms of the average nuclear potential using an appropriate mathematical function, much like the inclusion of the spin-orbit term successfully predicted magic nuclei. Though some success was found with deformed potentials and using experimental results

to fit more complex functional forms such as the Wood-Saxon potential, it became apparent that a purely mean-field treatment was insufficient for most nuclei.

The second solution involved the Hartree-Fock-Bogoliubov (HFB) method, where the focus shifts to finding an appropriate effective 2N interaction which describes nuclear properties by iteratively solving the Schrödinger equation to variationally improve an ansatz wavefunction constructed from a Slater determinant of single-particle states. In effect, this involves forming a system of equations where the unknowns are the single-particle wavefunctions, and one solves the system such that the energy is minimized. A successful HFB 2N potential can be used to solve the Schrödinger equation in a basis expansion, and this led to numerous successful descriptions of a range of low-excitation energy nuclear properties, especially for nuclei above about atomic number 60. This process and others like it are often called self-consistent mean-field approaches, and are still used in Density Functional Theory and effective models of heavy nuclei.

1.1.3 The rise of Nuclear Structure calculation

While the development of the aforementioned methods were significant, the growing amount of experimental information placed demands on the theory that went beyond the capabilities of mean-field approaches like the HFB method. Increasingly, the need to include residual inter-nucleon interactions beyond the mean-field arose. This led to the development of effective inter-nucleon interactions among "valence nucleons", nucleons outside an inert core of a magic number nucleus. However, the computational challenges posed by considering many valence nucleons made progress exceedingly cumbersome. This changed by the 60s when computers first began to become available, and larger basis spaces became a more realistic option. This was when the first shell model codes appeared, and marks both the development of Interacting Shell Model (ISM) calculation and the beginning of Nuclear Structure calculation as it is perceived today.

The ISM involves breaking nuclear shells into a core, valence, and external space. The core is treated with a mean-field ansatz, where core nucleons are considered inert and thus do not appear in the Slater determinant wavefunction. Instead the wavefunction contains only the remaining valence

shell nucleons, and the Slater determinant basis is truncated beyond a certain valence shell. The impact of the unoccupied external space can then be estimated through renormalization (though this would not be fully realized until later).

The ISM has seen great success, and remains a major paradigm in Nuclear Structure. Unsurprisingly however, the assumption of an inert core turns out to neglect important degrees of freedom (DoFs) in many nuclear states, such as states involving collective motion, and can become a poor description of the microscopic system. Moreover, such a treatment usually makes quantifying the result's uncertainty very difficult, which is vital to the calculation's practical use.

To address these limitations (in both Nuclear Structure and quantum chemistry, which had been facing similar challenges), various new model treatments were developed in the decades leading up to the present where the assumption of an inert core is relaxed or done away with entirely. The former, such as cluster approaches like the Interacting Boson Model (IBM) [7], find a happy medium that allow them to solve certain heavier systems the ISM could not, but face similar limitations for their own set of nuclei. These sorts of approaches are therefore often called "effective" models. The latter became known as *ab initio* (or "from the beginning") models, and will become the focus of our discussion later.

1.1.4 The path to a realistic nuclear interaction

Returning now to the topic of the 2N interaction, by the 70s quarks were discovered and QCD was defined as the governing theory of the strong force. Indeed, It would eventually be understood that the nuclear force is in truth only a consequence of quark/anti-quark/gluon (qq) interactions.

However, while qq interactions are well-defined at high energies, the problem becomes much more complex at low energies due to two fundamental properties of QCD: color confinement and asymptotic freedom. That is, the strong force interacts weakly at high energies (allowing perturbative solutions), but at low energies becomes strong and prevents colored particles (quarks) from being isolated. Consequently, attempts at modeling low-energy quark systems, let alone nuclei, at the level of QCD proves very challenging.

Nevertheless, the advances in QCD and QFT led to substantial progress in the following few decades on relativistic treatments that would come to be collectively called meson-exchange theories. Despite significant challenges and some drastic approximations when applied to low-energy properties of nuclei, these theories led to the development of several highly-accurate meson-exchange potentials still used today. These potentials involved the inclusion of phenomenological terms that can be fit to match contemporary 2N data with very high accuracy. Some examples of the most successful of these include CD-Bonn [8], Argonne V18 [9], and several others, and they've allowed unprecedented success in numerous Nuclear Structure calculations.

Thus, most Nuclear Structure relied on phenomenological potentials through the 80s and 90s, while the community's understanding of renormalization and scale transformation continued to develop and be formally defined. The development of EFT and subsequently χEFT in the late 90s has since offered the necessary formalism for a well-defined, quantitative description of interactions and nuclear phenomena at vastly distinct scales than those of the governing forces.

Consequently, the last two decades have since seen tremendous advancement in the development of a realistic 2N interaction rooted in QCD with well-defined theoretical uncertainties, and efforts towards defining a realistic 3N interaction have also progressed greatly. While presenting some significant mathematical and computational challenges, realistic interactions have certain advantages over their phenomenological counterparts, the most notable being that their roots in QCD allow the well-defined propagation of theoretical uncertainties. So long as the model uncertainty is also well-defined, Nuclear Structure results with such an interaction can potentially be used to validate (or invalidate) theory and predict emergent phenomena in ways phenomenological potentials cannot. Nevertheless, these realistic potentials pose several difficult challenges, and their implementation remains a dominant focus of current research.

1.2 Modern Nuclear Structure

Ostensibly, one would like to describe all quark and Nuclear Structure directly from the theory of the strong force, that being QCD. Unfortunately, the complexity of QCD and the very wide

interval of scales relevant to nuclei make a single theoretical approach that is effective for all sizes of nuclei (let alone the inclusion of quark systems) rather unlikely in the foreseeable future.

Instead, a more realistic strategy (and the contemporary one) is to use a sequence of different model frameworks at different scales, where the frameworks are connected to each other in a well-defined theoretical treatment of scales. Specifically, the frameworks closer to the scales of QCD are used to define the effective inputs required to retain predictive power at a much larger scale. The formal treatment relating these scales is manifestly EFT.

Effective Field Theory (or sometimes just Effective Theory outside the context of QFT) allows the study and description of how the DoFs at one physical scale evolve from the (usually different) DoFs at the scale of the system's underlying substructure, and its development can be seen woven through particle physics, statistical mechanics, general relativity, and several other disciplines. In Nuclear Theory, the works of Weinberg [10, 11] and van Kolck et. al. [12] in the 90s pioneered an approach based on the chiral symmetry exhibited by QCD, where one begins from the most general Lagrangian for pions and nucleons before accounting for the spontaneous chiral symmetry breaking. This treatment, called Chiral Effective Field Theory (χEFT), and its perturbative sorting of terms, called Chiral Perturbation Theory (χPT), offers a model-independent approach for low-energy Nuclear Structure possessing both a direct connection to the underlying QCD symmetries and a systematically improvable calculation scheme. Consequently, (χEFT) has become the contemporary modern approach for connecting the distant scales of QCD and nuclei, and represents a rapidly growing field of study in Nuclear Theory.

For instance, beginning from QCD, one may use lattice-based methods to simulate quarks and gluons directly. Using those results, one may determine the low-energy constants (LECs) required to define effective interactions and operators that average over the QCD substructure under χEFT.

Using these effective interactions and operators in *ab initio* methods allows the modeling of light nuclei and the determination of their observables. Performing an additional unitary transformation, such as one defined by the Similarity Renormalization Group (SRG, a subject that is closely related to EFT) can further extend the reach of these methods. Furthermore, with sufficient renormalization

the effective interactions can be used in configuration-mixing and cluster models for medium-sized nuclei, and in turn define the mean-field and effective forces required by density functional theories for the effective modeling of the heaviest nuclei.

Despite how both this goal of a unified, broadly-applicable approach and its solution using a model hierarchy bound together by a common theoretical framework are fairly pervasive ideas throughout current literature, I have not found a phrase to easily refer to the general notion of such a treatment. Thus, for lack of a better term, I shall refer to this concept as a "unified nuclear effective model", or UNEM, to facilitate the idea's discussion. That is, without specifying the specific model treatments or their interdependence, I shall use UNEM to mean a formal, well-defined approach that overcomes the distant scales of nuclei by applying multiple frameworks within a hierarchy of scale where each framework's inputs and outputs (and consequently the uncertainty associated with them) are connected by a quantifiable treatment of the scale transformations between them.

The primary challenge in determining a successful UNEM then is to retain the important physics and avoid arbitrary renormalizations at each redefinition of the DoFs. That is, as the nucleus being considered varies both between 1) the proton and neutron drip lines and 2) light to heavy nuclei along the valley of stability, we need to acquire a better understanding of how the behavior of nuclear matter changes, how the relevant DoFs evolve, and, consequently, how each will best be described. This is particularly true for nuclei with large neutron excesses, which, despite being where most heavy nucleosynthesis occurs, is also where the predictive power of modern Nuclear Structure appears to require the most improvement [13].

Naturally, the first steps for both developing such an understanding and identifying the feasibility of a UNEM requires defining the connection from QCD to light nuclei. Since the latter are generally the domain of *ab initio* approaches, we now focus our attention to their discussion.

1.3 Nuclear Structure *ab initio* Theory

We introduce *ab initio* Nuclear Structure Theory and establish some of the field's current context. We begin with a broad description of *ab initio* approaches and what defines them in Subsection 1.3.1.

We then describe the significance of uncertainty calculation as it pertains to contemporary Nuclear Structure in Subsection 1.3.2.

1.3.1 Introduction to *ab initio* theory

In low-energy Nuclear Physics, recent progress has been made in the microscopic *ab initio* nuclear theory of light nuclei, allowing the effective modeling of nuclear dynamics and the interactions of hadrons in general. Most *ab initio* methods are distinguished by their inclusion of all nucleonic DoFs in the problem being solved. The NCSM is one such approach, and is a focus of this work. Other methods include the Hyperspherical Harmonics (HH) method, Variational Monte Carlo (VMC) method, In-Medium Similarity Renormalization Group (IMSRG), Green's Function Monte Carlo (GFMC), Coupled-Cluster (CC), Lattice QCD (LQCD), as well as several others.

Though each has its own strengths and weaknesses, all *ab initio* methods generally possess three common features (beyond their consideration of nucleon DoFs). The first is that they rely on computational techniques to solve the nuclear Schrödinger equation numerically within a controlled approximation scheme. The second is that they possess well-defined model uncertainty. Last, their common limitation is the prohibitively expensive computational requirements of considering the "full" NMBP as the number of nucleons and the calculation's precision increases.

While their limitations proved particularly restrictive in the 70s and 80s, the continued growth in computational resources has allowed enormous steps in the range of nuclei that may be addressed by these methods. Further, several variations of *ab initio* approaches exist where approximations are introduced that reduce the size of the problem at the risk of limiting the cases it may be applied to, and are therefore generally referred to as "effective" treatments. Some examples include the IMSRG(2) approximation or the IBM.

Within the last decade, many of the questions regarding the accuracy of *ab initio* methods have been resolved, as computational resources have grown and improved methods for determining the sources of model uncertainty have been developed. Consequently, the differences that are still observed between *ab initio* results of light nuclei and experiment are now commonly considered

largely the result of the theoretical treatment of the interactions and operators themselves, rather than the many-body methods being used to calculate their observables. Thus, determining an effective nuclear interaction (as well as other effective operators) has become an even greater point of focus.

Most *ab initio* methods involve choosing at least a 2N potential as input, though the need for a consistent 3N potential has become commonly recognized for realistic calculations of most nuclei, and the accurate description of 3N forces remains one of the primary long-term goals of current research. These potentials are then used in a non-relativistic quantum many-body framework that reflects the symmetries relevant to the choice of potential(s). However, high-quality representations of the nuclear interaction are both difficult to determine and often challenging to implement. Indeed, this is, in some sense, reflected by the fact that there doesn't appear to be a simple analytic expression for either a mean-field nor 2N (nor 3N) interaction that proves valid for all nuclei. Mentioned previously, the development of realistic interactions provide new possibilities for validating theory with improved uncertainty calculations.

1.3.2 Uncertainty calculation in contemporary Nuclear Structure

Before turning to the topic of the NMBP, I wish to provide a brief aside regarding uncertainty calculation, as it is a significant focus in contemporary Nuclear Structure. In most disciplines involving model approaches, the development of uncertainty calculation follows what one might describe as a certain "natural order". Specifically, the uses of uncertainty calculation generally grow over a model's (and its related theory's) lifetime, as uncertainty estimation often only gets introduced and improved upon as it becomes necessary. In the earliest stages when a model approach is new and still developing, uncertainty estimates can serve as a useful way to gauge whether two different calculations "agree", and this applies for both calculations from two implementations of the same approach, or from two very different model treatments considering the same physical system.

Once a method has become better-defined and a level of confidence in its reliability is developed, uncertainty calculation usually becomes even more important for a new reason: to determine when

experimental and theoretical results disagree enough to suggest the possibility of new physics. Finally, even when an approach and the results it predicts become sufficiently well-tested, understood, and universally-accepted that they, in large part, leave the focus of contemporary scientific inquiry, the adoption of that approach or its results in practical endeavors, such as engineering, sometimes demand even more stringent standards of uncertainty estimation.

By comparison, the development of uncertainty calculation in Nuclear Structure calculation was suppressed somewhat by what proved for a long-time a largely insurmountable challenge to connect QCD to the NMBP. That is, while the governing theory was known, a way to apply it at the nuclear scale in a useful way was not, and this greatly restricted what uncertainty estimation (and to some degree Nuclear Structure in general) could be used to say in regards to QCD. Specifically, when using a phenomenological interaction, the discrepancies between a numerical model's results and experiment can be difficult to use to quantitatively validate the nuclear consequences of QCD. Instead, such discrepancies often only serve to test the effectiveness of the phenomenological extrapolation approach by which the interaction was defined, the effective theory it is based upon, and the model approach being implemented itself.

However, the continued development of computer technology and a formalized treatment of both scale transformations and the redefinition of the active DoFs may finally allow the gap between QCD and the NMBP to be bridged, and defines one of the leading interests in the development of χEFT. Similarly, as the accuracy of Nuclear Structure calculations continue to improve and the scientific community's reliance on them continues to rise, there is a growing demand for well-defined and meaningful uncertainty estimation for both a model's practical use and that of its results.

Consequently, the potential uses for high-quality uncertainty calculation have recently greatly expanded. In particular, despite its rapid development, the level of success χEFT can achieve is still unknown, and will depend in part on developing meaningful uncertainty estimation and understanding how that uncertainty propagates through the relevant theoretical frameworks.

However, while the growth in computational resources and effective theory are driving forces for uncertainty estimation, so too have they enabled an explosion in the development of new effective

approaches and tools requiring validation and testing. Thus, Nuclear Structure is presently in a very dynamic state characterized by a mixture of both venerable and developing approaches and techniques with varying levels of uncertainty calculation. While well-established methods mobilize for improved uncertainty calculation, others remain sufficiently new that the development of such tools is not yet required for the primary focus of their study (which tends to be on feasibility, efficiency, and accuracy).

Thus, while many of the calculations in this work reflect the development and early testing of tools that have not yet required the inclusion of highly-accurate uncertainty estimation, I wish to stress the significance that the development of uncertainty calculation currently represents in the field. For more insight on the discussion of this topic and its significance, see Refs. [14–16, 13].

1.4 The nuclear many-body problem

We consider the general A-nucleon system of N neutrons and Z protons. We treat all nucleons as having the average mass of the neutron and proton, $m_N = 938.92\,\frac{MeV}{c^2}$ (while one can include nucleon mass isospin splitting, the correction is small and won't be addressed here). We will denote the single-particle spatial coordinate and momentum for nucleon i as r_i and p_i, respectively. With these we define the system parameters

$$M = Am_N\,, \tag{1.1}$$

$$P = \sum_{i=1}^{A} p_i\,, \tag{1.2}$$

$$R = \frac{1}{A}\sum_{i=1}^{A} r_i\,, \tag{1.3}$$

where M is the system's total mass, P is the center of mass (cm) momentum, and R is the cm position.

Under Hamilton's principle the dynamics of the system are fully encoded by the many-body Hamiltonian

$$\mathcal{H}_A = \mathcal{T}_A + \mathcal{V}_A \tag{1.4}$$

where $\mathcal{T}_A = T_{rel} + T_{cm} = \sum_{i=1}^{A} \frac{p_i^2}{2m_N}$ is the total kinetic energy and $\mathcal{V}_A = U_{CM} + \sum_{a=1}^{A} V_{(a)}$ is the full A-body potential. Naturally, the cm kinetic energy is $T_{cm} = \frac{P^2}{2M}$, where we neglect the small effect of nuclear binding energy on the mass. We can then define the relative (i.e. intrinsic) kinetic energy

$$T_{rel} = T - T_{cm} = \sum_{i<j}^{A} \frac{(p_i - p_j)^2}{2Am_N} \,. \tag{1.5}$$

where our summation avoids double-counting by only summing cases where $i < j$.

The breakdown of $\mathcal{H}_A$ from Eq. (1.4) into many-body terms is called the many-body expansion, and it decomposes the Hamiltonian into a separate one-nucleon (1N) two-nucleon (2N), three-nucleon (3N), up to A-nucleon operator as

$$H_A = \sum_{i}^{A} (H_{1N})_i + \sum_{i<j}^{A} (H_{2N})_{ij} + \sum_{i<j<k}^{A} (H_{3N})_{i,j,k} + ... \tag{1.6}$$

Moving forward, we shall henceforth assume there are no external fields and the system is in its rest frame. The former equation then reduces to the intrinsic Hamiltonian

$$H_A = \sum_{i<j}^{A} \left[\frac{1}{A} \frac{(p_i - p_j)^2}{2m_N} + (V_{2N})_{ij} \right] + \sum_{i<j<k}^{A} (V_{3N})_{i,j,k} + ... \tag{1.7}$$

where V_{NN} is the two-body interaction, V_{3N} is three-body, and so on. Just as was discussed in the introduction, we will only consider up to two-body operators for the purposes of developing the tools discussed in this work.

We ultimately wish to solve the many-body Schrödinger Equation

$$H_A|\Psi\rangle = E|\Psi\rangle \,, \tag{1.8}$$

for eigenenergies E of nuclear $|\Psi\rangle$. How one proceeds from here depends on what many-body approach is applied; see Ref. [13] for a review of various methods. In this work, the NCSM is the primary focus.

References

[1] National Research Council. *Connecting Quarks with the Cosmos: Eleven Science Questions for the New Century*. The National Academies Press, Washington, DC, 2003. ISBN 978-0-309-07406-3. doi: 10.17226/10079. URL https://www.nap.edu/catalog/10079/connecting-quarks-with-the-cosmos-eleven-science-questions-for-the.

[2] Sonia Bacca. Structure models: from shell model to ab initio methods. *Eur. Phys. J. Plus*, 131 (4):107, 2016. doi: 10.1140/epjp/i2016-16107-6.

[3] Paul Adrien Maurice Dirac and Niels Henrik David Bohr. The quantum theory of the emission and absorption of radiation. *Proceedings of the Royal Society of London. Series A, Containing Papers of a Mathematical and Physical Character*, 114(767):243–265, 1927. doi: 10.1098/rspa.1927.0039. URL https://royalsocietypublishing.org/doi/abs/10.1098/rspa.1927.0039.

[4] Cameron Reed. The age of innocence: Nuclear physics between the first and second world wars. *American Journal of Physics*, 87(1):78–79, 2019. doi: 10.1119/1.5075721. URL https://doi.org/10.1119/1.5075721.

[5] Maria Goeppert Mayer. On closed shells in nuclei. ii. *Phys. Rev.*, 75:1969–1970, Jun 1949. doi: 10.1103/PhysRev.75.1969. URL https://link.aps.org/doi/10.1103/PhysRev.75.1969.

[6] Otto Haxel, J. Hans D. Jensen, and Hans E. Suess. On the "magic numbers" in nuclear structure. *Phys. Rev.*, 75:1766–1766, Jun 1949. doi: 10.1103/PhysRev.75.1766.2. URL https://link.aps.org/doi/10.1103/PhysRev.75.1766.2.

[7] F. Iachello and A. Arima. *The Interacting Boson Model*. Cambridge Monographs on Mathematical Physics. Cambridge University Press, 1987. doi: 10.1017/CBO9780511895517.

[8] R. Machleidt. The High precision, charge dependent Bonn nucleon-nucleon potential (CD-Bonn). *Phys. Rev.*, C63:024001, 2001. doi: 10.1103/PhysRevC.63.024001.

[9] Robert B. Wiringa, V. G. J. Stoks, and R. Schiavilla. An Accurate nucleon-nucleon potential with charge independence breaking. *Phys. Rev.*, C51:38–51, 1995. doi: 10.1103/PhysRevC.51.38.

[10] Steven Weinberg. Effective chiral lagrangians for nucleon-pion interactions and nuclear forces. *Nuclear Physics B*, 363(1):3 – 18, 1991. ISSN 0550-3213. doi: https://doi.org/10.1016/0550-3213(91)90231-L. URL http://www.sciencedirect.com/science/article/pii/055032139190231L.

[11] Steven Weinberg. Nuclear forces from chiral Lagrangians. *Phys. Lett.*, B251:288–292, 1990. doi: 10.1016/0370-2693(90)90938-3.

[12] U. van Kolck. Few-nucleon forces from chiral lagrangians. *Phys. Rev. C*, 49:2932–2941, Jun 1994. doi: 10.1103/PhysRevC.49.2932. URL https://link.aps.org/doi/10.1103/PhysRevC.49.2932.

[13] Petr Navrátil, Sofia Quaglioni, Guillaume Hupin, Carolina Romero-Redondo, and Angelo Calci. Unified ab initio approaches to nuclear structure and reactions. *Phys. Scripta*, 91(5):053002, 2016. doi: 10.1088/0031-8949/91/5/053002.

[14] J. A. Melendez, S. Wesolowski, and R. J. Furnstahl. Bayesian truncation errors in chiral effective field theory: nucleon-nucleon observables. *Phys. Rev.*, C96(2):024003, 2017. doi: 10.1103/PhysRevC.96.024003.

[15] E. Epelbaum et al. Few- and many-nucleon systems with semilocal coordinate-space regularized chiral two- and three-body forces. *Phys. Rev.*, C99(2):024313, 2019. doi: 10.1103/PhysRevC.99.024313.

[16] Oscar Javier Hernandez, Sonia Bacca, and Kyle Andrew Wendt. Recent developments in nuclear structure theory: an outlook on the muonic atom program. *PoS*, BORMIO2017:041, 2017. doi: 10.22323/1.302.0041.

CHAPTER 2. NO-CORE SHELL MODEL CALCULATION

The NCSM [1] method is a CI approach that treats all present nucleons as active (i.e., it considers the state of each nucleon as a unique DoF) and is conventionally expressed in the three-dimensional harmonic oscillator (HO) basis. The phrase "No-Core" serves to distinguish it from the interacting shell model, which generally assumes an underlying Hartree-Fock approach and therefore only considers the DoFs of nucleons on the outermost shells and approximates the inner shells with an inert mean-field core.

The NCSM method can be summarized as constructing the nuclear Hamiltonian using effective 2N (and possibly 3N) interactions, expressing the Hamiltonian as an infinite matrix expanded in a complete basis, approximating that Hamiltonian matrix by truncating the infinite basis, and diagonalizing the now finite Hamiltonian to determine its eigenpairs. Once solved, the eigenstates may then be used to calculate other observables.

The NCSM approach was originally performed in the context of applying Okubo-Lee-Suzuki (OLS) renormalization when truncating the infinite Hamiltonian matrix, but as new effective potentials and renormalization schemes became available and computational resources increased, OLS renormalization became less of a necessity for the approach. Consequently, the phrase began to more generally characterize any CI approach that adopts the "No-Core" model perspective, regardless of whether any renormalization is performed or what basis is considered. Nevertheless, as time passed and other variations on the method were developed, two other phrases began to appear in the literature to disambiguate themselves from the original NCSM approach: the No-Core Full Configuration (NCFC) approach, and the No-Core Configuration Interaction (NCCI) approach.

The NCFC approach was originally introduced in 2008 to refer to NCSM calculation without OLS renormalization, and instead augmented by extrapolation approaches to the continuum limit

and the use of χEFT-motivated 2N interactions [2]. The phrase NCCI approach was then later used in 2012 to refer to the computational methods common to both methods [3].

Nevertheless, the precise meaning of these terms have become somewhat nuanced and dependent on context. Thus, to avoid confusion I will explicitly define my intended meaning of each phrase as they appear in this work. In doing so I make no claims as to any strict definitions of these terms, but instead maintain them solely for the sake of clarity.

I shall henceforth use "NCCI" to generally refer to an approach that solves the full NMBP (where all nucleons are treated as active) using a matrix-eigensolution technique, and the high-performance computational methods such a technique requires. I use "NCFC" to refer to NCCI study that is augmented by extrapolation or other approaches that do not strictly reduce the DoFs in the NCCI problem. Finally, I use "NCSM" to refer to NCCI calculations performed using the HO basis, regardless of whether renormalization is used. Thus, under these definitions, NCSM calculations can be considered a subset of NCCI calculations, which in turn can be considered a component of the NCFC approach.

For the present discussion, we shall begin by establishing the theoretical framework common to all NCCI calculation, before narrowing to the case of NCSM calculations specifically. NCCI calculations involve expressing the nuclear hamiltonian as a matrix of inner products in a complete basis, i.e.

$$H_A = \begin{pmatrix} \langle\varphi_1|H_A|\varphi_1\rangle & \langle\varphi_1|H_A|\varphi_2\rangle & \langle\varphi_1|H_A|\varphi_3\rangle & \cdots \\ \langle\varphi_2|H_A|\varphi_1\rangle & \langle\varphi_2|H_A|\varphi_2\rangle & \langle\varphi_2|H_A|\varphi_3\rangle & \cdots \\ \langle\varphi_3|H_A|\varphi_1\rangle & \langle\varphi_3|H_A|\varphi_2\rangle & \langle\varphi_3|H_A|\varphi_3\rangle & \cdots \\ \vdots & \vdots & \vdots & \ddots \end{pmatrix} \tag{2.1}$$

where φ_n denotes the nth basis state used for expanding the system's eigenstates. The eigenfunctions then become weighted sums of the basis functions which can be determined by solving the matrix eigenvalue problem. The eigenfunctions thus obtained may then be used to calculate other observables of the system from operator matrix elements calculated in the same basis.

So long as the basis is complete, the expansion is exact and no observable will have any basis dependence. However, since a complete basis will be infinite-dimensional, the Hamiltonian must be truncated to some finite dimension d for practical calculation. This can most easily be seen by taking the inner product of the Hamiltonian with one of its eigenstates $|\Psi\rangle$ and considering the equality

$$\langle\Psi|H_A|\Psi\rangle = \left(\sum_i^{\infty}\langle\Psi|\varphi_i\rangle\langle\varphi_i|\right) H_A \left(\sum_j^{\infty}|\varphi_j\rangle\langle\varphi_j|\Psi\rangle\right) , \tag{2.2}$$

$$\approx \left(\sum_i^{d}\langle\Psi|\varphi_i\rangle\langle\varphi_i|\right) H_A \left(\sum_j^{d}|\varphi_j\rangle\langle\varphi_j|\Psi\rangle\right) , \tag{2.3}$$

Eq. (2.2) is exact as it involves the insertion of identities, while Eq. (2.3) is an inner product on the Hamiltonian with an approximate wavefunction.

The primary benefit of expanding the Hamiltonian in this way is that it may favor a highly-convergent solution. That is, so long as the basis is well-organized, of the appropriate scale, and respects the symmetries of the Hamiltonian, incrementing the cutoff should converge the ground-state energy monotonically (thanks to the variational principle) to the exact solution at the continuum limit, where any basis dependence must vanish.

The step of truncating the basis, sometimes called the Finite Basis Approximation (FBA), regulates the wavefunction, and predicting, accounting, and/or correcting this regulation can be viewed as the root of nearly every computational challenge faced in Nuclear Structure calculation. The quantitative description and handling of basis regulation is sometimes called regulator physics, and is the primary topic of Section 3.1.

In this chapter, we shall discuss NCSM calculation in two representations: first, we shall establish the conventional many-body treatment of the A-nucleon Hamiltonian in a many-body basis constructed from Slater determinants of single-particle HO basis states, and briefly describe some of the computational methods by which the Hamiltonian eigenvalue problem is solved in Section 2.1. Second, we will describe how the formulation can be greatly reduced in the case of the two-nucleon

system and define the 2N NCSM calculations performed in this work using Jacobi coordinates in Section 2.2.

2.1 Many-body NCSM modeling

We describe the NCSM approach employed to solve the NMBP for light nuclei. We begin by establishing some of the many-body formalism and basic concepts that are generally common to NCCI solutions in Subsection 2.1.1. Next, we narrow the discussion to our specific NCSM treatment, and establish the details that distinguish it in Subsection 2.1.2. We then provide a brief description of the computational challenges involved in NCCI calculation and an overview of the numerical methods that are used to overcome them in Subsection 2.1.3. We conclude by offering some perspective on where these calculations fit into the greater scope of Nuclear Structure in Subsection 2.1.4.

2.1.1 Nuclear many-body formalism

Nuclear many-body theory involves model implementations at various scales of the problem, but many of these methods share certain techniques and basic premises. Many-body CI approaches represent a significant portion of the methods employed to solve the NMBP, and appear in one form or another at all scales of the problem. CI methods often share common elements between them, as well as with other approaches to the NMBP.

Thus, we now proceed to define our many-body formalism. Though we shall ultimately focus on the NCSM method and will often use it as an example, much of the discussion remains general and also applies to other methods. We begin by establishing the basic premises and common elements involved in NCCI formulations of the NMBP. Following a brief description of the second-quantized notation that will appear throughout this work, we then describe the Lawson-Lipkin method by which states with cm motion may be shifted higher into the spectrum.

2.1.1.1 Basic premises and common elements of CI approaches

The Pauli exclusion principle requires that identical fermions (such as nucleons) cannot occupy the same quantum state, and that the wavefunction must be antisymmetric under the exchange of any two identical fermions. Thus, many-body basis states may be represented by the list of the single-nucleon states occupied by nucleons. We construct the many-body basis state, $|\Phi_\nu\rangle$, for nucleon configuration ν by taking the direct sum of the separate many-body neutron and proton states, i.e.

$$|\Phi_\nu\rangle = |\Phi_\nu^Z\rangle \oplus |\Phi_\nu^N\rangle \,. \tag{2.4}$$

We independently construct the many-body neutron and proton states, and often use the same single-particle basis for both (though notably this is not strictly required [3]). For example, we express the proton many-body basis states, $|\Phi_\nu^Z\rangle$, as Slater determinants of single-particle states occupied by the system's nucleons, or

$$|\Phi_\nu^Z\rangle = \mathcal{A}\prod_i^Z |\varphi_{\nu_i}^{sp}\rangle \,, \tag{2.5}$$

where $\mathcal{A}$ is an antisymmetrization operator that carries both the sign permutations of the determinant as well as an overall normalization factor and $\varphi_{\nu_i}^{sp}$ is the state occupied by nucleon i. For instance, in coordinate space the many-body proton wavefunction would be defined

$$\Phi_\nu^Z(r_1, r_2, \ldots, r_Z) = \langle r_1, r_2, \ldots, r_Z | \Phi_\nu^Z\rangle = \frac{1}{\sqrt{Z}} \begin{vmatrix} \varphi_{\nu_1}^{sp}(r_1) & \varphi_{\nu_2}^{sp}(r_1) & \cdots & \varphi_{\nu_Z}^{sp}(r_1) \\ \varphi_{\nu_1}^{sp}(r_2) & \varphi_{\nu_2}^{sp}(r_2) & \cdots & \varphi_{\nu_Z}^{sp}(r_2) \\ \vdots & \vdots & \ddots & \vdots \\ \varphi_{\nu_1}^{sp}(r_Z) & \varphi_{\nu_2}^{sp}(r_Z) & \cdots & \varphi_{\nu_Z}^{sp}(r_Z) \end{vmatrix} . \tag{2.6}$$

Notably, switching any two rows (i.e. interchanging two protons) in the Slater determinant preserves the magnitude of the nuclear wavefunction but reverses the overall sign, which is precisely the fermionic behavior we desire. We also see that since the many-body states are dependent on both Z and N, the resulting many-body basis is consequently specific to the nucleus under consideration.

2.1.1.2 Second quantization and normal-ordering

For the purposes of discussing many-body states and operators, it is often convenient to use the language of second quantization, which will appear intermittently in the discussions to follow. Thus, before continuing, we establish some standard definitions:

$$|0\rangle = |0\,0\,0\,\ldots\rangle\,, \tag{2.7}$$

$$a_\alpha^\dagger|0\rangle = |\alpha\rangle\,, \tag{2.8}$$

$$a_\alpha^\dagger|\alpha\rangle = |0\rangle\,, \tag{2.9}$$

$$a_\alpha|\alpha\rangle = |0\rangle\,, \tag{2.10}$$

$$a_\alpha|0\rangle = 0\,, \tag{2.11}$$

$$\left\{a_\alpha^\dagger,\, a_\beta^\dagger\right\} = \{a_\alpha,\, a_\beta\} = 0\,, \tag{2.12}$$

$$\left\{a_\alpha,\, a_\beta^\dagger\right\} = \delta_{\alpha\beta}\,, \tag{2.13}$$

where $|0\rangle$ is the vacuum state, $a_\alpha^\dagger$ and a_α are the single-nucleon creation and annihilation operators of the state $|\alpha\rangle$, respectively, and Eqs. (2.12), (2.13) define their anticommutation relations. For the sake of clarity, we shall denote single-particle states with the index ν_i when discussing a given many-body configuration ν, and use the Greek indices $\alpha, \beta, \gamma, \delta$ in the context of many-body operators.

Using this notation, we can rewrite the many-body state of Eq. (2.5)

$$|\Phi_\nu^Z\rangle = a_{\nu_1}^\dagger a_{\nu_2}^\dagger \ldots a_{\nu_Z}^\dagger|0\rangle = |\nu_1\nu_2\ldots\nu_Z\rangle\,. \tag{2.14}$$

Similarly, one can write the total action O of an anti-symmetrized two-body operator O_{12} as

$$O = \frac{1}{4}\sum_{\alpha\beta\gamma\delta}\langle\alpha\beta|O_{12}|\gamma\delta\rangle a_\alpha^\dagger a_\beta^\dagger a_\delta a_\gamma \tag{2.15}$$

where the factor preceding the summation compensates for overcounting.

Thus far, there remains a great deal of many-body states that are functionally identical beyond a phase factor from the anticommutator defined by Eq. (2.13) that only depend on the ordering of creation and annihilation operators of the same nucleon. To remove this degeneracy, we restrict ourselves to only considering many-body states and operators following a conventional normal-ordering scheme [4]. That is, we require that all creation operators precede annihilation operators, and both appear in ascending order (as defined by the ordering of the single-particle basis). For example, we only consider many-body proton states with the ordering

$$|\nu_1 \nu_2 \dots \nu_Z\rangle = \{a^\dagger_{\nu_1} a^\dagger_{\nu_2} \dots a^\dagger_{\nu_Z}\}|0\rangle \,. \tag{2.16}$$

Moreover, when evaluating an operator's matrix elements, we transpose creation and annihilation operators such that this ordering is maintained, and include the phase factor $(-1)^P$ where P is the number of operator transpositions between the creation and annihilation operators.

2.1.1.3 Shifting out center-of-mass excitations with the Lawson-Lipkin method

The physical phenomena related to nuclear wavefunctions are translationally invariant in nature; the finite methods we use to approximate them however, are often not. One source of this is the limitations on numerical precision inherent to finite methods, which is discussed in Chapter 3. Another source (and the one we will discuss here) is the use of single-particle coordinates defined with respect to a fixed origin, which is not a Galilean invariant treatment.

The primary benefit of a fixed origin is that the antisymmetrization of the Slater determinant becomes trivial when using the one-body coordinate operators r_i, compared to the alternative of trying to use the intrinsic coordinate operators

$$\tilde{r}_i = r_i - R \,, \tag{2.17}$$

which are naturally A-body operators. On the other hand, the drawback of a fixed origin is that the wavefunction solutions will usually have center-of-mass excitations mixed in. Generally, only

the intrinsic motion of the nucleons is of interest to us, which would be obscured by the presence of said cm excitations.

Fortunately, methods for factorizing the spurious cm motion are available and well-understood. We employ the conventional Lawson-Lipkin method [5], which involves shifting states with cm excitations high enough in the spectrum that they can easily be distinguished from the low-lying states of interest. This has been shown (and may be analytically proven) demonstratively effective for the HO single-particle basis under the $N_{\max}$ truncation scheme (described in Subsection 2.1.2), though its potential use in other bases remains largely unstudied.

For example, in the NCSM this involves adding and later subtracting the HO Hamiltonian term $\beta(H_{cm}^{HO}-\frac{3}{2}\hbar\Omega)$ to and from the many-body Hamiltonian, where β is a positive Lagrangian multiplier, $H_{cm}^{HO} = T_{cm} + U_{cm}$, $U_{cm} = \frac{1}{2}M\Omega^2R^2$, and Ω is the HO strength parameter of the single-particle basis. The term serves to shift the states with cm excitations by a scale factor of $\beta\hbar\Omega$ higher in the spectrum. So long as the shift is larger than the highest eigenstate of interest, the states with the lowest cm motion then have the desired factorized form

$$\langle r_i|\Psi_\nu\rangle = \langle R|\Phi_{0s}^{cm}\rangle\langle r_j^{intr}|\Psi_\nu^{intr}\rangle\,, \tag{2.18}$$

where the minimal cm motion Φ_{0s}^{cm} (i.e. the lowest HO wavefunction whose contribution to the internal energy is zero and hence does not scale with β) may be corrected for. That the intrinsic wavefunction factorizes is of critical importance, as certain observables, such as electromagnetic transition rates, would be altered by cm motion.

2.1.2 NCSM many-body basis formalism

So far, our treatment of the many-body system has remained somewhat generic, and could apply to a few choices of bases. The choice of basis represents a common point of variation for solving the NMBP with numerical matrix methods, and various options, each with their own unique advantages and disadvantages, have been considered in an array of studies over the last few decades [6, 3, 7–10].

However, there are some common features any choice of complete basis must possess to be viable for NCCI calculation. First, we generally require a basis respecting parity and total angular momentum, as these are the symmetries of nuclear bound states. Second, beyond being specified by N and Z, any truly general basis must possess at least two additional adjustable DoFs. First, because the complete basis must be infinite, a truncation scheme is required to vary which and how many states are included in the basis (and, consequently, the computational resources required) for a given calculation. Second, the resolution and/or physical scales at which the basis will be effective must be specified. The basis can be defined such that these two features are controlled by a mixture of parameters.

We proceed to describe how our many-body approach addresses these matters, and explicitly define the basis formalism used in the studies contained in this work. First, we describe the M-scheme many-body basis, and begin to explicitly define our treatment. Second, we derive the single-particle basis used to describe the states of individual nucleons. We finish by describing some additional considerations taken when constructing the many-body basis and corresponding matrix representation of the Hamiltonian in practice.

2.1.2.1 The M-scheme many-body basis

We form many-body states of fixed total nuclear angular momentum projection M_J and fixed parity P_P, as the corresponding Hamiltonian will have eigenstates of good total nuclear angular momentum J and parity. Naturally, when A is even (odd), M_J will be integer (half-integer), as the states don't mix due to baryon number conservation. In our case, we use the $M_J = 0$ and $M_J = \frac{1}{2}$ blocks for even and odd A, respectively.

Such a treatment can be easily constructed by using a single-particle basis where the single particle state's parity, p_P, and total momentum magnetic projection, m_j, are good quantum numbers, as then, for a given many-body state,

$$M_J = \sum_i^A (m_j)_i \ , \tag{2.19}$$

$$P_P = \prod_i^A (p_P)_i \ . \tag{2.20}$$

Such a treatment is generally referred to as an M-scheme basis.

While any basis satisfying the former requirements could be used, we choose the HO basis with good total single-nucleon angular momentum j as our single-particle basis, which we define in the following section. We truncate the many-body basis for a given calculation using the cutoff parameter $N_{\max}$, which denotes the maximum total number of HO excitation quanta allowed in any state of the many-body basis above the minimum number of energy quanta, N_0, required by the Pauli exclusion principle for the given nucleus. We calculate the number of energy quanta N_ν in a given many-body state ν by summing the principle quantum numbers N_{ν_i} of all occupied single-particle states, and only include many-body states satisfying

$$N_{\max} \geq \sum_i^A N_{\nu_i} - N_0 = \sum_i^A (2n_{\nu_i} + l_{\nu_i}) - N_0, \tag{2.21}$$

where n_{ν_i} and l_{ν_i} are the radial and angular momentum quantum numbers of the single-particle state ν_i, respectively. Naturally, the former inequality similarly truncates the single-particle basis states that may be occupied, and, in turn, the maximum possible m_j of those states.

Meanwhile, we control the scale of the HO wavefunctions by setting the parameter $\hbar\Omega$, where, as mentioned before, Ω is the HO strength parameter defining the single-particle basis's length scale. The same basis scale applies to all basis states in a given calculation. With our many-body basis defined thus, we move to the task of defining our single-particle basis.

2.1.2.2 The single-particle HO basis

We adopt the common choice of the HO basis for its well-studied finite basis effects, analytical properties, and several other convenient features. We denote the single-particle HO state as $|\phi_\alpha^{sp}\rangle$ with quantum numbers $\alpha \equiv \{n,\, l,\, s\,, j,\, m_j\}$, where n, l, s, j, and m_j, correspond to the radial, angular momentum, spin, total angular momentum, and total angular momentum projection, re-

spectively. Since we treat neutrons and protons separately, we do not include the isospin quantum numbers in our single-particle basis. When constructing the basis, we order single-particle HO states lexicographically by ascending N, n, l, j and m_j, sorted in that order.

To define the full single-particle HO wavefunctions, we first consider just the spatial part of the states, and solve the time-independent Hamiltonian eigenvalue equation for a single particle in a HO potential

$$\left(\frac{\hat{p}^2}{2m_N} + \frac{1}{2}m_N\Omega^2\hat{r}^2\right)|\phi_\alpha^{sp}\rangle = E_\alpha|\phi_\alpha^{sp}\rangle\,, \tag{2.22}$$

where E_α is the eigenenergy associated with the HO basis state $|\phi_\alpha^{sp}\rangle$, and $\hat{r}$ and $\hat{p}$ are the nucleon's position and momentum operators, respectively. The coordinate space solution to this equation is well-known and takes the form

$$\phi^{sp}_{nlm_l}(r,\theta,\varphi) = \langle r\,\theta\,\varphi|n\,l\,m_l\rangle = N_{nl}\frac{R_{nl}(r)}{r}Y_{lm_l}(\theta,\varphi), \tag{2.23}$$

where N_{nl} is a normalization constant, R_{nl} is the radial function, and Y_{lm_l} is a spherical harmonic. We define the radial function[1]

$$R_{nl}(r) = \left(\frac{r}{b}\right)^{l+1} exp\left(-\frac{r^2}{2b^2}\right) L_n^{l+\frac{1}{2}}\left(\frac{r^2}{b^2}\right)\,, \tag{2.24}$$

where $b \equiv \sqrt{\frac{\hbar}{m_N\Omega}}$ defines the basis's length scale, and $L_n^{l+\frac{1}{2}}$ is a generalized Laguerre function defined by the Rodrigues formula,

$$L_n^{(k)}(x) = x^{-k}\frac{\left(\frac{d}{dx}-1\right)^n}{n!}x^{n+k}\,. \tag{2.25}$$

Defining the dimensionless coordinate $\rho \equiv \left(\frac{r}{b}\right)^2$, we may conveniently re-express the spatial part of the wavefunction

$$\phi^{sp}_{nlm_l}(\rho,\theta,\varphi) = \frac{N_{nl}}{b}\rho^{\frac{l}{2}}e^{-\frac{\rho}{2}}L_n^{l+\frac{1}{2}}(\rho)\,Y_{lm_l}(\theta,\varphi)\,. \tag{2.26}$$

[1]Note we have defined our "radial function" as a unitless quantity. Despite being less intuitive, this proves very convenient for demonstrating both useful properties of the HO basis and in the derivation of operator matrix elements.

where one can determine $N_{nl} = \sqrt{\frac{2}{b}\frac{n!}{(n+l+\frac{1}{2})!}}$ satisfies the normalization condition.

Taking a brief detour, one notices a symmetry exists in the HO Hamiltonian between the momentum and position operators, specifically in that they are both quadratic. If one were to perform a Fourier transform on the spatial wavefunction defined in Eq. (2.26) or repeat the derivation from Eq. (2.22) but in momentum space, one would find the HO basis possesses a convenient feature: the solutions to the wave equation in momentum space possess an identical form as those in coordinate space, save for the argument ρ being re-scaled. That is, if we instead define $\rho \equiv \left(\frac{p}{b}\right)^2$, $b \equiv \sqrt{\frac{m_N \Omega}{\hbar}}$, and include an overall phase factor of i^{2n+l}, Eq. (2.26) becomes the HO solution in momentum space. This is a key feature of the HO basis, and one we will later use advantageously.

Returning to our goal of defining the single-particle basis, we must next include the spin part of the nucleon's wavefunction. For a single nucleon, this will always take the form of a Pauli spinor χ_{sm_s} with spin $s = 1/2$ and spin projection $m_s = \pm 1/2$.

Finally, we express our single-particle basis with good j using a change of basis, and define our complete basis state wavefunctions

$$\phi^{sp}_{\alpha}(\rho,\theta,\varphi) \quad = \quad \sum_{m_l,m_s} (l\, m_l\, s\, m_s | j\, m_j)\, \phi_{nlm}(\rho,\theta,\varphi)\chi_{sm_s} \tag{2.27}$$

where m_l is the angular momentum projection, and$(l\, m_l\, s\, m_s | j\, m_j)$ denotes a Clebsch-Gordan (CG) coefficient following the Condon-Shortley convention.

2.1.2.3 Many-body basis and operator construction

We define our specific implementation of the described many-body basis when evaluating the many-body Hamiltonian matrix. When constructing the basis for practical calculation, we designate each single-particle state by a unique integer index, and represent many-body states as ordered arrays of these indices. We use the term "orbital" to refer to the subset of single-particle states with the same n, l, and j (but different m_j). We in turn use the term "many-body orbital state" (or

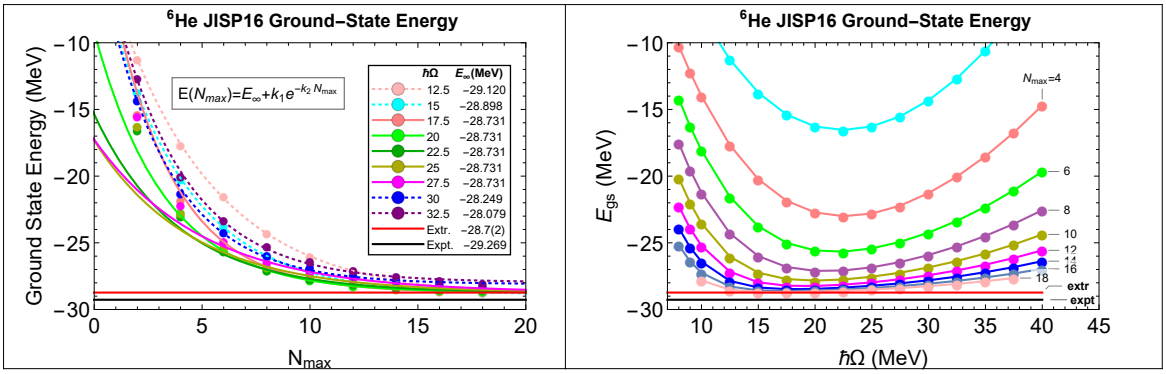

Figure 2.1 Left panel presents the ^{6}He ground-state energy as a function $N_{\max}$ for various basis scales distinguished by color. Points denote NCCI results, while lines denote local fits of Eq. (3.8) to the NCCI results of the corresponding color. Dotted lines designate least-square fits performed independently from other basis scales, while solid lines denote the fits fixed by the global extrapolation described in Section 3.2. The right panel provides the same NCCI results but now varying with HO basis scale, where connected points share the same $N_{\max}$. The flat black and red lines denote the experimental result and the global extrapolation A5 result, respectively.

"MBO state")[2] to refer to the subset of many-body states where the orbital of each single-particle state remains constant.

Combining the many-body states into MBO states allows coarse-grain checks of the common single-particle quantum numbers during matrix construction. Such checks allow us to determine if the entire intersection, or "tile", of a row MBO state and column MBO state will be filled with zeroes. For a 2N (3N) potential, this occurs whenever the MBO states differ by more than two (three) orbitals. For the kinetic energy operator (and any other operator), this occurs whenever the MBO states violate the operator's selection rules.

2.1.3 NCCI many-body calculation

With our theoretical framework defined, we are at last in a position to describe our NCFC many-body calculation. Before we begin however, it is useful to consider some actual results, as it helps establish the context and motivations of the upcoming discussion.

One of the most common nuclear observables pursued by *ab initio* methods (and Nuclear Structure in general) is the nuclear binding energy, as modeling the eigenstates of the nuclear Hamiltonian accurately is a necessary step for calculating any other nuclear observable. To provide an example, we consider the results depicted in Fig. (2.1), which shows the ground-state energy of ^{6}He using the JISP16 potential [11], a soft (i.e. strongly-diagonal), 2N potential that provides high-accuracy 2N scattering results and converges faster compared to many alternative potentials when modeling light nuclei. On the left we see how the ground state energy converges as $N_{\max}$ increases for various choices of basis scale, which are distinguished by color. The points denote the results of NCCI calculations, while lines denote an NCFC extrapolation using the results of the corresponding color. On the left, the same NCCI results are plotted but now with varying basis scale $\hbar\Omega$, where connected points all share the same $N_{\max}$ basis cutoff. In both plots, the red and black horizontal lines represent an extrapolation using all the NCCI results fit with solid lines and the experimental result, respectively.

While there is a great deal of physics to be discussed in these figures, there are two primary observations to make at present. First, focusing on just the NCCI results, it is clear that even for just the $A = 6$ system using a soft potential, several steps in the basis cutoff $N_{\max}$ are required before the NCCI results become a reasonable approximation of the nucleus's ground-state energy (it generally requires even higher $N_{\max}$ before the wavefunction has converged). Indeed, we see the NCCI results depend strongly on $N_{\max}$ for low basis cutoffs, and do not come within 10% of their converged value until around $N_{\max} = 10$, even at the optimal basis scale. Beyond a few exceptions (such as magic nuclei), the convergence rates of larger nuclei generally tend to be either roughly similar or slower to converge given the same nuclear interaction, such as can be seen from the ^{12}C

[2] It should be noted that the term "MBO state" is purely an invention of this work and does not appear in the literature.

and ^{16}O results using JISP in Ref. [12]. While the $N_{\max}$ cutoff required varies both on the potential being used as input and the operator observable in question (the reasons of which will be explored in Section 3.1), one fact is clear: multiple steps in the basis cutoff are generally required for meaningful NCCI results.

Second, we see the trends of the ground-state energy remain very consistent, converging monotonically from above. This can be seen as a consequence of the variational principle, which guarantees that the approximation of the nuclear Hamiltonian's ground state can only be improved by the addition of more basis states[3]. The combination of this consequence of the variational principle and the trend's simple functional form make extrapolations to the continuum very effective for NCCI ground-state energy results, and represents one of the primary methods in which NCFC methods work to improve upon NCCI calculations. This shall be further discussed in Section 3.2.

Having established some of the context of NCCI calculation, we now move to describe its methods in greater detail. Specifically, we discuss aspects of the computational challenges involved in performing NCCI calculation, and describe some of the current methods by which they are overcome. In most cases we will consider these matters through the lens of NCSM calculation performed using the NCCI code "Many Fermion Dynamics for nucleons" (MFDn), though much of the discussion extends to all NCCI calculation in general.

MFDn is a hybrid MPI-OpenMP Fortran code optimized for solving the NMBP, and possesses a long history of high-precision *ab initio* results for light nuclei that spans well over two decades. The research code is constantly maintained for efficient operation on modern leadership-class supercomputers, and significant developments for extending its capabilities are currently underway (aspects of which will be further commented on in Section 2.1.1). While discussing the technical details of MFDn's current implementation are outside our intended purposes here and won't be addressed directly, many aspects of its treatment (and those of High-Performance Computing in general) will be used in our description of how NCCI calculations are performed.

[3]This statement is not to say that NCCI ground-state energy results cannot converge to values below experiment; only that if they do, it is a consequence of the effective potential being used and not the approximation of the wavefunction.

The field of HPC is expansive and a subject we cannot hope to address here in full. Indeed, even just a complete description of the challenges faced by MFDn's HPC implementation and its solutions proves a formidable task that has instigated numerous works [13–15]. However, in order to both define the high-performance NCSM calculations being performed in this work and explain the motivations of the NCFC methods that will be described in Chapter 3, some amount of context regarding NCCI calculation is required. Thus, in this subsection we shall approach these topics not with the intent of completely defining the complex challenges and solutions they involve, but rather with the goal of establishing a broad perspective on what NCCI calculations generally entail.

We begin by explaining the key features of the nuclear Hamiltonian that make NCCI calculation so challenging and establish a sense of the method's limitations. We proceed to review what implementing these calculations on HPC platforms generally involves, some of the common problems that arise there, and some of the general strategies by which they are overcome. Next, we define some of the particular details that distinguish MFDn's implementation and the calculations performed in this work. Finally, we conclude this section by reviewing some of the techniques used to improve and extrapolate these results in NCFC methods.

2.1.3.1 Computational Challenges of the NCCI Hamiltonian

So far we have already seen the significance of the basis cutoff on NCCI results and the subsequent need for larger bases. However, solving for the eigenstates of the Hamiltonian matrices formed by the NCCI treatment described in Subsection 2.1.3 often proves a formidable task for larger $N_{\max}$, and constitutes the primary limitation of what systems NCCI methods can accurately model. This is primarily a consequence of the extremely rapid dimensional scaling of the nuclear Hamiltonian matrix as $N_{\max}$ and A increase. Indeed, despite the enormous strides forward that have been made since NCCI calculation first became viable, the majority of nuclei consisting of more than 20 nucleons or so remains largely unreachable for accurate NCCI modeling on present-day supercomputers.

To demonstrate this fact, we consider Fig. (2.2) as presented in Ref. [17], which illustrates both the rapid increase in the many-body Hamiltonian matrix's dimension as $N_{\max}$ increases for several

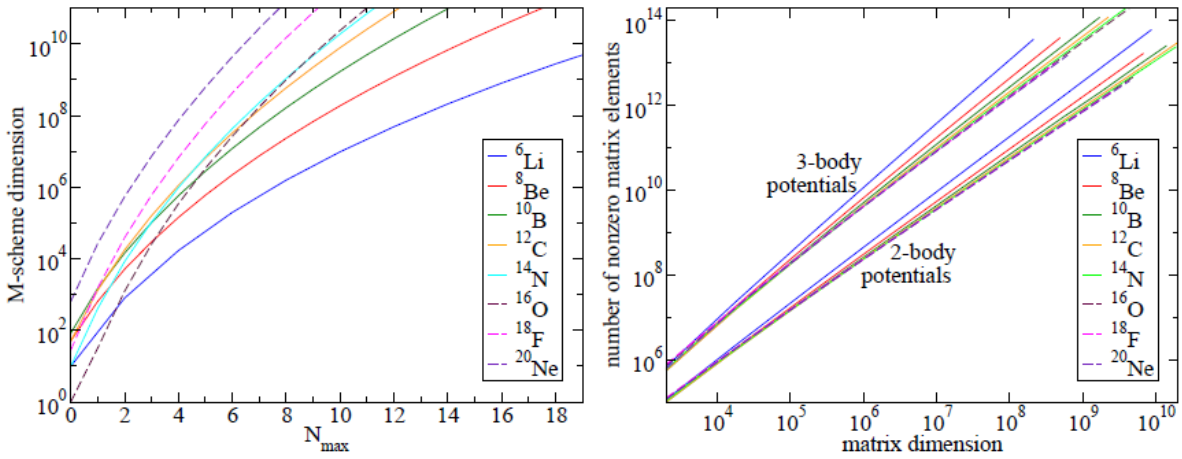

Figure 2.2 Dimensionality (left) and number of nonzero matrix elements in the lower triangular portion of the symmetric matrix (right) for light nuclei with the same number of protons and neutrons (i.e., Z = N), with nuclear angular momentum projection $M_J = 0$ and fixed parity P_P. Figure and caption taken from Ref. [16].

light nuclei on the left, and, in turn, the rapid increase in the number of nonzero elements (nnz) as the dimension increases on the right. The impact of including 3N forces is shown by the differences of dashed and solid lines of the same color in the right panel. While more powerful supercomputers are and continue to become available and the efficiency of NCCI codes continues to be developed, the rate of their improvement still remains too small for the computational limitations exemplified by Fig. (2.2) to be completely resolved in the foreseeable future under current NCCI strategies.

Beyond the rapid dimensional scaling that leads to unfeasibly large matrices, NCCI Hamiltonians possess several other distinct features. First, the matrix is Hermitian, which means the total number of matrix elements being considered can be reduced by (nearly) a factor of two by using only the upper or lower triangle of the matrix. Second, the matrix is sparse, though the density of the nnzs becomes irregular under the standard lexicographical ordering of MBO states. These features in conjunction with the matrix's size makes these calculations a prime candidate for sparse matrix multiplication methods.

2.1.3.2 Performing NCCI calculation on HPC Platforms

Despite these rather daunting challenges, the progress of NCCI calculation over the past few decades has been extremely rapid in the context of the history of Nuclear Structure. This has primarily been the result of the rapid growth of computational resources, the continued improvement of HPC methods, and certain revolutionary developments in how Nuclear Theory is approached. Here we will focus on defining some of the modern methods employed to perform NCCI calculation. Though we will largely focus on the methods implemented in MFDn as that is the CI code used for the NCSM calculations performed in this work, many CI codes (Antoine [18], BIGSTICK [19], KSHELL [20], NuShellX [21], to name a few) face problems and employ methods that are similar or in some cases identical to those described here.

One of the primary challenges NCCI calculation faces is the construction and storage of the Hamiltonian for performing matrix operations, since, as seen in Figure (2.2), the matrix being solved is usually far too large to construct in a reasonable time frame on a typical university computer system. To give an explicit example, we consider the ^{18}F nucleus, which is of significant importance in the radiopharmaceutical industry. The memory required by MFDn to store the full ^{18}F Hamiltonian matrix using a 2N and 3N interaction at $N_{\max} = 6$ is roughly of the order of 10^{13} nnzs, which, stored in single precision (i.e. 8 digits), requires on the order of 100 Terabytes of physical memory. This of course does not include the memory required for solving and storing the eigenvectors, nor does it yet reflect the enormous number of floating point operations (flops) the calculation consequently requires.

While other reasons exist, the matrix's immense memory requirement and the calculation's colossal number of flops are sufficient to demonstrate that most modern NCCI calculations must be performed on supercomputers comprised of a large network of distributed memory multiprocessors, referred to as "nodes", working in parallel. Each node possesses its own memory and CPU(s), which are in turn comprised of multiple parallel processing cores. Information can be transmitted between nodes through the larger network, most often by using the Message Passing Interface (MPI) library standard.

Using these parallel platforms to efficiently perform large-scale calculations is the primary goal of High-Performance Computing, and proves a challenging and complex task that has instigated the development of its own field in Computer Science. While discussing most of the technical details of HPC is outside our goals here, we will now establish some of the pervasive difficulties most relevant to CI codes, as they help explain aspects of the code's design. Specifically, the use of an HPC system introduces several new challenges, such as the risk of poor load-balancing. That is, if the division of the computational workload is much heavier on some nodes than it is on others, this tends to lead to poor performance as the underworked nodes spend significant amounts of time idle, or can even crash the parallel calculation (called a "job") if more data is allocated to a node than it has available memory. Another common class of problems seen in HPC calculations is communication bottlenecks, where, because a node's calculation depends on the data being stored or solved on another node, the node (or at least a subset of its processors) will sit idle while it waits to receive the data.

NCCI approaches overcome these challenges with a number of strategies. For the Hamiltonian, many CI codes resolve the problem of memory by recomputing parts of the matrix locally (or "on the fly") as they become needed in the calculations of a given node (or more generally, a separate memory domain or "MPI rank"). This can make the calculation far less memory intensive, but poses new problems, such as how the reconstruction often becomes time-consuming for iterative eigensolver methods. In MFDn, the full matrix is instead partitioned and arranged on a two-dimensional (2D) grid where only the matrix elements in the lower triangle of the many-body Hamiltonian are distributed to reduce the memory footprint. This is done before the iterative method begins, and consequently requires that the total number of distinct memory domains (i.e. "MPI ranks"), N_R, must satisfy

$$N_R = \frac{i(i+1)}{2}\,, \tag{2.28}$$

for some positive odd integer $i \in \mathbb{N}_{\text{odd}}$. This ensures each of the resulting submatrix's dimensions are roughly equal on each MPI rank, which is important for load-balancing.

The irregular sparsity pattern of the nuclear Hamiltonian poses another problem for good load-balancing, as a naive division of the matrix into simple blocks would usually result in some blocks containing no nnzs while others contain mostly nnzs. In MFDn, this is resolved by distributing the row and column MBO states (described in Subsubsection 2.1.2.3) to each MPI rank in a "round-robin" fashion, as this helps to spread out the dense and sparse parts of the matrix.

Once the matrix is successfully constructed in memory, the diagonalization process may begin. As discussed before, the prodigious size of the matrix makes any complete diagonalization scheme impractical. Moreover, only the lowest-lying eigenstates are generally of any interest. Thus, an algorithm that can identify and accurately determine just this subset of eigenstates is required. While often specialized to the problem being solved, the core of most NCCI algorithms involve projecting onto a Krylov subspace, which is usually done with some form of the Lanczos algorithm (specifically, the Hermitian Lanczos algorithm).

The Lanczos algorithm is a common choice of eigensolver for large sparse matrices for a number of useful features, but most often for its low memory footprint compared to other methods, its capacity to solve only a subset of eigenvectors, and it's potential for parallelization. In particular, the process involves only matrix-vector (and, less importantly,vector-vector) products, which makes it much faster (running in $\mathcal{O}(n^2)$ time) than methods relying on matrix-matrix products (such as the QR method, which runs in $\mathcal{O}(n^3)$ time). A simple version of the Lanczos algorithm is shown to provide a well-defined example, see the simple form of the Algorithm (1).

The Lanczos algorithm is itself a variant of the power iteration algorithm, where one repeatedly multiplies an initial (often random) pivot vector by a matrix until the pivot vector converges to one of that matrix's eigenvectors. The Lanczos algorithm is distinguished by its use of information between iterations to construct a tridiagonal matrix that possesses the same eigenvalues as the effective Hamiltonian, and a collection of "Lanczos vectors" (i.e. a Krylov subspace) that may be used on the tridiagonal matrix to determine the effective Hamiltonian's eigenvectors.

By periodically calculating the eigenvectors that have been solved for between Lanczos iterations, one observes that the eigenvectors for the lowest-lying eigenstates converge the fastest, and are

Algorithm 1 The Lanczos Algorithm

procedure LANCZOS(matrix H,vector v_1) ▷ returns subset of H's eigenpairs
  $\alpha, \beta, v \leftarrow \{\}$ ▷ 3 empty lists for collecting info
  $v_0 \leftarrow 0$ ▷ Skip initial orthogonalization at first
  $i \leftarrow 0$ ▷ Iteration index
  $isConverged \leftarrow$ false ▷ Initialize the loop's exit boolean
  while $isConverged$ **is** false **do**
    $i \leftarrow i + 1$
    $\omega_i \leftarrow Hv_i - \beta_i v_{i-1}$ ▷ Get new vector
    $\alpha_j \leftarrow \omega_i \cdot v_i$ ▷ Get overlap with current Lanczos vector
    $\omega_i \leftarrow \omega_i - \alpha_i v_i$ ▷ Orthogonalize new vector for new Lanczos vector
    $\beta_{i+1} \leftarrow ||\omega_i||$ ▷ Get normalization constant of new Lanczos vector
    $v_{i+1} \leftarrow \frac{\omega_i}{\beta_{i+1}}$ ▷ Normalize new Lanczos vector
    $v \leftarrow v \oplus \{v_i\}$ ▷ Append current Lanczos vector for later
    $\alpha \leftarrow \alpha \oplus \{\alpha_i\}$ ▷ Append current overlap α for later
    $\beta \leftarrow \beta \oplus \{\beta_{i+1}\}$ ▷ Append new normalization constant β for later
    Update($isConverged$) ▷ Check for the exit condition (see text for common options)
  end while
  $T =$TridiagonalMatrix(α, β) ▷ $\alpha \rightarrow$ diagonal, $\beta \rightarrow$ off-diagonals
  $eigenvalues =$Eigenvalues(T)
  $eigenvectors =$ Transpose$(v)Tv$
  return $\{eigenvalues, eigenvectors\}$
end procedure

therefore more likely to appear after each iteration than the higher energy spectral states. This may be viewed as largely the consequence of nuclear spectra being increasingly dense for higher excitations. Thus, so long as the number of Lanczos iterations is far larger than the number of desired eigenstates, the chances that the desired states won't appear vanishes, and the accuracy of the lowest-lying eigensolutions can be gauged by how well-converged the results become.

The usual drawback of the Lanczos algorithm is that it eventually becomes unstable. Specifically, the process diverges when the pivot vector becomes too close to an exact eigenvector of H, as then the following Lanczos vector is dominated by noise, and its corresponding β_i becomes very small. The most obvious case this happens is when the number of iterations exceeds the number of dimensions in the matrix, as then more vectors will be solved for than there are eigenvectors of the system. The more subtle way this can happen is if the initial pivot vector (usually chosen at random) happens to be orthogonal to a large number of the systems eigenvectors.

Fortunately, in the case of extremely large, Hermitian matrices like the NCCI Hamiltonian, the number of iterations is so much smaller than the dimension of the matrix that the instability of the Lanczos algorithm is rarely ever a concern. Similarly, the chances of the initial pivot vector being problematically close to orthogonal to one or more of the lowest-lying eigenvectors is also vanishingly small (though numerical noise combined with an extremely dense spectrum can make it less so).

Still, the iterations have to be stopped before the process becomes unstable. This is generally done by setting an iteration limit, a minimum size of β_i, both, or some other convergence metric, and is reflected in the provided algorithm by the boolean condition $isConverged$ being updated by an unspecified function. In the case of CI codes, one common strategy is to check the convergence of the energy eigenvalues after each iteration, but it has been observed that this often doesn't guarantee the eigenvectors are well-converged. Since the eigenvectors are important for solving other operator observables, MFDn instead checks the convergence of the eigenvectors themselves, though at a lower frequency.

Otherwise, the variations on (or alternatives to) the Lanczos algorithm that appear in NCCI implementations tend to focus on ensuring the results are well-converged and improving the efficiency of the process, particularly for the use on HPC parallel platforms. For instance, in one of its eigensolvers, MFDn implements a Locally Optimal Block Preconditioned Conjugate Gradient (LOBPCG) approach, which can boost performance by allowing multiple Krylov vectors to be calculated during each iteration, and is the primary topic of Ref. [16].

While much more could be said as to the complex challenges involved in NCCI implementations on HPC platforms, the former serves our purposes of establishing some of the key problems that motivate how NCCI calculation is approached, and orients us for our discussion of the NCFC and renormalization methods that work to improve the reach of NCCI calculation.

2.1.4 The role of NCCI many-body calculations

In this section, we have established the context of contemporary NCCI calculation, defined our many-body NCSM formalism, and broadly described many of the challenges and solutions common to the approach. We close our discussion of NCCI calculation by offering some perspective on the role NCCI calculation has and continues to play in the greater scope of Nuclear Structure. We review some of the key issues of NCCI calculation, and describe how they lead us to our upcoming discussion of the NCFC tools that augment NCCI results.

Despite being restricted by the explosive growth of the computational resources they require, NCCI many-body calculations and other *ab initio* calculations like them serve a vital role in both the short and long-term goals of contemporary Nuclear Structure. First, the high-precision results for few-body systems they provide make them the premier tools for examining light nuclei. In the greater scheme however, *ab initio* approaches stand as the gatekeepers sitting between the shift from quarks and gluons in QCD and the effective treatment of nucleons. On one side stands the lattice approaches which can accurately describe the underlying theory used by χEFT to define the realistic interactions all Nuclear Structure models will rely on. On the other side stand the effective models that approximate the "full" many-nucleon problem in ways that make it possible to perform calculations for heavier nuclei, at the cost of general applicability.

Thus, *ab initio* approaches play a critical role in connecting these two disparate scales by providing benchmark calculations for the realistic interactions being developed, the results of effective models for larger nuclei, and the effective methods being employed in both. In essence, if EFT is the bridge spanning the ocean between these two scales, then *ab initio* calculation is the pillar that holds its center aloft.

2.2 NCSM in the relative center-of-mass basis

Having established the necessary context of NCCI calculation and Nuclear Structure in general, we now turn to the topic of the effective methods that allow us to augment NCCI results. In the process of developing these methods, it is useful to have a computationally simple test case for

benchmarking the effective nuclear interactions, methods, and theoretical treatments. Before we consider the 3N cases of these effective methods, we must first do so for the 2N versions. Thus, the simplest system to test these methods is naturally the 2N system.

In the 2N system, only the 2N interaction contributes, and Eq. (1.7) reduces to

$$H_2 = \frac{(p_1 - p_2)^2}{2\mu} + V_{2N}\,, \tag{2.29}$$

where $\mu = \frac{m_N}{2} = \frac{938.92}{2}\,\frac{MeV}{c^2}$ is the reduced mass. Naturally, one could proceed from here to solve the problem exactly, but doing so would provide no insight for NCCI methods in larger nuclei.

While our many-body formalism is necessary for larger systems, it becomes somewhat cumbersome and inefficient in the 2N case. In addition, the problem may be even further reduced by transforming to Jacobi coordinates. Thus, in this section we derive a second NCSM treatment restricted to the 2N system using HO wavefunctions defined in the relative-cm (rcm) 3DHO basis, which will be the formalism used in the discussion of effective methods in Chapter 3.

We proceed to define our rcm formalism of the 2N system. We begin by defining our two-body relative coordinate system in Subsection 2.2.1. In Subsection 2.2.2 we define the 3DHO basis formalism to be employed.

2.2.1 Relative-cm coordinates

We consider the general two-particle system. Denoting their spatial vectors $\vec{r_1}$ and $\vec{r_2}$, we define the relative coordinates

$$\begin{aligned} \vec{R} &= \tfrac{1}{2}(\vec{r_1} + \vec{r_2}) \\ \vec{r} &= \vec{r_1} - \vec{r_2} \end{aligned} \tag{2.30}$$

where $\vec{R}$ is the center of mass (cm) spatial vector, and $\vec{r}$ is the relative distance between nucleons. Similarly, for nucleon momenta $\vec{p_1}$ and $\vec{p_2}$, we define

$$\begin{aligned} \vec{P} &= \vec{p_1} + \vec{p_2} \\ \vec{p} &= \tfrac{1}{2}(\vec{p_1} - \vec{p_2}) \end{aligned} \tag{2.31}$$

where $\vec{P}$ is the cm momentum, and $\vec{p}$ is the relative momentum of the two particles. This is generally considered the "mechanics" convention, and will be used throughout this work.

In our discussion of χEFT, we will need to discuss cases of momentum transfer with external probe. In these cases, we shall distinguish coordinates after interacting with the probe with (for the case of momentum $\vec{p}$) $\vec{p}'$. We also introduce the the additional parameter $\vec{q} = \vec{p}' - \vec{p}$ to denote the momentum transfer with the external probe.

2.2.2 The relative-cm three-dimensional harmonic oscillator basis

We define our rcm basis formalism. Where possible, we refer to the derivation of the single-particle HO basis in Subsubsection 2.1.2.2.

For 2N systems throughout this work, we assume the relative and cm solutions are separable and expand each in the HO basis separately. Thus, we expand the rcm two-body wavefunction in the basis

$$|\phi_i\rangle = |\,(n_r l_r; n_c l_c)\, l\, s\, j\, m_j\, t\, m_t\rangle\,, \tag{2.32}$$

$$= \sum_{m_l, m_s} (l\, m_l\, s\, m_s | j\, m_j)\,|\,(n_r l_r; n_c l_c)\, l\, m_l\rangle |\, s\, m_s\rangle |t\, m_t\rangle\,, \tag{2.33}$$

$$= \sum_{m_l, m_s} (l\, m_l\, s\, m_s | j\, m_j) \left(\sum_{m_{l_r}, m_{l_c}} (l_r\, m_{l_r}\, l_c\, m_{l_c} | l\, m_l)\, |n_r l_r m_{l_r}\rangle |n_c l_c m_{l_c}\rangle \right) |\, s\, m_s\rangle |t\, m_t\rangle\,, \tag{2.34}$$

where n, l, s, j, and t denote the 2N coupled radial, rcm angular momentum (i.e. $\vec{l} = \vec{l}_r + \vec{l}_c$) , spin, total angular momentum (i.e. $\vec{j} = \vec{l} + \vec{s}$), and isospin quantum numbers. We denote projection quantum numbers with m, where the subscript denotes the associated quantity. When required, we distinguish relative and cm quantities with the script r and c, respectively.

We define the relative motion in HO basis states that are solutions to

$$H_{rel} |\phi_i^r\rangle = \left(\frac{\hat{p}^2}{2\mu} + \frac{1}{2}\mu \Omega_r^2 \hat{r}^2 \right) |\phi_i^r\rangle = E_i^r |\phi_i^r\rangle\,, \tag{2.35}$$

while we define the cm motion in states that are solutions to

$$H_{CM}|\phi_i^c\rangle = \left(\frac{\hat{P}^2}{4m_N} + m_N\Omega_c^2\hat{R}^2\right)|\phi_i^c\rangle = E_i^c|\phi_i^c\rangle\,. \tag{2.36}$$

Naturally, the solutions to both of these equations are identical in form to Eq. (2.26), which we reproduce here for convenience using the generic form

$$\phi_{nlm_l}(\rho,\theta,\phi) = \frac{N_{nl}}{b}\,(\rho)^{\frac{l}{2}}\,e^{-\frac{\rho}{2}}L_n^{l+\frac{1}{2}}(\rho)\,Y_{lm_l}(\theta,\phi)\,. \tag{2.37}$$

The relative states require the substitutions $\rho \equiv \left(\frac{r}{b}\right)^2$ and $b \equiv \sqrt{\frac{\hbar}{\mu\Omega_r}}$ for the coordinate-space solution and $\rho \equiv \left(\frac{p}{b}\right)^2$ and $b \equiv \sqrt{\frac{\mu\Omega_r}{\hbar}}$ for the momentum-space solution. Similarly, the cm states require $\rho \equiv \left(\frac{R}{b}\right)^2$ and $b \equiv \sqrt{\frac{\hbar}{2m_N\Omega_c}}$ in coordinate space, and $\rho \equiv \left(\frac{P}{b}\right)^2$ and $b \equiv \sqrt{\frac{2m_N\Omega_c}{\hbar}}$ in momentum space.

We express the coupled spin wavefunction for the 2N system with the Pauli spinor χ_{sm_s} where $s = 0(1)$ and $m_s = 0(0,\pm1)$ for the spin singlet (triplet). The singlet is antisymmetrized with the Slater determinant

$$\chi_{00} = |0\,0\rangle = \frac{1}{\sqrt{2}}\begin{vmatrix} S_1(1) & S_2(1) \\ S_1(2) & S_2(2) \end{vmatrix} \tag{2.38}$$

where $S_k(i)$ is the kth single-nucleon spin state occupied by the single nucleon i. The coupled isospinor χ_{tm_t} is handled in an identical fashion.

In most cases, we will only need to consider the relative motion, and will therefore ignore the cm component unless otherwise specified. Similarly, we will relax our notation by suppressing the cm quantum numbers and relative subscript in such cases, i.e.

$$|\,(n_r l_r; n_c l_c)\,l\,s\,j\,m_j\,t\,m_t\rangle \to |n\,l\,s\,j\,m_j\,t\,m_t\rangle\,, \tag{2.39}$$

where it is understood that only the relative motion is being considered.

2.2.3 Numerical NCSM methods in the relative 2N system

We describe our numerical methods for performing NCSM calculation in the relative 2N system. With the problem reduced to a single relative coordinate and subsequently no need for a many-body basis, the rapid growth in basis dimension faced in many-body NCSM calculation becomes linear. Further, since the basis in which the Hamiltonian (and other operators) is expanded is well-defined in j and several other quantum numbers, a greater set of selection rules may be applied to reduce the basis under consideration. In the case of the Hamiltonian, this means only at most two (coupled) channels (where a channel is a single set of coupled angular momentum, spin, and isospin quantum number) need to be considered for the purposes of diagonalization.

For instance, to solve the deuteron ground state, one needs only consider elements of the $({}^3s_1 - {}^3 d_1)$ coupled channel when constructing the Hamiltonian, where we've used the channel's spectroscopic notation. The resulting basis dimension becomes $N_{\max} + 1$, and NCSM calculations can easily be performed at $N_{\max}$ currently impossible for many-body systems.

Thus, with performance being far less of a concern, much more freedom is allowed in the exploration of the problem and the impact of effective methods. To conduct such analysis, we perform calculations using Mathematica 11 for its convenient use, significant support community, and interactive coding environment. We use the standard diagonalization techniques to determine all eigensolutions of the Hamiltonian matrix, and perform all calculations at double precision unless otherwise specified.

References

[1] Bruce R. Barrett, Petr Navràtil, and James P. Vary. Ab initio no core shell model. *Prog. Part. Nucl. Phys.*, 69:131–181, 2013. doi: 10.1016/j.ppnp.2012.10.003.

[2] P. Maris, J. P. Vary, and A. M. Shirokov. Ab initio no-core full configuration calculations of light nuclei. *Phys. Rev. C*, 79:014308, Jan 2009. doi: 10.1103/PhysRevC.79.014308. URL https://link.aps.org/doi/10.1103/PhysRevC.79.014308.

[3] M. A. Caprio, P. Maris, and J. P. Vary. Coulomb-sturmian basis for the nuclear many-body problem. *Phys. Rev. C*, 86:034312, Sep 2012. doi: 10.1103/PhysRevC.86.034312. URL https://link.aps.org/doi/10.1103/PhysRevC.86.034312.

[4] Jouni Suhonen. *From Nucleons to Nucleus*. Theoretical and Mathematical Physics. Springer, Berlin, Germany, 2007. ISBN 9783540488613, 9783540488590. doi: 10.1007/978-3-540-48861-3. URL http://www-spires.fnal.gov/spires/find/books/www?cl=QC793.3.S8S84::2007.

[5] Petr Navrátil, Sofia Quaglioni, Guillaume Hupin, Carolina Romero-Redondo, and Angelo Calci. Unified ab initio approaches to nuclear structure and reactions. *Phys. Scripta*, 91(5):053002, 2016. doi: 10.1088/0031-8949/91/5/053002.

[6] Ch. Constantinou, M. A. Caprio, J. P. Vary, and P. Maris. Natural orbital description of the halo nucleus^{6}He. *Nucl. Sci. Tech.*, 28(12):179, 2017. doi: 10.1007/s41365-017-0332-6.

[7] Gianina Alina Negoita. Ab initio nuclear structure theory. Master's thesis, Iowa State University, 2010.

[8] Alexander Tichai, Julius Müller, Klaus Vobig, and Robert Roth. Natural orbitals for ab initio no-core shell model calculations. *Phys. Rev. C*, 99:034321, Mar 2019. doi: 10.1103/PhysRevC.99.034321. URL https://link.aps.org/doi/10.1103/PhysRevC.99.034321.

[9] G Puddu. A new single-particle basis for nuclear many-body calculations. *Journal of Physics G: Nuclear and Particle Physics*, 44(10):105104, sep 2017. doi: 10.1088/1361-6471/aa8234. URL https://doi.org/10.1088%2F1361-6471%2Faa8234.

[10] Paolo Amore. A variational sinc collocation method for strong-coupling problems. *Journal of Physics A: Mathematical and General*, 39(22):L349–L355, may 2006. doi: 10.1088/0305-4470/39/22/l01. URL https://doi.org/10.1088%2F0305-4470%2F39%2F22%2Fl01.

[11] A. M. Shirokov, A. I. Mazur, S. A. Zaytsev, J. P. Vary, and T. A. Weber. Nucleon-nucleon interaction in the j-matrix inverse scattering approach and few-nucleon systems. *Phys. Rev. C*, 70:044005, Oct 2004. doi: 10.1103/PhysRevC.70.044005. URL https://link.aps.org/doi/10.1103/PhysRevC.70.044005.

[12] P. Maris, J. P. Vary, and A. M. Shirokov. Ab initio no-core full configuration calculations of light nuclei. *Phys. Rev. C*, 79:014308, Jan 2009. doi: 10.1103/PhysRevC.79.014308. URL https://link.aps.org/doi/10.1103/PhysRevC.79.014308.

[13] Hasan M. Aktulga, Chao Yang, Esmond G. Ng, Pieter Maris, and James P. Vary. Improving the scalability of a symmetric iterative eigensolver for multi-core platforms. 26, 11 2014.

[14] Pieter Maris, Masha Sosonkina, James P. Vary, Esmond Ng, and Chao Yang. Scaling of ab-initio nuclear physics calculations on multicore computer architectures. *Procedia Computer Science*, 1(1):97 – 106, 2010. ISSN 1877-0509. doi: https://doi.org/10.1016/j.procs.2010.04.012. URL http://www.sciencedirect.com/science/article/pii/S187705091000013X. ICCS 2010.

[15] James P Vary, Pieter Maris, Esmond Ng, Chao Yang, and Masha Sosonkina. Ab initio nuclear structure - the large sparse matrix eigenvalue problem. *Journal of Physics: Conference Series*, 180(1):012083, 2009. URL http://stacks.iop.org/1742-6596/180/i=1/a=012083.

[16] Meiyue Shao, H. Metin Aktulga, Chao Yang, Esmond G. Ng, Pieter Maris, and James P. Vary. Accelerating nuclear configuration interaction calculations through a preconditioned block iterative eigensolver. *Computer Physics Communications*, 222:1 – 13, 2018. ISSN 0010-4655. doi: https://doi.org/10.1016/j.cpc.2017.09.004. URL http://www.sciencedirect.com/science/article/pii/S0010465517302904.

[17] James P. Vary et al. Ab Initio No Core Shell Model with Leadership-Class Supercomputers. In *Proceedings, International Conference Nuclear Theory in the Supercomputing Era (NTSE-2016): Khabarovsk, Russia, September 19-23, 2016*, pages 15–35, 2018.

[18] E. Caurier and F. Nowacki. Present Status of Shell Model Techniques. *Acta Physica Polonica B*, 30:705, March 1999.

[19] Calvin W. Johnson, W. Erich Ormand, and Plamen G. Krastev. Factorization in large-scale many-body calculations. *Computer Physics Communications*, 184(12):2761 – 2774, 2013. ISSN 0010-4655. doi: https://doi.org/10.1016/j.cpc.2013.07.022. URL http://www.sciencedirect.com/science/article/pii/S0010465513002518.

[20] Noritaka Shimizu. Nuclear shell-model code for massive parallel computation, "KSHELL". 2013.

[21] B.A. Brown and W.D.M. Rae. The shell-model code nushellx@msu. *Nuclear Data Sheets*, 120:115 – 118, 2014. ISSN 0090-3752. doi: https://doi.org/10.1016/j.nds.2014.07.022. URL http://www.sciencedirect.com/science/article/pii/S0090375214004748.

CHAPTER 3. BASIS REGULARIZATION AND ITS CORRECTION

The physics of the Universe functions at all scales simultaneously and coherently, but attempting to model physical phenomena in the same way is a daunting and generally unfeasible task. Moreover, the approximate independence of physical laws at different scales makes such an endeavor very unappealing and largely unnecessary. Indeed, one would be woefully hard-pressed to use QCD to predict, say, the trajectory of a boulder thrown by a trebuchet. Similarly, the forces of gravity are largely irrelevant to modeling how a nucleon is held together.

Thus, when constructing models historically, scientists have always defined (often implicitly) the scales at which a model will be effective. After all, one doesn't need to know how the particles that make up a boulder interact to model its macroscopic projectile motion, and trying to define such motion at the level of quark interactions would be an enormous and grossly unfeasible effort. Naturally then, restricting the scales of our models is only sensible, and largely required for their feasibility. For a long time, the assumption was that accurate model treatments should (and always "could" for that matter) represent a subset of physical phenomena correctly in a complete and self-consistent way. If any nonphysical conclusions could be deduced, one assumed the model description must be flawed somehow. It is only somewhat recently that the full ramifications of considering only a limited range of scales have begun to be formally identified, and a more nuanced perspective has developed.

In contemporary variational calculations of nuclear eigenfunctions, one aims to select a trial wavefunction that best exploits the features of the Hamiltonian under investigation, and then adjusts the basis parameters to optimize the resolution and consequently minimize the energy. Indeed, as we've seen in Fig. (2.1), there is clearly a predictable pattern to how results are dependent on the HO basis parameters. The effects of the FBA on the representation of wavefunctions, operators, and (consequently) calculated observables are sometimes referred to as a form of regularization,

while methods that counteract these basis truncation effects by redefining the operator matrix are considered a form of renormalization. Both processes were historically important precursors to the development of EFT.

The concepts of regularization and renormalization originally arose in the context of QFT, where one modifies (or "regularizes") the expression of divergent contributions from loop diagrams to an observable by introducing a parameter (often called a regulator or cutoff) to make the contribution finite. The regularized quantity remains divergent for certain values of the regulator, and is therefore only considered physically meaningful within a certain interval of the regulator's value. The classic example is in QED where one tries to calculate the mass-energy of an electron and finds treating it as a point particle would give it an infinite inertia. This therefore requires the introduction of a regulator (that turns out to be the electron's finite radius) for the calculation to be physically meaningful.

Naturally, the process of regularization makes the contributions from loop diagrams dependent on the regularization scale, and, being a model artifact, this is generally undesirable. Thus, regularization is generally followed by renormalization to remove this dependence, where one recognizes that the seemingly divergent terms are in reality the actual, measurable physical quantities, and therefore one redefines (or "renormalizes") these quantities. One standard example is considering an electron with a given mass m in QFT. QFT dictates that there is a cloud of virtual particles around the electron, and these virtual particles (and the interactions between them) make the electron behave as though it has a different mass than originally stated. Thus, in this case, renormalization serves to replace the original mass with a corrected mass and recognize that this "renormalized mass" is the actual experimentally-measurable quantity.

While highly controversial for decades, the need for these methods in physical theories is now generally viewed to reflect the limited scales the model is designed to predict, and that allowing the introduction of regulators in a model is required to acknowledge the possibility of new/undescribed physics at other scales the model doesn't consider. In one sense then, the need for regularization can be seen as a consequence of both incomplete knowledge and the attempt at modeling phenomena

in a finite interval of scale. Put in a different light, the appearance of nonphysical terms are a consequence of how representing physical phenomena within a limited range of scales is, in a very real sense, an innately nonphysical treatment outside that limited range.

Returning to the topic of basis truncation effects, one might wonder what regularization has to do with the FBA, as the two processes may appear somewhat unrelated. However, there is an important parallel between the two: just as adding a regulator restricts what range of scales will give physically meaningful results in QFT, the FBA (implicitly) restricts what range of scales the basis expansion (and consequently the representations of wavefunctions and operators it is used to define) will be physically meaningful. Thus, while the circumstances and motivations are very different, the ultimate effect of imposing the FBA is the similar to imposing one or more regulators (two in the HO basis), and this is why it is sometimes referred to as "basis regularization". Similarly, "matrix renormalization" in this context involves redefining operator matrices to better account for the effects imposed by the aforementioned basis regularization.

While using this diction provides a convenient parallel to some well-understood Physics concepts, there is an important distinction between the two that must be made: the process of regularization and renormalization in QFT apply to *models* (i.e. the NMBP), whereas the basis regularization and matrix renormalization we are considering are relevant to the *model approach* (i.e. the NCSM) used to perform calculations. This may seem a minor distinction, but has become significant as different computational approaches have been developed for solving the same model problem. Thus, while we shall use these terms in the following, one should keep in mind how they are distinct from the conventional forms of regularization and renormalization in Physics.

In this chapter, we shall discuss the significance of the FBA in Nuclear Structure and some of the methods by which it may be compensated. We begin by examining the impact of the FBA on the 2N system under the HO basis, and define the two regulators it imposes in Section 3.1. Next, we explain how this formal description may be used in NCFC extrapolation to estimate the converged NCCI results with a statistically-defined extrapolation uncertainty estimate in Section 3.2. We conclude

the chapter by introducing two renormalization schemes for improving the convergence of observables in NCSM calculation and investigate their implementation in the 2N system in Section 3.3.

3.1 Basis regularization and emergent scales in the 2N system

We define the presence of basis regularization in the example of the 2N system and define the basis regulators used to describe it. Throughout, we shall focus on the radial part of the wavefunction depicted in Eq. (2.24), as that is the part relevant to the scales for which the finite basis (and thus the representations of wavefunctions and operators) is physically meaningful. We shall switch between plotting in momentum and coordinate space depending on the scenario, though the same observations can be made in either representation.

We first establish the sources of basis regularization and define regulators characterising the HO basis in Subsection 3.1.1. Second, we describe emergent scales of the NMBP in Subsection 3.1.2.

3.1.1 Infra-red and ultraviolet regulators

The FBA, in the context of the HO basis, implicitly restricts the scales for which the representations of wavefunctions and operators are meaningful. Great strides in understanding the nature of these effects have been made, and this understanding has been used to predict how the FBA impacts observable results.

Before we consider 2N wavefunctions, we recall the behavior of the HO basis functions themselves by considering the examples shown in Fig. (3.1), where we introduce the wave number $k \equiv p/\hbar$. The relevant region of what scales these functions can meaningfully approximate is defined by the domain over which the oscillations occur. Borrowing some language used for the visible spectrum to facilitate discussion, we refer to the left boundary in momentum space (i.e low-momentum or long-range) of this domain the "infra-red" (IR) cutoff L_{IR} of the function, and the right boundary in momentum space (i.e. high-momentum or short-range) the "ultraviolet" (UV) cutoff Λ_{UV}. Naturally, for plots in coordinate-space, these two cutoffs will switch sides.

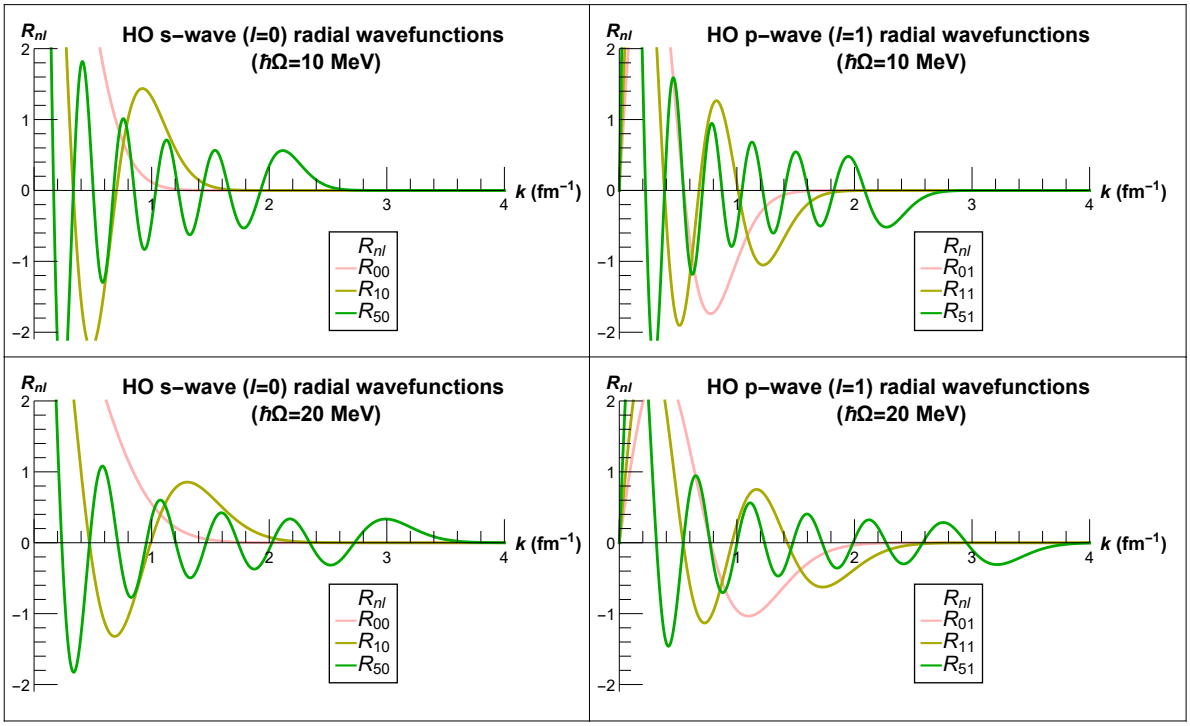

Figure 3.1 Some example HO basis s-wave (left) and p-wave (right) radial wavefunctions (Eq. (2.24)) with basis scale $\hbar\Omega = 10$ MeV (top) and $\hbar\Omega = 20$ (bottom) plotted in momentum space in terms of wave number k. The $n = 0, 1, 5$ states are shown in light red, yellow, and green, respectively. One observes increasing n extends the active domain of the wavefunction in both directions, while increasing $\hbar\Omega$ warps and shifts the active domain to the right (i.e. to larger energy scales).

We can see that as both n and l increase (i.e. as $N_{\max}$ increases), the domain of the oscillations (and consequently the domain on which the basis expansion is physically meaningful) widens in both directions. So the cutoffs associated with a given finite basis will depend on the highest HO excitation in that basis. On the other hand, as $\hbar\Omega$ increases from the upper to lower plots, we see the domain of the oscillations extend over higher momentum scales, and both ends of that domain are shifted to the right.

While both $N_{\max}$ and $\hbar\Omega$ are clearly functioning as "regulators" of the basis regularization, it is generally more convenient to discuss regulators that define the explicit momentum scales in which results using the finite basis are physically meaningful. Thus, we'd like to define the basis regulators L_{IR} and Λ_{UV} corresponding to our choice of HO basis. To make such an estimate, one can consider how the momentum of a classical particle in a HO state is largest at the origin, where all the particle's energy is kinetic. For the most excited state of a given basis, this would mean for a particle of mass μ,

$$\frac{\hbar^2 k_{\max}^2}{2\mu} = (N_{\max} + 3/2)\,\hbar\Omega, \rightarrow k_{\max} = \sqrt{2\,(N_{\max} + 3/2)\,\frac{\mu\Omega}{\hbar}}, \,, \tag{3.1}$$

where $k_{\max}$ is the maximum momentum. Similarly, we expect the same state to define a maximum radial extent a classical particle cannot exceed when the state has only potential energy, or

$$r_{\max} = \sqrt{2\,(N_{\max} + 3/2)\,\frac{\hbar}{\mu\Omega}}\,, \tag{3.2}$$

where $r_{\max}$ is the radial extent. We notice in these definitions that increasing $N_{\max}$ increases both quantities, while increasing $\hbar\Omega$ increases $k_{\max}$, but decreases $r_{\max}$. Looking back at Fig. (3.1), we see $r_{\max}$ and $k_{\max}$ do indeed behave the same way as the domain boundaries of HO wavefunction oscillations.

Since we wish to define outer limits for the scales of a basis, it is natural to define our basis regulators a few shells higher than what is dictated by $N_{\max}$, which has been observed a better estimate in a number of studies [1–4]. One generally does this by defining the quantity $N_i = N_{\max} + i$,

where i is an integer. In our case, we use $i = 3$ to mark the third shell higher than $N_{\max}$ and the corresponding extremes defined by Eqs. (3.1),(3.2). This value of i is observed in Ref. [5] to provide better estimates of the IR and UV limits for light nuclei.

Thus, from these considerations we define the IR and UV HO basis regulators (where we adopt the HO coordinate-space length scale definition $b = \sqrt{\frac{\mu\Omega}{\hbar}}$) :

$$L_{\mathrm{IR}} = \sqrt{(2N_{\mathrm{i}} + 3)}b^{-1}\,, \tag{3.3}$$

$$\Lambda_{\mathrm{UV}} = \sqrt{(2N_{\mathrm{i}} + 3)}b\,. \tag{3.4}$$

The basis regulators serve to define the scales a basis can meaningfully model wavefunctions and operators.

The former description reflects many of the same arguments for defining the HO basis regulators as provided in a series of closely related works [1, 2, 6, 3, 4, 7], and, barring some notational differences, matches the basis regulators defined in Ref. [2, 5]. While we shall proceed with our basis regulators defined thus, one should note that variations exist for them, as different arguments can be made on what best defines the "physically meaningful" boundaries imposed by basis regularization. The alternatives generally involve modifying the number of shells above $N_{\max}$ one uses in the regulators' definition.

To demonstrate these regulators and better understand the basis regularization they entail, it is useful to view some examples of extreme IR and UV basis regularization effects. Thus, we consider two basis expansions of the deuteron ground-state wavefunction using a chiral N3LO potential that has been renormalized to the scale of $\lambda_{\mathrm{2N}} = 2.0$ fm through SRG (a process discussed in Subsection 3.3.2) in Fig. (3.2). On the left we see the well-converged deuteron ground-state wavefunction alongside its heavily IR-regularized representation in coordinate space, and the same wavefunction on the right except now alongside its heavily UV-regularized representation in momentum space. The vertical dashed lines mark the respective IR and UV cutoffs.

We see that the two basis regulators given in Eqs. (3.3), (3.4) appear to be fairly good estimates for the limited scales a finite HO basis can meaningfully model. The oscillations leading up to

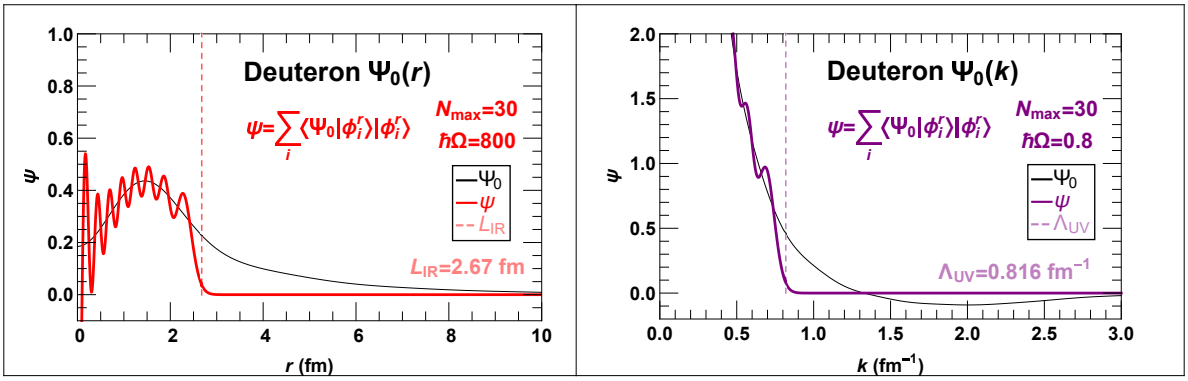

Figure 3.2 Two cases of extreme basis regularization using the example case of the deuteron ground-state wavefunction Ψ_0 (black) when using N3LO chiral EM500 2N interaction [8]. Left panel shows the heavily IR-regularized representation $\psi_{\rm IR}$ (red) of the deuteron ground-state wavefunction in coordinate space, while the right panel shows the heavily UV-regularized representation ψ_{UV} (violet) in momentum space. The basis parameters used are shown on the right side of each plot in the corresponding color. Vertical, dashed lines mark the value for the given basis of the regulators $L_{\rm IR}$ (light red) and Λ_{UV} (light violet), and defined by Eqs. (3.4), (3.4). Their value is shown in the bottom right for the basis depicted in the plot they appear.

the rapid falloff reflect the exaggerated weight for the highest basis function in the regularized wavefunction. That is, since the most excited HO state is defined over the widest domain, it is the only function that overlaps the scales closest to the cutoffs, and therefore its overlap with the actual wavefunction appears unnaturally large due to the normalization condition. In essence, the extreme basis regularization observed here can be viewed as the consequence of a poorly-conditioned optimization problem, where one tries to recreate the wavefunction as best as possible with the basis states available.

3.1.2 Emergent scales of the NMBP

When defining the boundaries of the HO basis regularization, we wish to capture what we will call the "emergent scales" of the problem, by which we mean the scales that are of particular significance to the physical system being approximated. Naturally, the emergent scales are governed

by the underlying dynamics given by the Hamiltonian, and are distinguished by their independence from any model approach.

For example, if we define λ_{2N} as the maximum momentum scale of a given 2N potential, it follows that for an accurate representation of the wavefunction and potential, we at least require

$$\lambda_{\mathrm{2N}} < \Lambda_{\mathrm{UV}} \,. \tag{3.5}$$

Similarly, one would expect the IR regulator should at least extend beyond the nuclear radius, R_A, or

$$R_A < L_{\mathrm{IR}} \,. \tag{3.6}$$

While reasonable estimates, the former conditions are, in practice, usually insufficient to guarantee converged Nuclear Structure results (particularly for the IR regularization). This is largely the consequence of having defined our basis regulators from a classically-motivated description, when, being of a quantum nature, nuclear wavefunctions and HO wavefunctions possess non-zero asymptotic regions, or "tails", in both coordinate and momentum space.

To discuss these effects, we will consider the momentum-space tail first. While the maximum UV scale of nuclear potentials does not always fall off quickly, realistic interactions from χEFT and SRG-renormalized interactions generally do have fast falloffs. This is because the former require a built-in regulator during their construction to be physically meaningful, while the latter impose a similar[1] cutoff effect through a unitary scale transformation (which we describe in Subsection 3.3.2). In both cases, the effective potential exhibits super-Gaussian falloff beyond the imposed momentum cutoff, and consequently the UV convergence becomes rapid in momentum space once Eq. (3.5) becomes satisfied. The subsequent corrections then primarily come from the much more gradual falloff of the IR tail of the wavefunction in coordinate space.

Indeed, if we observe the plots of the ground-state energy in terms of $\hbar\Omega$ depicted on the right panel of Fig. (2.1), one notices that the optimal $\hbar\Omega$ (i.e. the $\hbar\Omega$ giving the energetic minimum) for

[1] Though both methods impose a cutoff, note their impact on the potential in other ways is very different.

a given $N_{\max}$ starts at higher $\hbar\Omega$ values but drifts to lower values as $N_{\max}$ increases. This reflects how, once $N_{\max}$ is large enough to capture the UV convergence, subsequent increases in $N_{\max}$ will shift the minimum to lower values of $\hbar\Omega$ to capture more of the coordinate-space tail, since the additional shifts to the UV regulator granted by increasing $N_{\max}$ are largely superfluous beyond the potential's momentum cutoff.

The aforementioned pattern is only part of the picture one usually sees in light nuclei, as what one sees depends on both the potential and the range of $N_{\max}$ being considered, and we've used a very soft interaction. Specifically, In cases of "hard" interactions with significant high-momentum correlations, the minimum usually first shifts to higher values of $\hbar\Omega$ before shifting back to lower values as seen in Fig. (2.1). This is because the impact of the improved coverage over the UV tail dominates in harder potentials at low $N_{\max}$, and the minimum only shifts back to lower values once UV convergence is reached. Thus, because JISP16 is so soft, the effects of the improved UV coverage initially only balances the effects of the improved IR coverage, and the initial shift of the minimum to higher $\hbar\Omega$ values is suppressed. For more examples of this pattern and its discussion, see Refs. [5, 6, 3].

Thus, we see the basis IR cutoff ultimately dominates the remaining basis regularization effects at higher $N_{\max}$. However, defining a strict IR condition for the scale at which results will be converged proves somewhat difficult. Specifically, one observes a new emergent scale of the problem that makes the scale required for convergence potential- and state-dependent: the convergence of a wavefunction will depend on its associated binding energy, as dictated by the usual quantum mechanics considerations for the tails of bound state wavefunctions. That is, being a quantum system, the coordinate-space tail of nuclear wavefunctions extend beyond the nuclear radius, and only fall off exponentially. This differs significantly from the coordinate-space tails of HO basis functions, which fall off rapidly and can be compared to the rapid fall-off at an infinite barrier or "box" around the system.

The position of this effective barrier defines a new scale inherent to a finite HO basis, which can be approximated by determining the slope of the most excited basis function at the boundary of

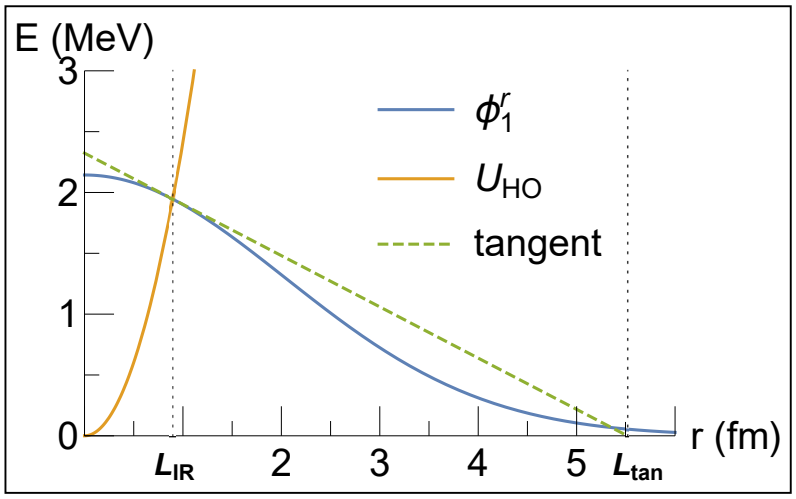

Figure 3.3 Graphical description for a simple estimate of the cutoff scale of the HO tail. The yellow line depicts an HO potential, while the blue depicts the corresponding ground state. The dashed green line is the tangent of the ϕ_1^r at its intersection with the HO potential, which corresponds to the $L_{\rm IR}$ cutoff. The tangent's y-intercept provides an estimate of where the HO tail begins falling rapidly.

the potential and using its tangent. For instance, if we consider Fig. (3.3) we see a HO potential overlaid with its ground-state wavefunction. Clearly, taking the tangent of the wavefunction at the boundary gives a fairly good estimate of the hard-wall cutoff of a quantum HO state. In truth, such an estimate can be seen as just the NLO correction term of an expansion about the classical boundary, and, as discussed in Refs. [6, 3], one arrives at a more accurate estimate of the IR HO basis cutoff

$$L_t \approx L_{IR} + 0.54437 b \sqrt[6]{(2N_{\rm max}+3)}\,. \tag{3.7}$$

So far we have only considered the cutoff in the context of the single-particle basis, and neglected any dependence on the details of the NCSM many-body basis. Instead, one can define a very precise IR length scale for the basis by equating the lowest eigenvalue of the intrinsic kinetic energy of the A-nucleon system in the NCSM many-body basis to that of A-nucleons in a $3(A-1)$-dimensional hyper-radial potential well, with a Dirichlet boundary condition for the corresponding hyper-radius. Being A-dependent, this process doesn't involve a closed-form expression like the former, and instead must

be determined through numerical calculations evaluated for a given system. While this approach won't be further discussed here, it proves remarkably effective for extrapolations in light nuclei [7, 9].

Much more can be said regarding basis regularization and its various subtleties. For the purposes of this work however, the former discussion serves to introduce all the relevant concepts that shall appear in both studies provided in Chapters 4 and 5, as well as the upcoming description of NCFC extrapolation.

3.2 NCFC extrapolation

We introduce the concept of NCFC extrapolation and its respective uncertainty estimation, and define the extrapolation approach used in Fig. (2.1). We discuss the effectiveness of these tools, and lay some of the foundations defining the extrapolations presented in Chapter 5.

One of the primary methods introduced by NCFC studies to augment NCCI calculation are the extrapolation of observables to the continuum limit by fitting the results varying with regards to the basis parameters under a specific functional form. Mentioned in Subsection 2.1.3, extrapolation proves particularly effective for the ground-state energy, due to consequences of the variational principle and the simple dependence on $N_{\max}$ and $\hbar\Omega$.

Multiple functional forms exist for extrapolating NCCI results for the ground-state energy, though the most recent are generally rooted in the study of basis regularization from the FBA [2, 6, 3]. Furthermore, while not discussed in this work, recent strides have generated ground-state energy and r^2 extrapolations through the use of artificial neural networks (ANNs) [10].

To discuss NCFC extrapolation, we consider the basic example provided by Fig. (2.1), which implements an extrapolation based on "extrapolation A5" described in Refs. [11, 9]. In this implementation, the extrapolation involves fitting the NCCI ground-state binding energy results with the functional form

$$f\left(N_{\max}\right) = a + b \cdot e^{-cN_{\max}} \tag{3.8}$$

where a, b, and c are fit parameters. The process involves performing a weighted χ^2 approach, which, in essence, uses the results at different basis scales simultaneously to form multiple fits that all converge to the same value. The fitting procedure for the global extrapolation proceeds as follows:

1. All results associated with $N_{\max} = 0$ are removed from consideration.

2. The basis scale (denoted here as $\hbar\Omega_0$) that gives the minimal eigenstate energy out of all the NCCI results being considered is identified.

3. Five results associated with basis scales $\hbar\Omega_0 + 2.5i$ for integers $1 \leq i \leq 5$ are retained for the global extrapolation; all other results are removed from consideration. The starting $N_{\max}$ result is set to $N_0 = 2$.

4. The results for $\hbar\Omega_i$ are used in a least-squares fit to Eq. (3.8), and the resulting b_i and c_i fit parameters are retained for later use as the initial values in the global extrapolation. The average is taken of the five a values obtained, and is similarly retained as the initial value of the converged energy.

5. The $\hbar\Omega_i$ results associated with basis cutoffs $N_0 + 2j$ for $0 \leq j \leq 4$ are identified. Each energy result, $E_i(N_j)$, with the exception of the $E_i(N_0)$ result, is weighted by the coefficient

$$w_{ij} \left(\frac{E_i(N_j) - f_i\left(N_j\right)}{E_i(N_j) - f_i\left(N_{j-1}\right)} \right)^2 , \tag{3.9}$$

   where $f_i\left(N_j\right) = a + b_i e^{c_i N_j}$. The $E_i(N_0)$ result is given the weight $w_{i0} = 3w_{i1}$.

6. N_0 is incremented by 2, and step 5 is repeated for all possible sets of five results with consecutive $N_{\max}$.

7. χ^2 is expressed as the sum of all weights w_{ij}, and a is variationally minimized by adjusting parameters b_i and c_i (10 variational parameters in total). The values determined in step 4 are used as the parameters' initial values, and constrained to 0.1% to 100,000% of that initial value

during the minimization process. The resulting value of a is used as the globally extrapolated energy.

8. Step 7 is repeated but now only with subsets of the same N_0. Half the maximum difference between the extrapolated values for a is used as the global extrapolation's uncertainty.

The described global extrapolation approach proves a fairly good estimate for the converged energy, and serves to demonstrate an example of what strategies NCFC extrapolations often involve. However, this particular example lacks some key features of those that appear in recent literature (that both make it simpler to perform as an example, and shall serve to highlight these features). First, the functional form, while broadly effective, does not reflect the extrapolations for the UV and IR basis regularization explicitly, which is ultimately what is being modeled. Contemporary fits, such as extrapolation $A5$ as described in Ref. [9], possess terms for the IR and UV basis regularization and are based in their theoretical description. Second, the given choice of uncertainty is somewhat arbitrary, and while it errs on the generous side, could potentially be better quantified by a stronger statistical interpretation of confidence.

3.3 Renormalization

We define two forms of renormalization and examine their implementation in the 2N system. First, we define and examine the Okubo-Lee-Suzuki (OLS) approach in Subsection 3.3.1. Second, we define and consider the Similarity Renormalization Group (SRG) approach in Subsection 3.3.2.

3.3.1 Okubo-Lee-Suzuki renormalization

For the present study, we consider only the OLS formulation employed by Ref. [12]. For a more complete discussion regarding the different effective Hamiltonian formulations and proofs of their equivalences, see Refs. [13–15].

The OLS renormalization procedure is a similarity transformation method for decoupling a given model space into component subspaces while preserving their eigenvalues. The process involves

constructing a unitary transform, U_{OLS}, which transforms the original model Hamiltonian of a given quantum system into two decoupled effective Hamiltonians.

We define the OLS technique for 2N matrix elements in a relative HO basis. The OLS transform bears its origins in Refs. [13–15], where it was originally proposed as a decoupling scheme for shell model calculations and plays a significant role in several approaches. In our case, it serves as a way to construct a unitary transform to decouple the vast majority of our basis states and allows us to define an effective Hamiltonian that retains a renormalized form of the lowest set of eigenstates, but in a much smaller basis dimension. Similarly, the transform defined by the Hamiltonian may be applied to define other effective operators that will retain the system's observables for that subset of eigenstates.

We begin by reviewing the original derivation of the OLS effective Hamiltonian as defined in Ref. [15]. From there we describe the construction of the unitary transform and provide qualitative insight on how it works. Finally, we offer some perspective on the finer details, challenges, and limitations of the technique by examining its implementation in the 2N system.

3.3.1.1 The OLS effective Hamiltonian

We briefly introduce the original OLS effective Hamiltonian treatment; see Refs. [15, 15, 15] for the complete derivation. We consider the solutions $\psi \in \Psi$ to the equation

$$H|\psi_i\rangle = E_i|\psi_i\rangle\,, \tag{3.10}$$

which we express in a HO basis $\Phi = \{\phi_1, \phi_2, ...\}$, where ϕ_i is the ith HO state. We introduce the projectors $P + Q = I$, which divide the given model basis into complementary subspaces $\Phi_P \oplus \Phi_Q = \Phi$ of dimensions d_P and d_Q, respectively, whose constituent states we generically denote ϕ_P and ϕ_Q. We want a similarity transform satisfying the decoupling condition

$$Qe^{-\omega}He^{\omega}P = 0\,, \tag{3.11}$$

where the operator ω transforms a Q-space state to a P-space state. For this equation to be valid, the Q-space components $\langle\phi_Q|\psi\rangle$ for a subset, Ψ_P, of the d_P eigenvectors $\psi \in \Psi_P$ must be representable by the P-space components as

$$\langle\phi_Q|\psi\rangle = \sum_u^{d_P} \langle\phi_Q|\omega|\phi_u\rangle\langle\phi_u|\psi\rangle \,, \tag{3.12}$$

where the sum is over basis states $\phi_u \in \Phi_P$. Assuming the chosen eigenvector elements define an invertible $d_P \times d_P$ matrix, the operator ω may be defined

$$\langle\phi_Q|\omega|\phi_P\rangle = \sum_i^{d_P} \langle\phi_Q|\psi_i\rangle\langle\tilde{\psi}_i|\phi_P\rangle \,, \tag{3.13}$$

for $\psi_i \in \Psi_P$ where $\tilde{\psi}_i$ denotes the inverse of $\langle\phi_P|\psi_i\rangle$. We may then express the elements of an effective P-space Hamiltonian, H_P ,

$$\langle\phi_P|H_P|\phi'_P\rangle = \sum_{u,v}^{dp}\sum_{i,j,k}^{dp} \langle\phi_P|\tilde{\psi}_k\rangle\langle\tilde{\psi}_k|\phi_u\rangle\langle\phi_u|\tilde{\psi}_i\rangle E_i \langle\tilde{\psi}_i|\phi_v\rangle\langle\phi_v|\tilde{\psi}_j\rangle\langle\tilde{\psi}_j|\phi'_P\rangle \,, \,, \tag{3.14}$$

where the summation indices u and v sum over basis states $\phi \in \phi_P$, while indices i, j, k sum over eigenstates $\psi \in \Psi_P$.

3.3.1.2 The OLS unitary transform

While the matrix elements expressed in Eq. (3.14) can be used to construct the effective Hamiltonian H_P (which is non-Hermitian in this form), it is more convenient and illustrative to consider the construction of the OLS transform. To do so, we return to the consideration of the original Hamiltonian H of dimension d, which is taken sufficiently large to achieve numerical convergence of the d_P eigenvalues and eigenvectors intended for defining the P-space. Notably, reaching convergence is not computationally expensive for 2N and 3N systems using modern technology.

By finding the eigenvectors ψ_i of the Hamiltonian, the unitary transform U diagonalizing H may be constructed as

$$U = \begin{pmatrix} \psi_{11} & \psi_{21} & \dots & \psi_{d1} \\ \psi_{12} & \psi_{22} & \dots & \psi_{d2} \\ \vdots & \vdots & \ddots & \vdots \\ \psi_{1d} & \psi_{2d} & \dots & \psi_{dd} \end{pmatrix}, \tag{3.15}$$

which applied to the Hamiltonian yields

$$H_{diag} = UHU^{\dagger} = \begin{pmatrix} E_1 & 0 & \dots & 0 \\ 0 & E_2 & \dots & 0 \\ \vdots & \vdots & \ddots & \vdots \\ 0 & 0 & \dots & E_d \end{pmatrix}, \tag{3.16}$$

where H_{diag} is the diagonalized Hamiltonian.

We now re-introduce the projection operators P and Q, as discussed previously. While the distribution of eigenstates between P & Q may be chosen arbitrarily, we define the P-space as containing the lower-lying energy spectra with dimension d_P and Q-space containing the higher-lying energy spectra, such that

$$H^P_{diag} = PH_{diag}P^{\dagger} = \begin{pmatrix} E_1 & 0 & \dots & 0 \\ 0 & E_2 & \dots & 0 \\ \vdots & \vdots & \ddots & \vdots \\ 0 & 0 & \dots & E_{d_p} \end{pmatrix}, \tag{3.17}$$

and

$$H^Q_{diag} = QH_{diag}Q^{\dagger} = \begin{pmatrix} E_{d_p+1} & 0 & \dots & 0 \\ 0 & E_{d_p+2} & \dots & 0 \\ \vdots & \vdots & \ddots & \vdots \\ 0 & 0 & \dots & E_d \end{pmatrix}, \tag{3.18}$$

where together the spaces of H^P_{diag} and H^Q_{diag} span the original model space, or

$$H^P_{diag} \oplus H^Q_{diag} = H_{diag}\,. \tag{3.19}$$

We now focus our attention solely on the P-space. In order to express the effective Hamiltonian of the P-space, the unitary transform U is projected into the P-space as

$$U^P \equiv PUP^\dagger = \begin{pmatrix} \psi_{11} & \psi_{21} & \cdots & \psi_{d_p 1} \\ \psi_{12} & \psi_{22} & \cdots & \psi_{d_p 2} \\ \vdots & \vdots & \ddots & \vdots \\ \psi_{1 d_p} & \psi_{2 d_p} & \cdots & \psi_{d_p d_p} \end{pmatrix}. \tag{3.20}$$

However, this projection leaves U^P no longer unitary. While numerous schemes exist to restore unitarity of this finite matrix (leading to different but unitarily equivalent representations), we follow the choice of [16, 17], and define the unitary transformation

$$\tilde{U}^P = \frac{U^P}{\sqrt{U^{P\dagger}U^P}}\,. \tag{3.21}$$

Just as in the case of the OLS effective Hamiltonian, note that this transform requires the norm in the denominator to be non-zero, which in turn requires no degenerate (or near-degenerate) eigenvectors in the P-space. Then an effective Hamiltonian in the P-space may then be constructed as

$$H^P_{eff} = \tilde{U}^{P\dagger} H^P_{diag} \tilde{U}^P = \tilde{U}^{P\dagger} PU H_{rel} U^\dagger P \tilde{U}^P\,. \tag{3.22}$$

The P-space component of the unitary transform U_{OLS} is thus be defined

$$U^P_{OLS} = \tilde{U}^P PU\,. \tag{3.23}$$

Following the same method, the Q-space component of U_{OLS} could be constructed, allowing the full unitary OLS transformation to be expressed as

$$U_{OLS} = \begin{pmatrix} U^P_{OLS} & 0 \\ 0 & U^Q_{OLS} \end{pmatrix}, \tag{3.24}$$

which applied to the original Hamiltonian would yield

$$U_{OLS} H U^\dagger_{OLS} = \begin{pmatrix} H_P & 0 \\ 0 & H_Q \end{pmatrix}. \tag{3.25}$$

In practice however, we are only interested in the lower-lying spectra found in the P-space, meaning only the construction of U^P_{OLS} is necessary (and, consequently, only requires the desired d_P eigenvectors of the Hamiltonian to be known). By constructing and applying only U^P_{OLS}, the subspace of interest may be decoupled from the full problem while preserving its lowest-lying eigenvalues.

Finally, the transform U^P_{OLS} constructed from the Hamiltonian may be similarly applied to other operators of the original model space to obtain effective P-space operators as

$$O^P_{eff} = U^P_{OLS} O U^{P\dagger}_{OLS}. \tag{3.26}$$

The inner products of energy eigenstates with these operators in the original model space will be similarly preserved by these effective operators for energy eigenstates in the P-space. In the case that the initial and final P-spaces are different (such as for a transition matrix element) the OLS transform must be calculated for each subspace independently. The effective transition operator may then be calculated as

$$O^P_{eff} = U^{P'}_{OLS} O U^{P\dagger}_{OLS}, \tag{3.27}$$

where $U^{P'}_{OLS}$ is the transform associated with the bra P-space while U^P_{OLS} is associated with the ket P-space.

3.3.1.3 OLS renormalization in the 2N system

We now employ an implementation of OLS renormalization on the 2N system in relative coordinates. Beyond introducing the concepts, this can be viewed as a supplement to the discussion provided by the published work provided in Chapter 4.

It is useful to start by considering how the Hamiltonian itself changes with OLS renormalization, and how it differs from the effects of basis regularization imposed by truncation. Thus, we begin by considering Fig. (3.4), where the 2N EM500 Hamiltonian's $^1S_0$ channel is plotted in k^2-space for both conventional $N_{\max}$ truncation and OLS renormalization. Below each given plot (excluding the leftmost), the change in energy

$$\Delta E_0 = E_0' - E_0 \tag{3.28}$$

corresponds to the difference between the original (or "bare") $N_{\max} = 60$ (far left) Hamiltonian's lowest $^1S_0$ excitation energy, E_0, and the energy E_0' calculated for the same state of the given truncated/renormalized Hamiltonian.

From just these few examples we can see that the lowest $^1S_0$ excitation energy of the bare Hamiltonian remains fairly-well preserved by OLS renormalization, especially compared to the result from a truncated Hamiltonian of the same matrix dimension, and this serves as a simple consistency check. Naturally, the precision at which OLS preserves the eigensystem depends directly upon the precision used in its implementation. For instance, the results displayed here reflect the OLS transform performed at machine precision in Mathematica (~16 digits); performing the same calculation at 40 digits of precision do not visibly change the plots, but gives $\Delta E_0 < 10^{-19}$ MeV for all the listed choices of d_P.

Despite the rather staunch differences in the ground-state energy, the truncated and renormalized Hamiltonians appear similar at a first glance, and the renormalization appears to retain much of the Hamiltonian's original structure. To be more specific, the diagonal bands observed reflect the kinetic energy operator's selection rules, and their presence appears to be left largely intact by our choice of OLS renormalization.

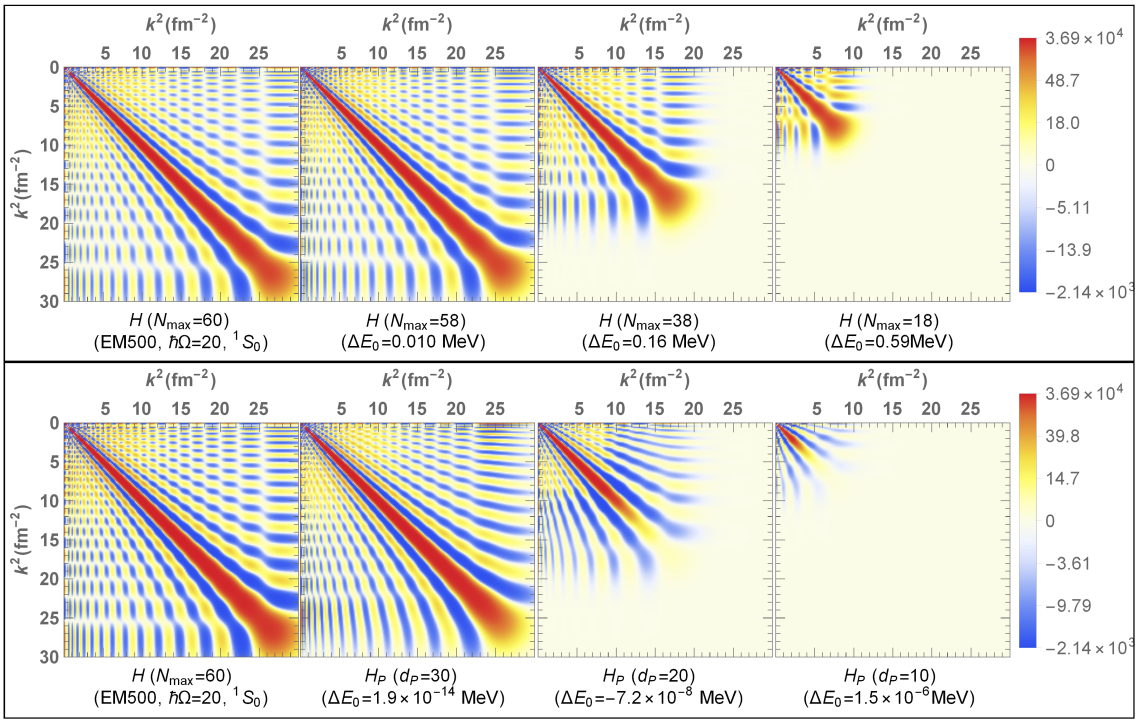

Figure 3.4 Plots of the realistic EM500 2N Hamiltonian expressed in the $\hbar\Omega = 20\,\mathrm{MeV}$ $^1\mathrm{S}_0$ HO basis channel and plotted in k^2-space as its basis dimension is reduced by $N_{\max}$ truncation (top) and OLS renormalization (bottom), from the original (or "bare") $N_{\max} = 60$ Hamiltonian on the far left to the $N_{\max} = 18$ (or equivalently $d_P = 10$) Hamiltonian on the far right. Shades of yellow to red denote positive (i.e. repulsive) magnitudes, while shades of blue denote negative (i.e. attractive) magnitudes. The color scale is non-linear, and is instead adjusted to maximize contrast. The energy shift ΔE_0 (see Eq. (3.28)) of the lowest $^1\mathrm{S}_0$ 2N excitation eigenenergy from the bare Hamiltonian is provided below the corresponding plot of the Hamiltonian. Notably, the OLS-renormalized Hamiltonians remains within six or more decimals of the bare Hamiltonian's lowest excitation energy.

However, a closer look reveals subtle differences between each vertical pair of panels that explain the source of the shifts in energy. Specifically, one notices the strong, repulsive diagonal band in the truncated Hamiltonian Hamiltonian is significantly diminished in the OLS renormalized Hamiltonian as d_P decreases, especially farther down the diagonal. This reflects how the renormalization is "redistributing" off-diagonal elements inward, especially towards the strong repulsive diagonal, which will be particularly significant for the energies of higher excitations. Indeed, as the basis dimension falls, we see the highest momentum regions are being suppressed in general.

If we focus on the difference made by removing only the single most excited basis state through OLS, we notice that some of the "sharp" block-diagonal structure of the Hamiltonian has been "smoothed". In addition, some of the speckle pattern in the low-momentum off-diagonals disappears. The sharp contrast in contours over short spans in momentum space seen in the plot of the bare Hamiltonian reflects the selection rules of the kinetic energy, which is approximately the sole contribution beyond the UV range of the potential (which from Fig. (3.5), appears to be roughly $15\,\mathrm{fm}^{-2}$).

We can also see a distinct change in the shape of the interior repulsive region that is dominated by the potential in $d_P = 20$. To see this more clearly we may consider Fig. (3.5), which shows the OLS transform applied directly to the potential as $U^P_{OLS} V_{2N} U^{P\dagger}_{OLS}$ in the upper row, and the effective potential

$$V_{eff} = H_{eff} - PT_{rel}P\,, \tag{3.29}$$

shown in the lower row.

We see from the top row that, while many structural aspects of the kinetic energy operator remained unchanged by OLS, the structural changes to the potential appear far more significant. The range of the central attractive well appears enlarged at $d_P = 20$, and the repulsive barrier has a hard, square-like cutoff around $8\,\mathrm{fm}^{-2}$. It is particularly noteworthy that this cutoff is not the cutoff from the reduced basis size, which for the $d_P = 20$ basis used here is around $20\,\mathrm{fm}^{-2}$ according to Eq. (3.4). This would suggest a new scale emerges for the potential that is being imposed by OLS

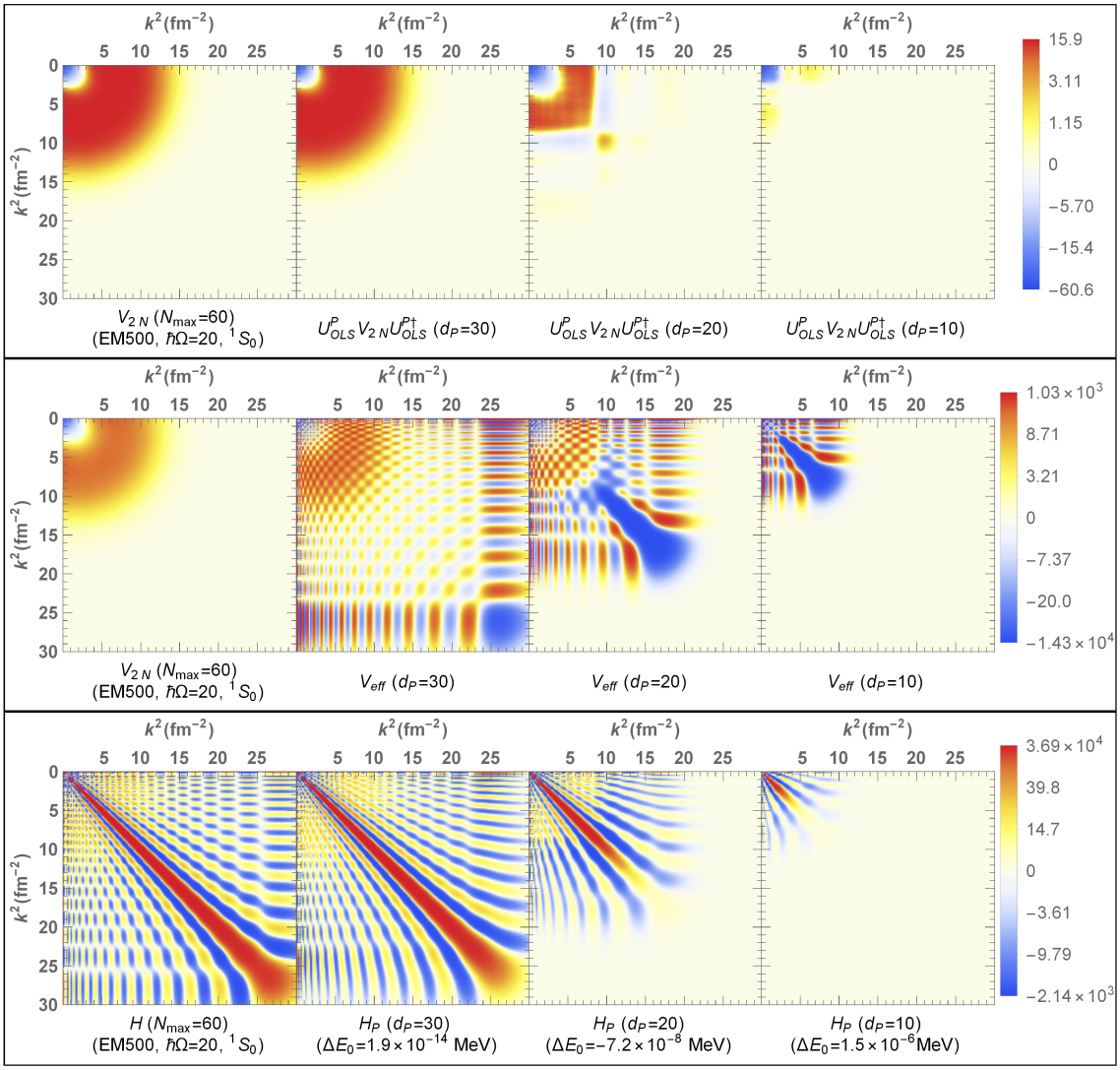

Figure 3.5 Plots of the realistic N3LO EM500 2N potential expressed in the $N_{\max} = 60$, $\hbar\Omega = 20\,\text{MeV}$ $^1\text{S}_0$ HO basis channel, plotted in k^2-space and renormalized with OLS for multiple choices of P-space dimension d_P, from the "bare" $d_P = 31$ potential on the far left to the $d_P = 10$ potential on the far right. Top row shows the quantity $U^P_{OLS} V_{2N} U^{P\dagger}_{OLS}$, whereas the middle shows Eq. (3.29). The Shades of yellow to red denote positive (i.e. repulsive) magnitudes, while shades of blue denote negative (i.e. attractive) magnitudes. The color scale is non-linear, and is instead adjusted to maximize contrast. The corresponding OLS effective Hamiltonians and energy shifts ΔE_0 (see Eq. (3.28)) shown in Fig. (3.4) are provided in the bottom row for completeness and pedagogical purposes. of the potential.

renormalization, which is likely linked to the range in momentum space (the implied P-space range) over which the phase shifts are preserved.

Meanwhile, the effective potential V_{eff}^{P} shown on the bottom row suggests the removal of only the highest HO excitation most significantly impacts the next highest HO excitation. Indeed, only a slight suppression of the kinetic energy operator can be seen by the traces left behind throughout the lower momentum regions upon removing the kinetic energy.

Much more can be observed regarding OLS renormalization in the 2N system, and can be found in Chapter 4. For now, we turn our attention to a second renormalization strategy: the SRG approach.

3.3.2 The Similarity Renormalization Group

We describe the SRG process for renormalizing 2N matrix elements in a relative basis. The SRG approach originates from Refs. [18, 19] of the 90s, and reflects many of the same key ideas regarding scale that have come to define a great deal of modern Nuclear Theory. The SRG process is centered around using a flow equation to iteratively and unitarily adjust the Hamiltonian using a given generator of scale transformations. While the method is quite versatile and the effects of the renormalization can be made to vary significantly based on what generator is used, we will focus on the common use of the Wilson generator (i.e. the kinetic energy) to boost the convergence speed with $N_{\max}$ of the eigenenergies by unitarily transforming the Hamiltonian such that large momentum changing interaction contributions are suppressed.

We begin by describing the SRG procedure. We then discuss aspects of the procedures computational implementation and offer some simple examples. We conclude by exploring the impact of the transform on the Hamiltonian and consider other aspects of the approach.

3.3.2.1 The SRG procedure

We review the SRG procedure; for a more complete description, see Refs. [20, 21]. For the bare Hamiltonian H we seek a similarity transform U_s with scale parameter s such that

$$H_s = U_s H_B U_s^\dagger \tag{3.30}$$

where H_s is an effective hamiltonian that is band-diagonal with width $\lambda = s^{-\frac{1}{4}}$ (thus, $\lim_{\lambda\to\infty} H_s \to H$). Taking the derivative of Eq. (3.30) gives the infinitesimal form of the transformation (or "flow equation"):

$$\frac{dH_s}{ds} = \frac{dU_s}{ds} H_B U_s^\dagger + U_s H_B \frac{dU_s^\dagger}{ds} = \frac{dU_s}{ds} U_s^\dagger H_s + H_s U_s \frac{dU_s^\dagger}{ds} \tag{3.31}$$

We note that for unitary operators

$$\frac{d}{ds}\left(U_s U_s^\dagger\right) = \frac{d}{ds}(I) = 0 \to \frac{dU_s}{ds} U_s^\dagger = -U_s \frac{dU_s^\dagger}{ds} \tag{3.32}$$

Let's denote this anti-hermitian quantity $\eta_s = \frac{dU_s}{ds} U_s^\dagger$. Then our flow equation becomes

$$\frac{dH_s}{ds} = [H_s, \eta_s] \ , \tag{3.33}$$

where η_s is the generator of infinitesimal changes in scale. Solving the flow equation depicted by Eq. (3.33) is the primary goal of SRG. The equation is equivalent to a system of ordinary differential equations (ODEs), which may be solved to determine the limit of H_s when $s \to \infty$. While doing so, one may similarly transform other operators O alongside the Hamiltonian as

$$\frac{dO_s}{ds} = [O_s, \eta_s] \ , \tag{3.34}$$

where the evolution of η_s is defined by its evolution in Eq. (3.33) (this is why the operators must be evolved alongside the Hamiltonian).

For a given implementation, we must choose our generator; what we choose will decide what the effective Hamiltonian will evolve to. Some common choices are:

- $\eta_s = [H_s,\, T]\,, \rightarrow$ band diagonal (sometimes called "Wilson generators")
- $\eta_s = \left[(H_s)_{diag}\,,\, (H_s)_{offd}\right]\,, \rightarrow$block diagonal by channel (sometimes called "Wegner generators")
- $\eta_s = [H_s,\, PH_sP + QH_sQ]\,, \rightarrow$ block diagonal for P & Q (like OLS)

We'll use the first option for our examples: the kinetic energy operator T. Naturally, in this case, only the potential of the Hamiltonian will be relevant in iterations of the flow equation, as T self-commutes.

Finally, it is also often convenient to reparametrize the flow equation with $s \equiv \frac{1}{\lambda^4}$, so that the flow parameter λ corresponds directly to the imposed cutoff in momentum space, and $\lambda = \infty$ corresponds to the original Hamiltonian. Both parameters are commonly used in the literature, and will be used interchangeably in the upcoming section.

3.3.2.2 Example implementation methods for SRG renormalization

In practice, solving Eq. (3.33) involves evolving the system of ODEs defined by each element of the matrix. One way to do this is to rephrase the equation purely as an iterative matrix problem, where one takes infinitesimal steps in the scale ds such that the transform may be approximated $U_s \sim 1 - \eta_s ds$. Phrased in terms of an infinitesimal shift in the momentum scale $d\lambda$, a single iteration then just involves calculating

$$V_{\lambda - d\lambda} = V_\lambda - [H_\lambda,\, \eta_\lambda]\, ds = V_\lambda + [H_\lambda,\, [V_\lambda,\, T]] \left(\frac{1}{(\lambda - d\lambda)^4} - \frac{1}{\lambda^4} \right) . \tag{3.35}$$

The resulting $V_{\lambda - d\lambda}$ is then put back in place of V_λ and the process is repeated for $V_{\lambda - 2d\lambda}$ and so on.

While a conceptually simple approach, implementing it numerically proves problematic, as it is very difficult to predict how large the finite step sizes of $d\lambda$ need to be to avoid building up error and

voiding the transform's unitarity. Furthermore, the required step size changes for different values of λ as well as for different potentials. Thus, this sort of method (as well as any other numerical time-step approach) becomes a somewhat difficult problem to generalize due to the need to identify the appropriate step size.

Equivalently, the flow equation may be written as a system of coupled ODEs as

$$\frac{dH_{s,ij}}{ds} = [H_s, [H_s, T]]_{ij} = \sum_{l,k} [2H_{il}T_{ik}H_{kj} - H_{il}H_{ik}T_{kj} - T_{il}H_{ik}H_{kj}] \ , \tag{3.36}$$

and the system can be solved analytically. Mathematica proves particularly well-suited to such a task, so this is the method that is used for the results of the following section. However, this too ultimately proves fairly limited in the matrix sizes that may be considered in a timely manner, and one generally must rely on state-of-the-art numerical ODE solvers for the high-accuracy renormalization desired in Nuclear Structure.

3.3.2.3 SRG in the 2N system

We consider an example implementation of SRG in the 2N system. Just as in Subsection 3.3.1, we find it most demonstrative to examine how the potential itself changes with SRG renormalization as depicted in Fig. (3.6). To better allow comparison with what we observed in Fig. (3.5), we once again consider the 2N EM500 potential represented in the $^1S_0$ channel plotted in k^2-space, where once again we include the change in energy defined by Eq. (3.28) below each renormalized plot.

Where OLS evolved the potential to lower momenta in general, SRG presses the potential into a diagonal band, or, equivalently, restricts the maximum momentum transfer the state's occupant can undergo. While this does not strictly reduce the dimension of the basis necessary to include the entire potential, it does make the inclusion of the higher HO excitations unnecessary for the lower energy eigenstates of the system, since the eigenstates of the renormalized system are now dominated by only a small subset of adjacent HO basis states. In practice, this means the wavefunction (and consequently the renormalized operator observables) will converge much faster.

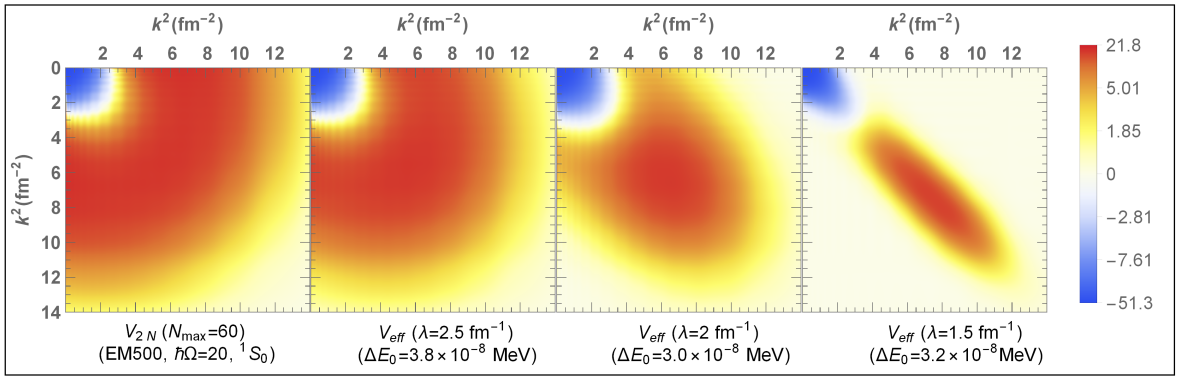

Figure 3.6 Plots of the EM500 potential expressed in the $\hbar\Omega = 20\,\text{MeV}$ $^1S_0$ HO basis channel and plotted in k^2-space as it is evolved numerically by SRG (with a Wilson generator) to the momentum cutoff λ, from the "bare" $N_{\max} = 60$ potential (left) to $\lambda = 1.5\,\text{fm}^3$(right). Shades of yellow to red denotes positive (i.e. repulsive) magnitudes, while shades of blue denote negative (i.e. attractive) magnitudes. The color scale is non-linear, and is instead adjusted to maximize contrast. The total shift from the lowest $^1S_0$ 2N excitation eigenenergy is provided below the plot of each renormalized potentials.

3.3.2.4 Further developments for implementing the SRG

Despite the flexibility granted by being able to tailor the generator used for a given system, performing the SRG method by solving Eqs. (3.33), (3.34) as described in the former examples proves somewhat restrictive. First, the system of ODEs being solved roughly doubles in size for each operator one wishes to renormalize. Further, operators often don't evolve at the same rates and usually don't all require the same level of accuracy for different interval values of the flow parameter, both of which increase the likelihood of the ODEs becoming stiff. Second, the use of a high-order ODE solver is crucial for high-accuracy implementations of SRG, as any significant accumulation of error during each time-step destroys the unitarity of the transformation. However, state-of-the-art solvers often require the storage of a dozen or more copies of the solution vector at any given time, and this can become memory intensive. This is particularly true for many-body implementations of SRG like the *ab initio* MR-IMSRG approach employed in Chapter 5, and proves the primary computational bottleneck of the method [21]. Finally, the need to renormalize operators alongside the Hamiltonian, beyond being mildly inconvenient, proves particularly troublesome for transition

operators when the initial and final systems do not share the same model space (nor, consequently, the same Hamiltonian matrix).

The most direct solution to these problems would be to simply solve the unitary transform U_s, much like what is done in OLS, as then the transform can be applied to operators independently. From the description given before, U_s may be defined

$$U_s = \mathcal{T} e^{\int_0^s ds' \eta_{s'}} = \lim_{N\to\infty} \prod_{i=0}^{N} e^{\eta_{s_i} \delta s_i} = \sum_n \frac{1}{n!} \int_0^s ds_1 ... \int_0^s ds_n \mathcal{T}\{\eta_{s_1} ... \eta_{s_n}\} \tag{3.37}$$

where $\mathcal{T}$ orders operators by descending scale. However, trying to calculate U_s as shown in Eq. (3.37) is generally highly impractical. Fortunately, methods have been developed to use the Magnus expansion [22, 23] to recast the problem such that, instead of solving the system of ODEs for the Hamiltonian and other operators, one expresses the transform $U_s \equiv e^{\Omega_s}$ and solves

$$\frac{d\Omega_s}{ds} = \sum_{n=0}^{\infty} \frac{B_n}{n!} \left[\Omega_s, \eta_s\right]^{(n)} , \tag{3.38}$$

where the nested commutators are given by

$$\left[\Omega_s, \eta_s\right]^{(0)} = \eta_s \, , \tag{3.39a}$$

$$\left[\Omega_s, \eta_s\right]^{(n)} = \left[\Omega_s, \left[\Omega_s, \eta_s\right]^{(n-1)}\right] , \tag{3.39b}$$

and $B_{n=0,1,2,\cdots}$ are the Bernoulli numbers $\{1, -1/2, 1/6, \cdots\}$. The unitary transform may then be used to transform any operators of interest using the Baker-Campbell-Hausdorff formula

$$e^{\Omega_s} O e^{-\Omega_s} = \sum_{n=0}^{\infty} \frac{1}{n!} \left[\Omega_s, O\right]^{(n)} . \tag{3.40}$$

This formulation of SRG possesses a number of convenient advantages over the high-precision evolution of Eqs. (3.33), (3.34), but also introduces some new problems. For a complete description see Refs. [24, 22, 23]. This strategy is also a crucial element for the Magnus formulation of IMSRG calculation used in the MR-IMSRG benchmark calculations of Chapter 5.

References

[1] S. N. More, A. Ekström, R. J. Furnstahl, G. Hagen, and T. Papenbrock. Universal properties of infrared oscillator basis extrapolations. *Phys. Rev.*, C87(4):044326, 2013. doi: 10.1103/PhysRevC.87.044326.

[2] S. A. Coon, M. I. Avetian, M. K. G. Kruse, U. van Kolck, P. Maris, and J. P. Vary. Convergence properties of ab initio calculations of light nuclei in a harmonic oscillator basis. *Phys. Rev. C*, 86:054002, Nov 2012. doi: 10.1103/PhysRevC.86.054002. URL https://link.aps.org/doi/10.1103/PhysRevC.86.054002.

[3] R. J. Furnstahl, G. Hagen, T. Papenbrock, and K. A. Wendt. Infrared extrapolations for atomic nuclei. *J. Phys.*, G42(3):034032, 2015. doi: 10.1088/0954-3899/42/3/034032.

[4] S. König, S. K. Bogner, R. J. Furnstahl, S. N. More, and T. Papenbrock. Ultraviolet extrapolations in finite oscillator bases. *Phys. Rev.*, C90(6):064007, 2014. doi: 10.1103/PhysRevC.90.064007.

[5] E. D. Jurgenson, P. Maris, R. J. Furnstahl, P. Navràtil, W. E. Ormand, and J. P. Vary. Structure of p-shell nuclei using three-nucleon interactions evolved with the similarity renormalization group. *Phys. Rev.*, C87(5):054312, 2013. doi: 10.1103/PhysRevC.87.054312.

[6] R. J. Furnstahl, G. Hagen, and T. Papenbrock. Corrections to nuclear energies and radii in finite oscillator spaces. *Phys. Rev.*, C86:031301, 2012. doi: 10.1103/PhysRevC.86.031301.

[7] K. A. Wendt, C. Forssén, T. Papenbrock, and D. Sääf. Infrared length scale and extrapolations for the no-core shell model. *Phys. Rev.*, C91(6):061301, 2015. doi: 10.1103/PhysRevC.91.061301.

[8] D. R. Entem and R. Machleidt. Accurate charge dependent nucleon nucleon potential at fourth order of chiral perturbation theory. *Phys. Rev.*, C68:041001, 2003. doi: 10.1103/PhysRevC.68.041001.

[9] Ik Jae Shin, Youngman Kim, Pieter Maris, James P. Vary, Christian Forssén, Jimmy Rotureau, and Nicolas Michel. Ab initio no-core solutions for ^{6}Li. *J. Phys.*, G44(7):075103, 2017. doi: 10.1088/1361-6471/aa6cb7.

[10] Gianina Alina Negoita et al. Deep learning: Extrapolation tool for ab initio nuclear theory. *Phys. Rev.*, C99(5):054308, 2019. doi: 10.1103/PhysRevC.99.054308.

[11] P. Maris, J. P. Vary, and A. M. Shirokov. Ab initio no-core full configuration calculations of light nuclei. *Phys. Rev. C*, 79:014308, Jan 2009. doi: 10.1103/PhysRevC.79.014308. URL https://link.aps.org/doi/10.1103/PhysRevC.79.014308.

[12] James P. Vary, Robert A. M. Basili, Weijie Du, Matthew Lockner, Pieter Maris, Soham Pal, and Shiplu Sarker. Effective operators in two-nucleon systems. *Phys. Rev.*, C98(6):065502, 2018. doi: 10.1103/PhysRevC.98.065502.

[13] Kenji Suzuki and Shyh Yuan Lee. Convergent Theory for Effective Interaction in Nuclei*). *Progress of Theoretical Physics*, 64(6):2091–2106, 12 1980. ISSN 0033-068X. doi: 10.1143/PTP.64.2091. URL https://doi.org/10.1143/PTP.64.2091.

[14] Kenji Suzuki. Construction of Hermitian Effective Interaction in Nuclei: General Relation between Hermitian and Non-Hermitian Forms. *Progress of Theoretical Physics*, 68(1):246–260, 07 1982. ISSN 0033-068X. doi: 10.1143/PTP.68.246. URL https://doi.org/10.1143/PTP.68.246.

[15] Kenji Suzuki and Ryoji Okamoto. Degenerate Perturbation Theory in Quantum Mechanics. *Progress of Theoretical Physics*, 70(2):439–451, 08 1983. ISSN 0033-068X. doi: 10.1143/PTP.70.439. URL https://doi.org/10.1143/PTP.70.439.

[16] Nadezda A. Smirnova, Bruce R. Barrett, Youngman Kim, Ik Jae Shin, Andrey M. Shirokov, Erdal Dikmen, Pieter Maris, and James P. Vary. Effective interactions in the *sd* shell. 2019.

[17] E. Dikmen, A. F. Lisetski, B. R. Barrett, P. Maris, A. M. Shirokov, and J. P. Vary. Ab initio effective interactions for sd-shell valence nucleons. *Phys. Rev.*, C91(6):064301, 2015. doi: 10.1103/PhysRevC.91.064301.

[18] Stanisław D. Głazek and Kenneth G. Wilson. Renormalization of hamiltonians. *Phys. Rev. D*, 48:5863–5872, Dec 1993. doi: 10.1103/PhysRevD.48.5863. URL https://link.aps.org/doi/10.1103/PhysRevD.48.5863.

[19] Franz Wegner. Flow-equations for hamiltonians. *Annalen der Physik*, 506(2):77–91, 1994. doi: 10.1002/andp.19945060203. URL https://onlinelibrary.wiley.com/doi/abs/10.1002/andp.19945060203.

[20] Sergio Szpigel and Robert J. Perry. The Similarity renormalization group. pages 59–81, 2000.

[21] Heiko Hergert, Jiangming Yao, Titus D. Morris, Nathan M. Parzuchowski, Scott K. Bogner, and Jonathan Engel. Nuclear Structure from the In-Medium Similarity Renormalization Group. *J. Phys. Conf. Ser.*, 1041(1):012007, 2018. doi: 10.1088/1742-6596/1041/1/012007.

[22] S. Blanes, F. Casas, J.A. Oteo, and J. Ros. The magnus expansion and some of its applications. *Physics Reports*, 470(5):151 – 238, 2009. ISSN 0370-1573. doi: https://doi.org/10.1016/j.physrep.2008.11.001. URL http://www.sciencedirect.com/science/article/pii/S0370157308004092.

[23] Wilhelm Magnus. On the exponential solution of differential equations for a linear operator. *Communications on Pure and Applied Mathematics*, 7(4):649–673, 1954. doi: 10.1002/cpa.3160070404. URL https://onlinelibrary.wiley.com/doi/abs/10.1002/cpa.3160070404.

[24] T. D. Morris, N. Parzuchowski, and S. K. Bogner. Magnus expansion and in-medium similarity renormalization group. *Phys. Rev.*, C92(3):034331, 2015. doi: 10.1103/PhysRevC.92.034331.

CHAPTER 4. EFFECTIVE OPERATORS IN TWO-NUCLEON SYSTEMS

Modified from a manuscript published in *Physical Review C*

James P. Vary, Robert Basili, Weijie Du,

Matthew Lockner, Pieter Maris, Soham Pal and Shiplu Sarker

4.1 Abstract

Effective Hamiltonians and effective electroweak operators are calculated with the Okubo-Lee-Suzuki formalism for two-nucleon systems. Working within a harmonic oscillator basis, first without and then with a confining harmonic oscillator trap, we demonstrate the effects of renormalization on observables calculated for truncated basis spaces. We illustrate the renormalization effects for the root-mean-square point-proton radius, electric quadrupole moment, magnetic dipole moment, Gamow-Teller transition and neutrinoless double-beta decay operator using nucleon-nucleon interactions from chiral Effective Field Theory. Renormalization effects tend to be larger in the weaker traps and smaller basis spaces suggesting applications to heavier nuclei with transitions dominated by weakly-bound nucleons would be subject to more significant renormalization effects within achievable basis spaces.

4.2 Introduction

Precision studies of electroweak properties of nuclei have become of great interest to complement major advances underway in experimental nuclear physics. As an example, significant experimental and theoretical efforts are aimed at searches for neutrinoless double-beta ($0\nu2\beta$) decay which require significant investments in new experimental facilities and in theoretical advances. Our limited goal here is to use solvable two-nucleon systems within a configuration-interaction (CI) approach in order to explore the dependence of electroweak operators on the CI basis-space truncation when

evaluating nuclear properties. Information on the size of these effects can help interpret previous studies and guide plans for calculations in larger nuclei.

We select systems of two nucleons interacting via realistic nucleon-nucleon (NN) interactions both in free space and in a harmonic oscillator (HO) trap for investigating renormalization effects on a suite of electroweak properties. These systems are numerically solvable in a large HO basis space providing high precision results for comparison with approximate results. This allows us to map out the effects arising from the correlations governed by different interactions, as well as the effects due to basis space truncation and the effects linked with the length scale of the environment, the trap. To accurately calculate these effects we adopt the Okubo-Lee-Suzuki (OLS) method [1–3] to derive the basis truncation dependence of effective interactions and operators. By comparing matrix elements of these derived effective operators with those from a truncated treatment of the original operators, we observe the truncation effects (conversely the renormalization effects) on each electroweak operator for each basis space and for each confining HO trap. While most effects tend to be in the range of a few percent, the effects on the $0\nu2\beta$ matrix element can be above a factor of two for some systems. Such cases suggest a careful treatment of renormalization effects must be implemented for $0\nu2\beta$ decay matrix elements in limited basis spaces. Fortunately, these same OLS methods are adaptable to more realistic applications as in the case of the No-Core Shell Model (NCSM) [4–7] and to valence space effective interactions as well [8].

This work may be viewed in the context of a related pioneering work that extensively investigated the deuteron and its electromagnetic form factors with renormalization group methods [9]. The importance of maintaining consistency in the renormalization of both the Hamiltonian and all other observables is the theme we share. The renormalization method, interactions, observables and presence of a trap distinguish our work from Ref. [9].

4.3 Theoretical framework

4.3.1 Many-body systems

We seek to solve a Hamiltonian H eigenvalue problem expressed in a suitable basis and, once the eigenvectors are obtained, to evaluate matrix elements of additional observables O. For nuclear physics applications, such as the NCSM, the resulting matrix for H is infinite dimensional. With truncation, the matrix of H becomes numerically tractable, allowing the study of results as a function of the finite basis parameters in order to estimate the converged results and their uncertainties. For the NCSM, we express H in terms of the relative kinetic energy operator $T_{\rm rel}$ acting between all pairs of nucleons in the A–nucleon system and an interaction term V that may include multi-nucleon interactions as

$$H = T_{\rm rel} + V. \tag{4.1}$$

By adopting a complete basis of Slater determinants, $|\Phi_j\rangle$ for A nucleons, developed from a chosen single-particle basis, we express the complete space problem as a matrix eigenvalue problem. That is, the eigenvalues E_k and eigenstates $|\Psi_k\rangle$, expanded in our complete basis of Slater determinants, obey the equations

$$H|\Psi_k\rangle = E_k|\Psi_k\rangle \tag{4.2}$$

$$|\Psi_k\rangle = \sum_j A_{kj}|\Phi_j\rangle, \tag{4.3}$$

where A_{kj} denotes the expansion coefficient.

The selection of the complete single-particle basis is flexible but we will follow a popular choice and adopt the three-dimensional HO due to its well-studied analytical properties that facilitate numerical applications and the retention of the underlying symmetries of H [7]. We take the neutron and proton mass m to be the same (938.92 MeV, their average measured mass), so that the

only length scale in the HO single-particle basis can be expressed in terms of the HO energy $\hbar\Omega$ as

$$b = \sqrt{\frac{\hbar}{m\Omega}}. \tag{4.4}$$

4.3.2 Finite matrix truncation approach

In practical applications, it is advantageous to define the many-body truncation with $N_{\max}$, the maximum of the total HO quanta in the retained Slater determinants above the minimum total HO quanta for the A nucleons [7]. A quantum of the HO single-particle state is twice the radial quantum number n plus the orbital quantum number l. That minimum total HO quanta for the A nucleons also depends on the number of neutrons N and protons Z that comprise the system. Zero is the minimum total HO quanta for the two-nucleon systems addressed in this work.

We define the P–space (or "model space") as the basis space retained by this $N_{\max}$ truncation. The infinite-dimensional space beyond this $N_{\max}$ truncation is called the Q–space. For a sufficiently large $N_{\max}$, some observables are seen to converge in very light nuclei for interactions which do not couple strongly to high momentum states and when computational resources are sufficient. For example, using a chiral N^{2}LO NN interaction [10, 11], the ground-state (gs) energy of ^{6}Li has been calculated [12–14] in a sequence of HO basis spaces. With extrapolation to the complete basis, the result is $-31.0(2)$ MeV [14]. Here, the parenthesis specifies the uncertainty as 200 keV in the extrapolation. The basis space truncation for the largest finite basis employed in the extrapolation is $N_{\max} = 18$. At $N_{\max} = 18$ and $\hbar\Omega = 28$ MeV the gs energy, which is also a variational upper bound of the exact result, is already -29.928 MeV, i.e., about 1.1 MeV above the extrapolated result. For comparison, the experimental gs energy is -31.995 MeV [15].

However, other observables, such as the root-mean-square (rms) point-proton radius and electric quadrupole transitions, converge poorly up through $N_{\max} = 18$ [16]. For long-range observables such as the rms point-proton radius, the theoretical results are insufficiently converged to provide directly a meaningful comparison with experiment. For example, with extrapolations, the rms point-proton radius for ^{6}Li, has significant uncertainties [16].

For all these reasons, it may be advantageous to soften the interactions and to promote improved convergence of the eigenvalue problem. As we explain in the next section, this softening, or renormalization of the interaction, also necessitates renormalizing the operators corresponding to these other observables. That is, we need to consistently derive the effective operators for all observables in the chosen model space.

4.3.3 Effective Hamiltonian and operators

Once the complete basis space and the P–space are defined, we can address the development of an effective Hamiltonian H_{eff} for the P–space that formally retains a subset of the eigenvalues of the complete space. We adopt the OLS method [1–3] which we briefly outline here. More details, including specifics for including three-nucleon interactions, are found in Ref. [7].

The formal structure of the OLS approach is visualized by first considering H in the complete basis space and defining the unitary transformation U that diagonalizes H to produce the Hamiltonian's spectral form H_d along with the P–space projection of U, which we denote W^P.

$$H_d := UHU^\dagger \tag{4.5}$$

$$W^P := PUP. \tag{4.6}$$

Provided that the projected eigenvectors form a complete set of linearly independent vectors in the P–space, we can then construct a finite basis transformation $\widetilde{U}^P$, which is unitary in the P–space, as

$$\widetilde{U}^P := \frac{W^P}{\sqrt{W^{P\dagger}W^P}}. \tag{4.7}$$

With this transformation, we define our H_{eff} for the P–space with

$$H_{\text{eff}} := \widetilde{U}^{P\dagger} H_d \widetilde{U}^P \tag{4.8}$$

$$= \widetilde{U}^{P\dagger} U H U^\dagger \widetilde{U}^P. \tag{4.9}$$

We denote the OLS transformation $U_{\rm OLS}$ by the combination

$$U_{\rm OLS} := \widetilde{U}^{P\dagger} U. \tag{4.10}$$

We define our P–space to accommodate the lowest set of eigenvalues of the original Hamiltonian though other choices are feasible, such as retaining states whose eigenvectors have the largest probabilities of P–space configurations. We furthermore note that $H_{\rm eff}$ is not unique since there is the freedom of a residual P–space unitary transformation that preserves H_d. Additional mathematical issues have been addressed in Ref. [17] such as the breakdown when linearly-dependent projected eigenvectors are encountered. We did not encounter this breakdown in the calculations reported in this work. A central issue for the current work is to investigate the effects of the corresponding transformation on the observables O needed to generate consistent renormalizations. That is, we define consistent effective operators

$$O_{\rm eff} := U_{\rm OLS} O U_{\rm OLS}^{\dagger} \tag{4.11}$$

for calculations of observables with the P–space eigenfunctions of $H_{\rm eff}$. [1]

While these steps provide the formal framework, the essential question of a practical implementation requires further discussion. In the NCSM, one introduces an auxiliary confining potential, which is later removed, and solves for the OLS transformations on a subset of the nucleons in the nucleus (typically two or three nucleons) in what is dubbed a "cluster approximation" [18, 7]. The derived few-nucleon effective interaction is designed to renormalize the strong few-nucleon correlations in the presence of other nucleons approximated by the auxiliary potential. This effective interaction is subsequently employed to define an A-nucleon effective Hamiltonian. The cluster approximation is guaranteed to produce the exact results as either the cluster size is increased to reach the full A-nucleon system or as the P–space truncation is removed. The two-nucleon cluster

[1] Note that we are addressing a P–space which generally includes eigenstates with different conserved quantum numbers. The $U_{\rm OLS}$ transformation will properly manage scalar operators that conserve the symmetries of H as well as non-scalar operators that may induce transitions between eigenstates.

approximation of the NCSM serves as a paradigm for introducing and solving the NN systems of this work. Our aim is to investigate the ramifications of this approach for effective electroweak operators derived in a manner consistent with the softened interaction.

To this stage, we have described the formal structure of the OLS method and we have discussed its applications within the NCSM. For the two-nucleon systems we address below, either without or with a HO trap, we apply the OLS approach in the relative coordinate system. Since the NN Hamiltonian is defined with the conserved symmetries of each NN partial wave (channel), we apply the OLS method to each NN channel independently. That is, we solve for individual OLS transformations in a relative HO basis of fixed total angular momentum, coupled spin, parity and charge – the conserved quantum numbers for each NN channel. Then, we calculate the effective non-scalar operators with OLS transformations from the NN channels required for that operator. In these applications, the length scale of Eq. (4.4) is defined with the reduced mass which we take to be 469.46 MeV for all NN channels.

4.4 Applications to two-nucleon systems

4.4.1 Deuteron ground state

We define an initial system to consist of two nucleons described by the H of Eq. (1) whose gs energy we investigate in this subsection. Motivated by the NCSM cluster approximation framework, we will define a second two-nucleon system in the next subsection that adds a confining HO interaction (trap). Both systems are numerically solvable. We refer to the numerical solutions of these two systems as their "exact" results and we present these results in the Appendix. Using graphical representations, we compare these exact results with solutions from a truncation approach and with solutions from an OLS effective Hamiltonian approach. We refer to the results from the truncation approach and the results from the OLS approach each as "model" results.

We adopt NN interactions from chiral Effective Field Theory (EFT) and we include the Coulomb interaction between proton pairs in the Hamiltonian. Specifically, we employ the NN interactions of the Low Energy Nuclear Physics International Collaboration (LENPIC) [10–14] which have been

developed for each chiral order up through N^{4}LO. These LENPIC interactions employ a semilocal coordinate-space regulator and we select the interactions with the regulator range $R = 1.0$ fm [13, 14]. We refer to these interactions as "LENPIC–X" where "X" defines the specific chiral order (LO, NLO, N^{2}LO, N^{3}LO or N^{4}LO). We also employ the chiral EFT interaction of Ref. [19] with momentum-space regulator 500 MeV which we refer to as "Idaho–N^{3}LO". All of these chiral EFT interactions are charge-dependent.

We consider the neutron-proton (np) system since the deuteron gs provides the only bound NN state. In particular, we solve for the deuteron gs energy for each interaction using three approaches. First, we obtain a high-precision result by diagonalizing the Hamiltonian in the coupled ${}^3S_1 - {}^3D_1$ channel in a very large HO basis ($N_{\max} = 400$) for three different values of the HO energy $\hbar\Omega$. We have verified that these gs energies produce the same result as the numerical solution of the Schrödinger equation to at least 5 significant figures [10, 11] in all cases. We refer to these results from diagonalization at $N_{\max} = 400$ as the "exact" results. One may view these exact results as creating a discretized approximation to the continuum and we note that the largest eigenvalues exceed 1 GeV in all cases investigated here. Second, we solve for the gs energy in the HO bases truncated at lower $N_{\max}$ values to produce model results for the simple truncation approach. Third, we solve for the OLS effective Hamiltonian at each value of $N_{\max}$ and $\hbar\Omega$, following the methods described above, to produce the model results for the OLS approach. We follow this same approach for the neutron-neutron (nn) and proton-proton (pp) channels needed for some of the transitions addressed in this work.

The model results of the truncation and OLS approaches are used to calculate their fractional difference with respect to our exact results for each observable (i.e., observables calculated with the $N_{\max} = 400$ wave functions) where the fractional difference, Fract. Diff., is defined as the scaled difference $(model - exact)/|exact|$. The Fract. Diff. results for the deuteron gs energy are presented as curves in Fig. (4.1) for a representative selection of our NN interactions. We do not show the results for LENPIC-LO since they are similar to the LENPIC–NLO results. Also, we do not show the LENPIC–N^{4}LO results which are similar to those of LENPIC–N^{3}LO.

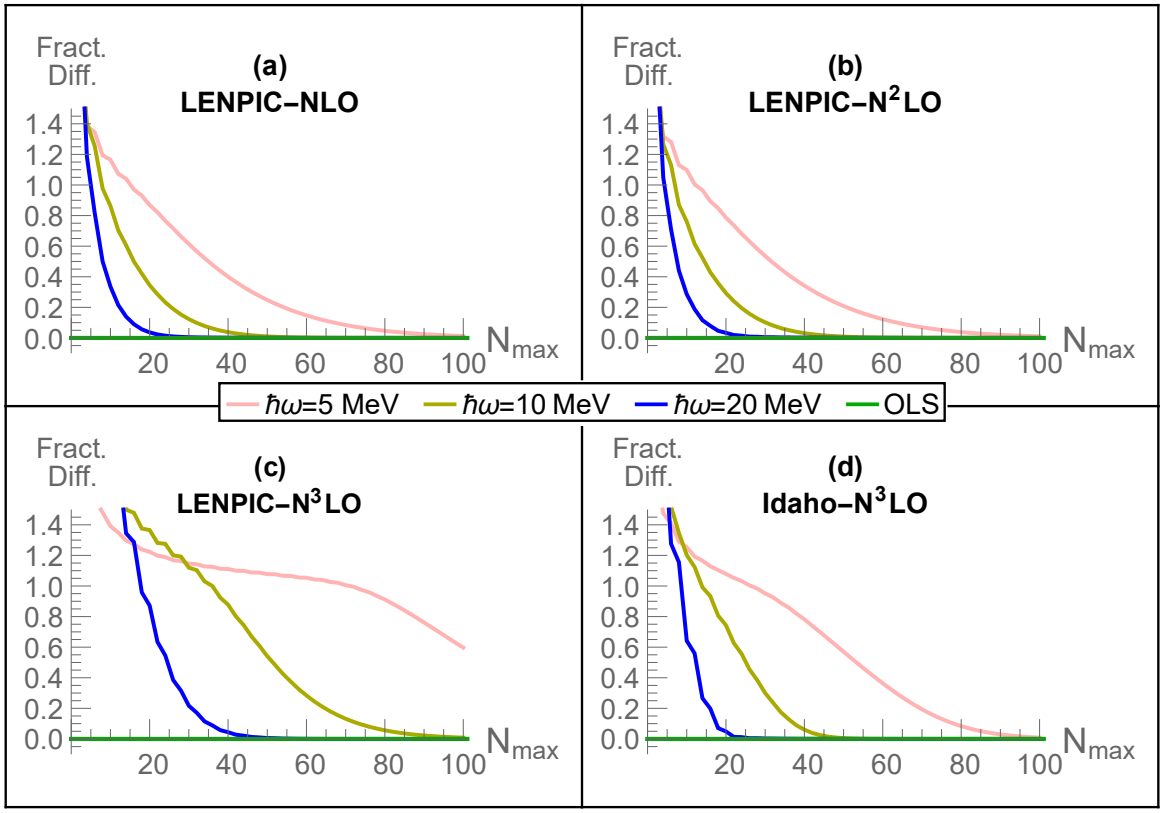

Figure 4.1 The fractional differences, where Fract. Diff. of an observable $= (model - exact)/|exact|$, for the deuteron gs energy at three values of the HO energy $\hbar\Omega$ as a function of the P–space limit $N_{\max}$. The model results from diagonalizing the P–space truncated Hamiltonian matrix produce Fract. Diff. curves that decrease towards zero with increasing $N_{\max}$ in accordance with the variational principle. The model results from diagonalizing the OLS–renormalized Hamiltonian matrix reproduce the exact results at each $N_{\max}$ to high precision, yielding flat and overlapping green lines for their Fract. Diff. plots in all cases. Panels (a), (b) and (c) correspond to the Hamiltonians constructed with the LENPIC chiral EFT interactions [10–14] at NLO, N^{2}LO and N^{3}LO, respectively. We employ the LENPIC interactions with coordinate-space regulator $R = 1.0$ fm. Panel (d) corresponds to the Hamiltonian constructed with the Idaho–N^{3}LO potential [19] with momentum-space regulator 500 MeV.

From the results in Fig. (4.1), we observe that the convergence rates for the truncation approach can depend significantly on the chiral order with the LENPIC NN interaction. In particular, there is a dramatic slowing of the convergence rates at N^{3}LO as seen in panel (c) compared to panels (a) and (b). The dependence of the convergence rates on the LENPIC chiral orders is also revealed in many-body observables where slower convergence leads to larger extrapolation uncertainties pSec4:Maris:2016wrd,Binder:2015mbz,Binder:2018pgl.

Comparing the LENPIC NN interaction results in Fig. (4.1) also reveals changing shapes of the convergence patterns with increasing chiral order for the bases using HO energy $\hbar\Omega = 5$ and 10 MeV. In particular, the case with $\hbar\Omega = 5$ MeV develops a region showing significantly reduced slope, nearly a plateau, with increasing $N_{\max}$ at N^{3}LO (panel (c)). The results for the Idaho–N^{3}LO interaction shown in panel (d) indicate convergence patterns intermediate to LENPIC–N^{2}LO (panel (b)) and LENPIC–N^{3}LO (panel (c)). These regions of reduced slope correspond to Fract. Diff ≈ 1.0 which defines a region of P–spaces where the lowest solution is transitioning between an unbound state and a bound state with increasing $N_{\max}$. Thus, for some interactions at lower values of $\hbar\Omega$, we observe a plateau-like behavior as seen in panels (c) and (d) of Fig. (4.1). In these same cases, after crossing over to a bound state solution, the convergence rate accelerates. We have investigated this plateau and have found a correlation with a changing feature of the wavefunction: while the solution is moving across the plateau with increasing $N_{\max}$ it is building up its d–state component from near zero to near its final value. When it nearly acquires its final value, the energy decreases to a bound state (Fract. Diff. falls below 1.0) and accelerates its convergence rate. We examined other interactions exhibiting this plateau in Fract. Diff. and found a similar correlation with buildup of the d–state probability. We anticipate that, at sufficiently low values of the basis $\hbar\Omega$, we would find a similar plateau with all realistic interactions for the deuteron.

The dependence of the convergence rate on the basis $\hbar\Omega$ for the truncation approach in Fig. (4.1) is systematic – from most rapid convergence at $\hbar\Omega = 20$ MeV to slowest at $\hbar\Omega = 5$ MeV. We have not sought to optimize the choice of $\hbar\Omega$ though that is often a point of interest in many-body

applications. Our interest here is rather to feature results for a range of choices of $\hbar\Omega$ that will be useful for our investigation of electroweak observables in the system of the following subsection.

The Fract. Diff. for the results of the OLS approach in Fig. (4.1) always remains at zero, to within our numerical precision, which is what one anticipates. That is, since the OLS approach should provide the exact gs energy in any basis space, these results serve as a verification of our numerical procedures. The OLS procedure reproduces that subset of eigenvalues of the complete problem compatible with the dimensionality fixed by $N_{\max}$, including eigenvalues lying high in the continuum. We verify the accuracy of the eigenvalues from the OLS approach by direct comparison with the corresponding subset of results from the complete problem for each set of P–space basis parameters. We have confirmed that our OLS eigenvalues agree with the respective subset of the exact eigenvalues to at least 6 significant figures.

We now present additional observables for the deuteron that represent baseline results for later comparison. In Fig. (4.2) we show the gs energy (panel (a)), rms point-proton radius (panel (b)), electric quadrupole moment (panel (c)) and magnetic moment (panel (d)) for the same set of 3 HO basis parameters as in Fig. (4.1) using the LENPIC–N^{2}LO interaction. Here, we expand the scale to see details of the results from $N_{\max} = 0 - 40$. Clearly, the results in the truncated basis exhibit strong deviations from their exact values and those deviations exhibit non-smooth behavior, such as sawtooth patterns, with increasing $N_{\max}$. The excursions in the electric quadrupole moment in panel (c) are especially prominent. These features represent the role of an s–state plus d–state combination that are added with each increase in $N_{\max}$ by 2 units. With the addition of two such combinations (increase $N_{\max}$ by 4 units) we include states with canceling asymptotic tails. This observation helps one to understand why results differing by 4 units in $N_{\max}$ follow a simpler trend in Fig. (4.2) – a trend visualized by the dotted line connecting the successive maxima and another dotted line connecting the successive minima of the sawtooth patterns. Such a visualization is also applied to the maxima and the minima of the sawtooth patterns of the other observables in Fig. (4.2), the rms radius (b) and magnetic moment (c). Note that the scale for the magnetic

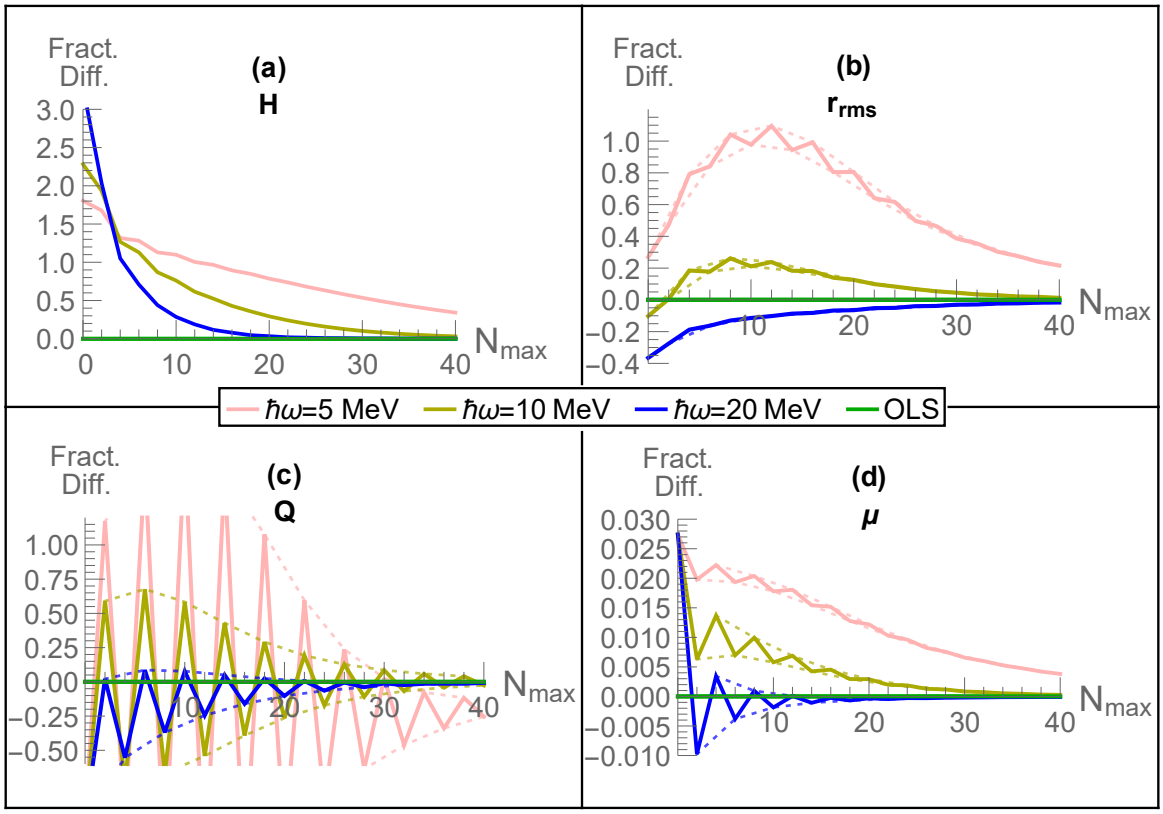

Figure 4.2 The fractional differences for a selection of deuteron properties at three values of the HO energy basis parameter $\hbar\Omega$ as a function of the P–space limit $N_{\max}$. Following the scheme of Fig. (4.1), we present the Fract. Diff. for the truncated basis calculations (three colored curves approaching zero at high $N_{\max}$) and for the OLS renormalized calculations (green curves all coincident with zero). All results are obtained with the LENPIC–N^{2}LO interaction with regulator $R = 1.0$ fm. The gs energy in panel (a) is an expanded version of the gs energy in panel (b) of Fig. (4.1). The rms point-proton radius $r_{\rm rms}$ appears in panel (b), the electric quadrupole moment Q in panel (c) and the magnetic moment μ in panel (d). The model results using the OLS transformation method reproduce the exact results at each $N_{\max}$ to high precision, yielding flat and overlapping green lines for their Fract. Diff. plots in all cases. The short dashed lines provide envelopes for results with sawtooth patterns.

moment is greatly enlarged relative to the other scales in Fig. (4.2) indicating it is rather insensitive to basis truncation effects.

Here again, the calculations of the effective operators with the OLS method, when employed with the OLS wave functions in the same P–space, provide the exact results to within 6 digits for each observable at each value of the trap. The OLS results are seen as the flat green lines at Fract. Diff. ≈ 0 in Fig. (4.2).

4.4.2 Two nucleons in HO trap – ground-state energy

For the purpose of investigating effective electroweak operators and gauging a range of representative behaviors anticipating future applications to finite nuclei, we augment the initial system of the previous subsection with the addition of a confining interaction or trap. We adopt a HO confining potential and separate the effects of the trap into center-of-mass and relative motion. Since the center-of-mass motion factorizes, its wavefunction is an exact HO eigenstate and not affected by the NN interaction acting in relative coordinates. We subsequently consider only the relative motion of the two nucleons in the confining HO potential of relative motion and employ the Hamiltonian:

$$H = T_{\rm rel} + V + \frac{1}{2}\mu\Omega^2 r^2 \tag{4.12}$$

For these systems, we adopt HO energies for the confining interaction which match the basis values of $\hbar\Omega = 5,\ 10,$ and 20 MeV introduced above.

In this second system, the HO trap simulates the role of the nuclear medium in which the two-nucleon subsystem is embedded. For applications where we expect weakly bound nucleons to dominate the electroweak properties, we provide results with the confining strength parameter $\hbar\Omega = 5$ MeV. Then we progress to simulate contributions from moderately bound to deeply bound nucleon pairs with $\hbar\Omega = 10$ and 20 MeV, respectively. We also note that the addition of the HO trap emulates the mathematical framework for the two-body cluster approximation in the NCSM where the HO trap is added during the development of the effective Hamiltonian and then removed

at the stage of defining the effective interaction [7]. Such a treatment of the HO trap as a pseudo-potential is known to improve convergence in NCSM applications with the OLS approach using the cluster approximation. We therefore anticipate that studying the two-nucleon system with various HO traps, including its electroweak properties, will provide insights into renormalization effects on observables in future NCSM applications to finite nuclei.

For simplicity, we elect to retain only a subset of the LENPIC NN interactions for this second system. In panel (a) of Fig. (4.3) we show the Fract. Diff. for the gs energy in the ${}^3S_1 - {}^3D_1$ channel for the three different traps. Again, we list the exact results in the Appendix. Note that, for this second system, the exact results depend on the HO strength parameter $\hbar\Omega$. The convergence rate for results of the truncation approach is again systematic – slowest with $\hbar\Omega = 5$ MeV and fastest with $\hbar\Omega = 20$ MeV. However, the scale for Fract. Diff. in panel (a) of Fig. (4.3) is much larger than in Fig. (4.1). Nevertheless, the results of the OLS approach again provide agreement with the exact gs energy results over all choices of P–space as evident by the coincident flat green lines at Fract. Diff. $= 0$.

4.4.3 Two nucleons in HO trap – electromagnetic observables

We now turn our attention to additional observables in this second system where we again aim to compare the results of the truncation approach with those of the OLS approach. We note that a consistent OLS treatment of various long-range observables has been investigated in the past and results of truncation versus OLS approaches have been shown to be in the range from a few percent to about ten percent [4–6]. Our aim here is to investigate both electromagnetic and weak observables over a wide range of basis spaces but in the limited two-nucleon system. In the end, we find large effects for matrix elements of some observables in cases with traps having small HO energies and/or in cases having small $N_{\max}$ values. This suggests that truncation effects are more severe and renormalization effects are more important when approaching observables involving weakly bound states and transitions involving resonance states.

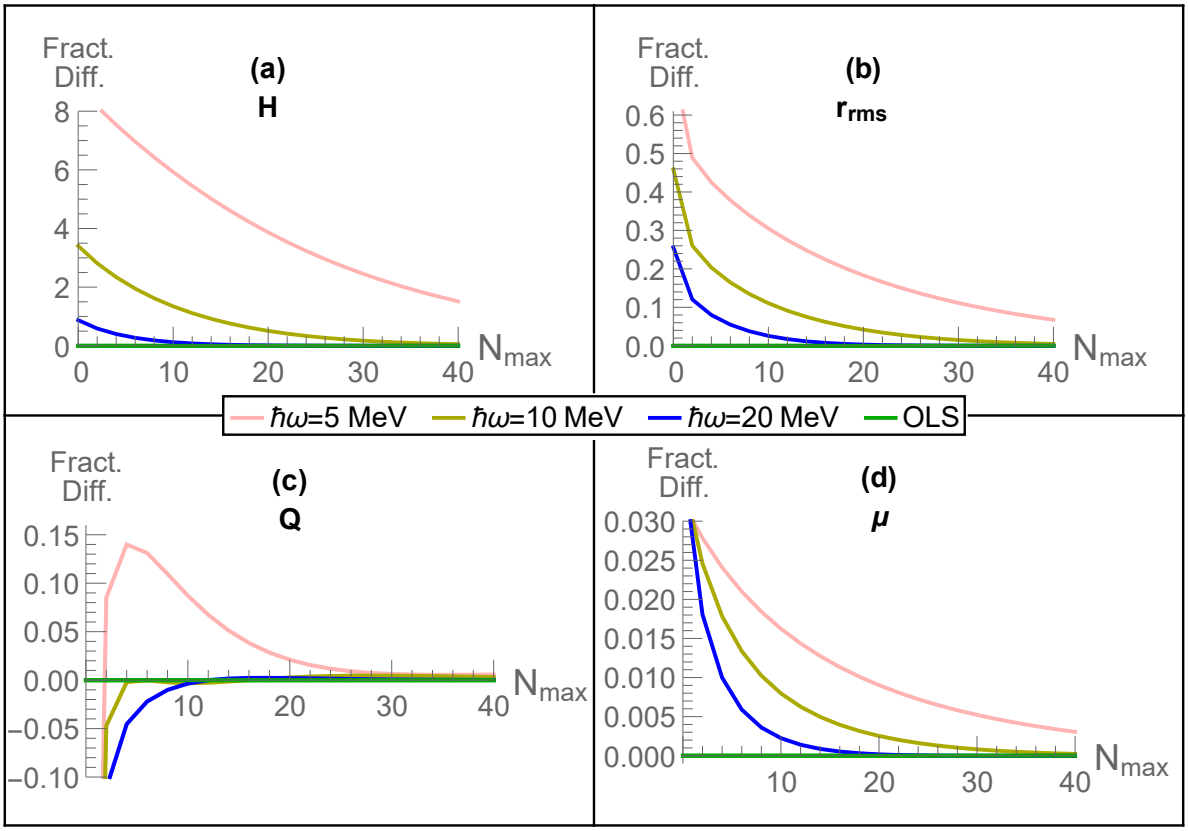

Figure 4.3 Fractional differences between model and exact results as a function of the P–space for selected gs observables of the two-nucleon system in the ${}^3S_1 - {}^3D_1$ channel for three different HO traps. The NN interaction is the LENPIC–N^{2}LO NN interaction with regulator $R = 1.0$ fm. HO energies $\hbar\Omega$ for the bases correspond to the HO energies of the traps. The observables correspond to the eigenenergy (a), the rms point-proton radius (b), the electric quadrupole moment (c) and the magnetic dipole moment (d).

For the initial set of gs observables beyond the gs energy, we again examine the rms point-proton radius $r_{\rm rms}$, quadrupole moment Q and magnetic dipole moment μ. We note that the role of the harmonic confining interaction is significant since the wave functions will therefore have gaussian asymptotic properties which moderate the long-range contributions of these operators. In true nuclear bound state environments, the asymptotic wave functions are exponential and provide significant contributions to the long-range observables.

For both the truncation approach and the OLS approach, we again present the results for the gs expectation value of these operators as a fractional difference from the exact results in Fig. (4.3). The exact results are, again, those obtained in $N_{\rm max} = 400$ calculations and are given in the Appendix for completeness. Note the major differences in the scales of Fig. (4.3). The results of truncation are the largest for the gs energy (see discussion above) and then decreasing in size for $r_{\rm rms}$, Q and μ in that order. The results of truncation are also largest at $\hbar\Omega = 5$ MeV and smallest at $\hbar\Omega = 20$ MeV. Physically, one expects that, as $\hbar\Omega$ increases, the trap will become more important than the NN interaction in the Hamiltonian. With this decreasing role of the NN interaction, results from the truncation approach will trend towards the simpler situation of two nucleons in a simple HO Hamiltonian where they are increasingly representative of the exact results with the same simple Hamiltonian. Indeed, the main impression of the results of the truncation approach with a trap in Fig. (4.3) is the generally smooth trends that contrast the results without a trap presented in Fig. (4.2) – in particular, the sawtoooth behavior seen in Fig. (4.2) is absent from Fig. (4.3). While $r_{\rm rms}$ (panel (b)) and μ (panel (d)) appear to have a monotonic convergence pattern, just like the gs energy, the convergence pattern for Q is slightly more complicated. The Fract. Diff. for Q in the truncation approach at lower HO trap energies exhibits a sign change while it exhibits a tendency towards monotonic behavior at larger trap energies.

As shown previously in Fig. (4.2), we find that, as expected, the results for the gs observables in Fig. (4.3) within the OLS approach agree with the exact gs results over all choices of P–spaces and traps. This agreement is evident through the Fract. Diff. remaining zero (flat green lines) for the

OLS results in all panels. We checked that the Fract. Diff. for the OLS results shown in Fig. (4.3) are zero to at least six significant figures.

4.4.4 Two nucleons in HO trap – weak observables

We now consider the Gamow-Teller (GT) beta decay matrix element for the transition from the gs of the $^1S_0$ nn channel to the gs of the $^3S_1 - ^3D_1$ deuteron channel shown in panels (a) and (b) of for the same traps as above. For panel (a) (and also for panel (c)) we adopt the LENPIC–NLO NN interaction. For panel (b) (and also for panel (d)) we adopt the LENPIC–N^{2}LO NN interaction. The GT operator is the simple spin-isospin form [20]. Our aim is to explore the role of two different, but lower, chiral order interactions with panels (a) and (b) (and also panels (c) and (d)). Future works will employ GT operators from chiral EFT where the emphasis will shift to having all observables, including the eigenvalues, obtained with chiral EFT operators at the same chiral order.

The Fract. Diff. for the GT matrix elements in panels (a) and (b) of Fig. (4.4) displays convergence patterns in the truncation approach similar to the operators in panels (a), (b) and (d) of Fig. (4.3) but on a reduced scale and with the opposite sign. The exact result, whose overall sign is arbitrary and has no physical consequence, is negative with our numerical procedures (see Table 4 in the Appendix). With increasing P–space dimension, the truncation results rise towards the exact results from below producing the Fract. Diff. trends for the GT matrix elements. Thus, in smaller basis spaces, the results of the truncation approach for this gs-to-gs transition would require the application of a scaling, or quenching factor, that is less than unity in order to match the exact results. In order to help make this point more clear, we present plots of the quenching factor (defined as the Exact/Model result) in Fig. (4.5) for the results in Fig. (4.4). We note in panels (a) and (b) of Fig. (4.5) that the quenching factor in truncated calculations of the GT matrix element deviates from unity by, at most, about 6%. The largest deviations from unity and the slowest convergence rates are found with the weakest HO trap energy of $\hbar\Omega = 5$ MeV where the nn and np ground states are spread in coordinate space compared with their distributions in the other HO traps. This

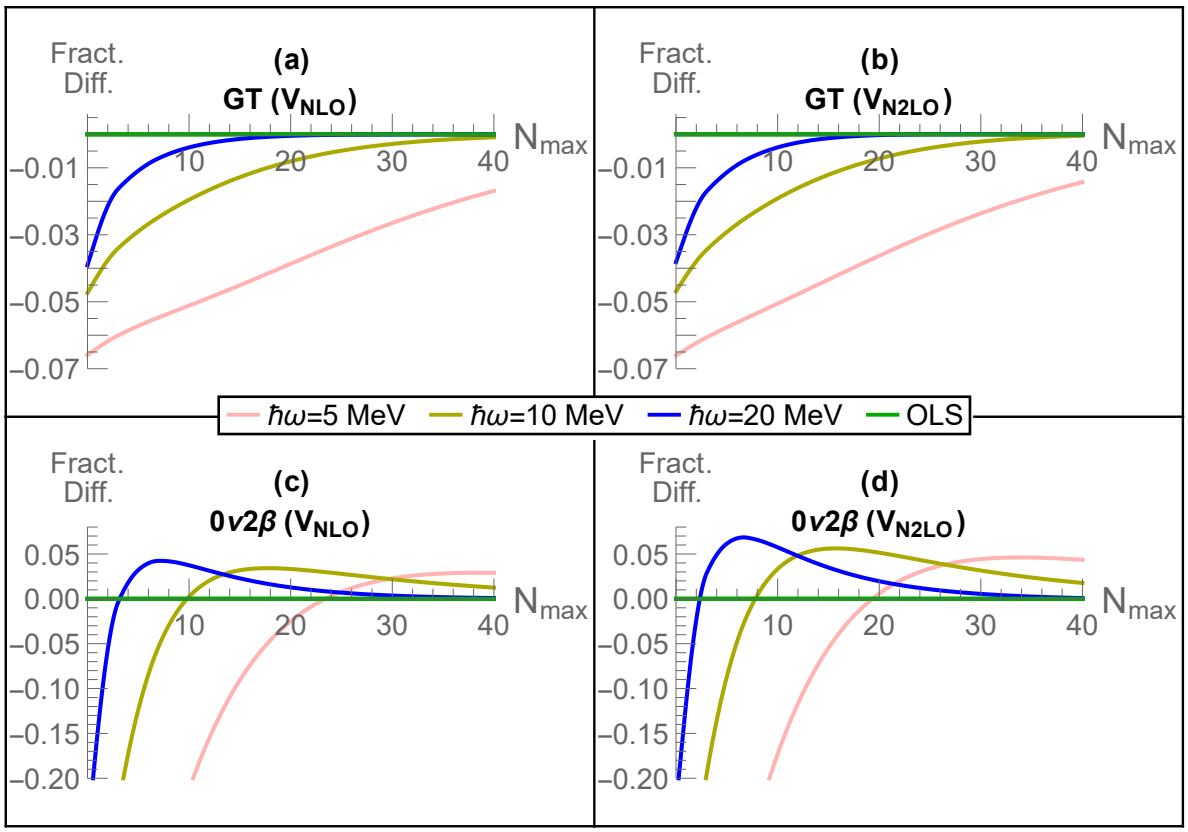

Figure 4.4 Fractional differences between model and exact results as a function of the P–space for selected gs transitions from the lowest state of the ${}^1S_0$ nn system in three different HO traps. Panels (a) and (b) are for the allowed GT-transition to the gs of the ${}^3S_1 - {}^3D_1$ channel. Panels (c) and (d) are for the $0\nu2\beta$-decay to the gs of the ${}^1S_0$ pp system. The NN interaction for cases (a) and (c) are taken to be the LENPIC–NLO potential, while we adopt the LENPIC–N^{2}LO potential for cases (b) and (d). All results shown employ LENPIC NN interactions with coordinate space regulator $R = 1.0$ fm.

systematic decrease of the GT quenching factor from unity with increasing spatial distribution of the two-nucleon system is reminiscent of the approximate phenomenological decrease in the quenching factor for GT matrix elements in valence spaces with increasing atomic number [21]. On the other hand, as expected, the OLS approach again produces the exact GT results for all our choices of the HO trap energies and for all choices of P–space (flat green lines at zero (unity) for panels (a) and (b) of Fig. (4.4) (Fig. (4.5))).

Finally, owing to intense current interest, we investigate the $0\nu2\beta$-decay operator within the same approaches and exhibit the results for three traps in panels (c) (with LENPIC–NLO) and panel (d) (with LENPIC–N^{2}LO) of Fig. (4.4) and Fig. (4.5). We adopt the $0\nu2\beta$-decay operator from chiral EFT of Ref. [22], which is consistent with chiral N^{2}LO. For calculating our exact results, we employ a basis space with $N_{\max} = 200$ which is sufficient for high-accuracy calculations with the LENPIC interaction at N^{2}LO. We elect not to apply the LENPIC semilocal coordinate space regulator to this $0\nu2\beta$-decay operator as this regulator is not gauge invariant.

The $0\nu2\beta$-decay results in panels (c) and (d) of Fig. (4.4) and Fig. (4.5) reveal that convergence patterns of the truncation approach are sensitive to the HO energy of the trap. Furthermore, in contrast with several results seen above, the $0\nu2\beta$-decay Fract. Diff. results of Fig. (4.4) do not appear to approach the exact result with increasing P–space dimension until we reach about $N_{\max} = (10, 20, 40)$ for $\hbar\Omega = (20, 10, 5)$ MeV respectively. At $N_{\max} = 0$, the magnitude of the results from the truncation approach are much smaller than the exact results; with increasing $N_{\max}$ the results from the truncation approach increase but overshoot the exact results by about 5% before converging towards the exact results. That is, at small $N_{\max}$ values, the $0\nu2\beta$-decay results with the truncation approach are significantly suppressed indicating large effects due to evaluating matrix elements of this operator in truncated basis spaces. For more details of this lower region of $N_{\max}$, we turn to panels (c) and (d) of Fig. (4.5).

The quenching factors in the truncated calculations of $0\nu2\beta$-decay in panels (c) and (d) of Fig. (4.5) rise significantly above unity in the low $N_{\max}$ region contrary to what we find for the GT matrix elements. The rise is largest with the weakest trap strength of $\hbar\Omega = 5$ MeV and smallest

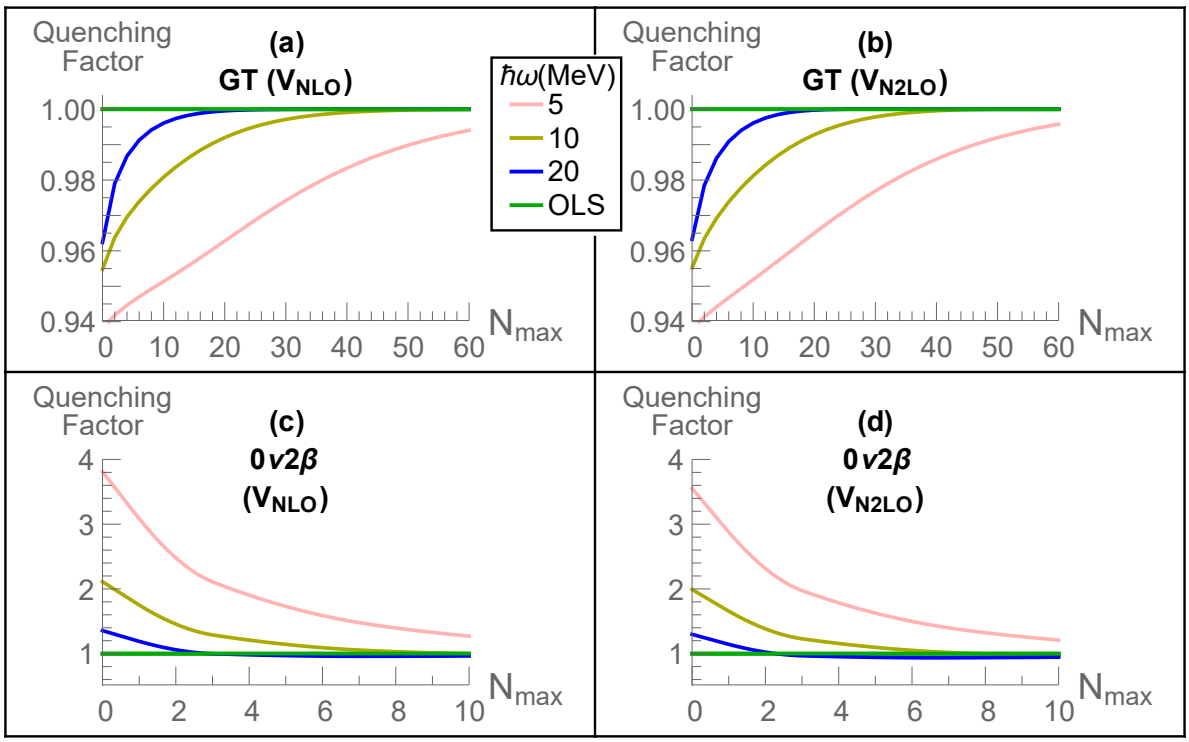

Figure 4.5 Quenching factor defined as Exact/Model for GT-decay and $0\nu2\beta$-decay matrix elements as a function of the P–space for gs transitions from the lowest state of the ${}^1S_0$ nn system in three different HO traps. Panels (a) and (b) are for the allowed GT-transition to the gs of the ${}^3S_1 - {}^3D_1$ channel. Panels (c) and (d) are for the $0\nu2\beta$-decay to the gs of the ${}^1S_0$ pp system. The NN interaction for cases (a) and (c) are taken to be the LENPIC–NLO potential, while we adopt the LENPIC–N^{2}LO potential for cases (b) and (d). All results shown employ LENPIC NN interactions with coordinate space regulator $R = 1.0$ fm. A quenching factor greater than unity signals an enhancement of the model results is required to arrive at the exact results.

with the strongest trap of $\hbar\Omega = 20$ MeV. We interpret these results to indicate that significant contributions from intermediate range components of the $0\nu2\beta$-decay operator are omitted with truncations to the smaller model spaces. Furthermore, these results suggest that truncated calculations of $0\nu2\beta$ transition matrix elements between weakly bound nucleons are likely to require quenching factors greater than unity (i.e., enhancements) in small model spaces. In other words, these substantial excursions above unity may have significant implications for eventual applications in finite nuclei. It is also worth remarking that the OLS transformation is different for the initial and final states of both the GT and $0\nu2\beta$ matrix elements. Therefore, obtaining the exact results for these matrix elements for all P–spaces by the OLS method is another non-trivial test of our numerical procedures.

4.5 Summary and outlook

Our initial application to the deuteron ground state revealed the order-of-magnitude effects of simple P–space basis truncations compared with exact results as a function of the basis HO energy $\hbar\Omega$ for a set of realistic NN interactions. The smallest value studied, $\hbar\Omega = 5$ MeV, produced the largest truncation effects (hence the largest renormalization effects) for these interactions. We also showed that, for a wide range of P–spaces and a selection of NN interactions, the Okubo-Lee-Suzuki approach consistently reproduced the exact results which one anticipates from a theoretical perspective.

Effective Hamiltonians and effective electroweak operators were then calculated for two nucleons in a confining harmonic oscillator trap as a function of the P–space. For this system, matrix elements of all OLS-derived effective operators again agree with exact results in all model spaces and for all traps investigated. We quantify the deviations of the simple truncated space results from the exact results for three different traps as a function of the P–space. We illustrate these effects for the root-mean-square point-proton radius, electric quadrupole moment, magnetic dipole moment, Gamow-Teller transition and neutrinoless double-beta decay operators using NN interactions from chiral Effective Field Theory.

From the results shown in Figs. (4.3,4.4,4.5), we found that the size of error in the matrix element of an observable introduced by a truncated basis space approach depends on the observable, the value of the HO parameter of the trap $\hbar\Omega$, and the severity of the P–space truncation given by $N_{\max}$. Long-range observables, such as the root-mean-square point-proton radius and the electric quadrupole moment exhibited larger errors due to truncation to smaller spaces than the magnetic dipole and GT operators. We also found surprisingly large truncation errors for the double beta decay operator – larger than that of Q, and of the same order as the $r_{\rm rms}$ radius. On the other hand, the GT operator exhibited behaviors similar to the magnetic moment as may be expected.

While these results appear to be reasonable in the qualitative sense and are consistent with previous investigations, the quantitative dependencies shown here may be useful in estimating uncertainties for observables obtained in truncated many-body calculations with realistic NN interactions. In particular, since renormalization effects tend to be larger in cases with weaker traps and smaller basis spaces, applications to heavier nuclei, for both transitions between weakly bound nucleons and to continuum states, will likely be subject to the more significant renormalization effects.

The results presented here also signal the approximate magnitude of the corrections that the OLS renormalization provides for each of our selected observables. These corrections, which can be obtained with OLS renormalization, should be carried forward to the appropriate many-body applications. It will also be important to implement the chiral Effective Field Theory treatment of the electroweak operators that are consistent with the chiral Effective Field Theory of the strong inter-nucleon interactions.

4.6 Acknowledgements

We acknowledge fruitful discussions with Hugh Potter, Evgeny Epelbaum, Hermann Krebs and Jacek Golak. We acknowledge Robert Basili and Weijie Du as project leaders. This work was supported in part by the US Department of Energy (DOE) under Grant Nos. DE-FG02-87ER40371, DE-SC0018223 (SciDAC-4/NUCLEI) and DE-SC0015376 (DOE Topical Collaboration in Nuclear

Theory for Double-Beta Decay and Fundamental Symmetries). PM thanks the Fundação de Amparoà Pesquisa do Estado de São Paulo (FAPESP) for support under grant No 2017/19371-0. Computational resources were provided by the National Energy Research Scientific Computing Center (NERSC), which is supported by the US DOE Office of Science under Contract No. DE-AC02-05CH11231.

4.7 Appendix

We present tables of results that correspond to the $N_{\max} = 400$ case unless otherwise specified, where all results have converged to six or more digits of precision as a function of N_{max}. All results involving the LENPIC interactions in the Hamiltonian correspond to adopting the LENPIC regulator $R = 1.0$ fm. Results are presented at each value of the HO basis parameter $\hbar\Omega$ and for each observable. Differences between the "exact" results in the sixth significant figure at different values of $\hbar\Omega$ in Tables 1 and 2 arise from the transformation of the HO basis representation from an initial representation at $\hbar\Omega = 28$ MeV where 5 significant figures in the gs energy was adopted as the criteria for accuracy in the HO basis transformation. On the other hand, the results shown here to six significant figures are the results reproduced by the OLS transformation to at least this level of accuracy.

Table 4.1 Ground-state eigenvalues (in MeV) for the specified potentials used as the "exact" values in Fig. (4.1).

	$\hbar\Omega$ (MeV)		
Potential	5	10	20
LENPIC–NLO	-2.20607	-2.20609	-2.20609
LENPIC–N^{2}LO	-2.23508	-2.23516	-2.23516
LENPIC–N^{3}LO	-2.22324	-2.22326	-2.22326
Idaho–N^{3}LO	-2.22458	-2.22459	-2.22458

Table 4.2 Ground-state eigenvalues and selected observables used as the "exact" values in Fig. (4.2). The results were obtained with the LENPIC–N^{2}LO interaction with regulator $R = 1.0$ fm. No confining interaction was included.

	$\hbar\Omega$ (MeV)		
gs Observable	5	10	20
H (MeV)	-2.23508	-2.23516	-2.23516
$r_{\rm rms}$ (fm)	1.96440	1.96436	1.96436
Q (e fm^2)	0.269862	0.269874	0.269873
μ (μ_N)	0.856323	0.856323	0.856323

Table 4.3 Ground-state eigenvalues and selected observables used as the "exact" values in Fig. (4.3). The results were obtained with the LENPIC–N^{2}LO interaction with regulator $R = 1.0$ fm. The strength of the confining HO potential is the same as the basis parameter $\hbar\Omega$ that labels each column of results.

	$\hbar\Omega$ (MeV)		
gs Observable	5	10	20
H (MeV)	-0.703487	2.35148	10.7332
$r_{\rm rms}$ (fm)	1.44078	1.20869	0.992923
Q (e fm^2)	0.204165	0.164676	0.122359
μ (μ_N)	0.852184	0.849597	0.84814

Table 4.4 Ground-state transition matrix elements used as the "exact" values in Figs. (4.4,4.5). The strength of the confining HO potential is the same as the basis parameter $\hbar\Omega$ that labels each column of results. The GT transition matrix element values correspond to the $N_{\rm max} = 400$ case, where they have converged to six or more significant digits. The $0\nu2\beta$ transition matrix element values correspond to the $N_{\rm max} = 200$ case, where they have converged to four or more significant digits.

		$\hbar\Omega$ (MeV)		
Decay	LENPIC	5	10	20
GT	NLO	-1.40355	-1.42839	-1.43974
	N^{2}LO	-1.40338	-1.42902	-1.44106
$0\nu2\beta$	NLO	1.59067	0.505287	0.827882
	N^{2}LO	1.48274	0.476412	0.792684

References

[1] Susumu Ôkubo. Diagonalization of Hamiltonian and Tamm-Dancoff Equation. *Progress of Theoretical Physics*, 12(5):603–622, 11 1954. ISSN 0033-068X. doi: 10.1143/PTP.12.603. URL https://doi.org/10.1143/PTP.12.603.

[2] Kenji Suzuki and Shyh Yuan Lee. Convergent Theory for Effective Interaction in Nuclei*). *Progress of Theoretical Physics*, 64(6):2091–2106, 12 1980. ISSN 0033-068X. doi: 10.1143/PTP.64.2091. URL https://doi.org/10.1143/PTP.64.2091.

[3] Kenji Suzuki. Construction of Hermitian Effective Interaction in Nuclei: General Relation between Hermitian and Non-Hermitian Forms. *Progress of Theoretical Physics*, 68(1):246–260, 07 1982. ISSN 0033-068X. doi: 10.1143/PTP.68.246. URL https://doi.org/10.1143/PTP.68.246.

[4] Ionel Stetcu, Bruce R. Barrett, Petr Navràtil, and James P. Vary. Effective operators within the ab initio no-core shell model. *Phys. Rev.*, C71:044325, 2005. doi: 10.1103/PhysRevC.71.044325.

[5] Ionel Stetcu, Bruce R. Barrett, Petr Navràtil, and James P. Vary. Long and short-range correlations in the ab-initio no-core shell model. *Phys. Rev.*, C73:037307, 2006. doi: 10.1103/PhysRevC.73.037307.

[6] A. F. Lisetskiy, M. K. G. Kruse, B. R. Barrett, P. Navràtil, I. Stetcu, and J. P. Vary. Effective operators from exact many-body renormalization. *Phys. Rev.*, C80:024315, 2009. doi: 10.1103/PhysRevC.80.024315.

[7] Bruce R. Barrett, Petr Navràtil, and James P. Vary. Ab initio no core shell model. *Prog. Part. Nucl. Phys.*, 69:131–181, 2013. doi: 10.1016/j.ppnp.2012.10.003.

[8] E. Dikmen, A. F. Lisetski, B. R. Barrett, P. Maris, A. M. Shirokov, and J. P. Vary. Ab initio effective interactions for sd-shell valence nucleons. *Phys. Rev.*, C91(6):064301, 2015. doi: 10.1103/PhysRevC.91.064301.

[9] E. R. Anderson, S. K. Bogner, R. J. Furnstahl, and R. J. Perry. Operator Evolution via the Similarity Renormalization Group I: The Deuteron. *Phys. Rev.*, C82:054001, 2010. doi: 10.1103/PhysRevC.82.054001.

[10] E. Epelbaum, H. Krebs, and U. G. Meißner. Precision nucleon-nucleon potential at fifth order in the chiral expansion. *Phys. Rev. Lett.*, 115(12):122301, 2015. doi: 10.1103/PhysRevLett.115.122301.

[11] E. Epelbaum, H. Krebs, and U. G. Meißner. Improved chiral nucleon-nucleon potential up to next-to-next-to-next-to-leading order. *Eur. Phys. J.*, A51(5):53, 2015. doi: 10.1140/epja/i2015-15053-8.

[12] P. Maris et al. Properties of 4He and 6Li with improved chiral EFT interactions. *EPJ Web Conf.*, 113:04015, 2016. doi: 10.1051/epjconf/201611304015.

[13] S. Binder et al. Few-nucleon systems with state-of-the-art chiral nucleon-nucleon forces. *Phys. Rev.*, C93(4):044002, 2016. doi: 10.1103/PhysRevC.93.044002.

[14] S. Binder et al. Few-nucleon and many-nucleon systems with semilocal coordinate-space regularized chiral nucleon-nucleon forces. *Phys. Rev.*, C98(1):014002, 2018. doi: 10.1103/PhysRevC.98.014002.

[15] D. R. Tilley, C. M. Cheves, J. L. Godwin, G. M. Hale, H. M. Hofmann, J. H. Kelley, C. G. Sheu, and H. R. Weller. Energy levels of light nuclei A=5, A=6, A=7. *Nucl. Phys.*, A708: 3–163, 2002. doi: 10.1016/S0375-9474(02)00597-3.

[16] Ik Jae Shin, Youngman Kim, Pieter Maris, James P. Vary, Christian Forssén, Jimmy Rotureau, and Nicolas Michel. Ab initio no-core solutions for ^{6}Li. *J. Phys.*, G44(7):075103, 2017. doi: 10.1088/1361-6471/aa6cb7.

[17] C. P. Viazminsky and James P. Vary. On mathematical structure of effective observables. *Journal of Mathematical Physics*, 42(5):2055–2064, 2001. doi: 10.1063/1.1286034. URL https://aip.scitation.org/doi/abs/10.1063/1.1286034.

[18] P. Navràtil, J. P. Vary, and B. R. Barrett. Properties of C-12 in the ab initio nuclear shell model. *Phys. Rev. Lett.*, 84:5728–5731, 2000. doi: 10.1103/PhysRevLett.84.5728.

[19] D. R. Entem and R. Machleidt. Accurate charge dependent nucleon nucleon potential at fourth order of chiral perturbation theory. *Phys. Rev.*, C68:041001, 2003. doi: 10.1103/PhysRevC.68.041001.

[20] A. Bohr and B. Mottelson. *Nuclear Structure*, volume 1. World Scientific, Singapore, 1998.

[21] G. Martínez-Pinedo, A. Poves, E. Caurier, and A. P. Zuker. Effective g_A in the pf shell. *Phys. Rev.*, C53(6):R2602, 1996. doi: 10.1103/PhysRevC.53.R2602.

[22] Gary Prezeau, M. Ramsey-Musolf, and Petr Vogel. Neutrinoless double beta decay and effective field theory. *Phys. Rev.*, D68:034016, 2003. doi: 10.1103/PhysRevD.68.034016.

CHAPTER 5. BENCHMARK NEUTRINOLESS DOUBLE-BETA DECAY MATRIX ELEMENTS IN A LIGHT NUCLEUS

Modified from a manuscript submitted to *Physical Review C*

R.A.M. Basili,[1] J.M. Yao,[2,3] J. Engel,[2] H. Hergert,[3]

M. Lockner,[1] P. Maris,[1] J.P. Vary[1]

[1]Department of Physics, Iowa State University, Ames, IA 50010, USA

[2]Department of Physics, University of North Carolina, Chapel Hill, NC 27514, USA

[3]FRIB/NSCL and Department of Physics and Astronomy, Michigan State University, East Lansing, MI 48824, USA

5.1 Abstract

We compute nuclear matrix elements of neutrinoless double-beta decay mediated by light Majorana-neutrino exchange in the $A = 6$ system. The goal is to benchmark two many-body approaches, the No-Core Shell Model and the Multi-Reference In-Medium Similarity Renormalization Group. We use the SRG-evolved chiral N3LO-EM500 potential for the nuclear interaction, and make the approximation that isospin is conserved. We compare the results of the two approaches as a function of the cutoff on the many-body basis space. Although differences are seen in the predicted nuclear radii, the ground-state energies and neutrinoless double-beta decay matrix elements produced by the two approaches show significant agreement. We discuss the implications for calculations in heavier nuclei.

5.2 Introduction

Since the discovery of the lepton flavor violation in neutrino oscillations [1–3], identifying whether the neutrino is a Majorana fermion (i.e. its own antiparticle) has become a priority in nuclear

and particle physics. However, because neutrinos are charge neutral and nearly massless, they are notoriously difficult to detect, and their properties remain only partly understood. Major theoretical and experimental collaborative efforts are already underway to study neutrino properties [4–19]. Answering whether neutrinos are indeed Majorana particles would not only shed light on the mechanism behind neutrino mass generation, but would also provide insight on leptogenesis and the universe's apparent matter-antimatter asymmetry.

Neutrinoless double-beta decay ($0\nu\beta\beta$-decay) is a hypothetical lepton-number-violating (LNV) nuclear transition where two neutrons decay to two protons and two electrons but no anti-neutrinos (or the reverse with leptons exchanged with their antiparticles). Observing $0\nu\beta\beta$-decay would confirm the existence of a LNV process, and is commonly viewed as the best means of learning whether neutrinos are Majorana particles. Experiments designed to detect $0\nu\beta\beta$-decay in ton-scale volumes of ^{76}Ge, ^{136}Xe, and other materials have already put impressive limits on the $0\nu\beta\beta$-decay half-life [6, 7, 9], and these limits will only become more accurate as additional data is collected. For a more complete description of current and past efforts as well as some of the underlying theory, see Refs. [20–24] and references therein.

While of enormous significance in itself, the experimental detection or non-detection of $0\nu\beta\beta$-decay will be insufficient to pin down or put limits on extra-Standard-Model parameters such as the average neutrino mass. Because the decay rate depends on the $0\nu\beta\beta$-decay nuclear matrix elements (NMEs), interpreting the experimental results requires the accurate calculation of those NMEs. However, at present the calculated NMEs in the heavy nuclei of interest differ by a factor of two to three [22]. In addition, calculated NMEs for β-decay are usually smaller than experimental values, and the reasons for these differences are only now being understood in a quantitative way [25]. To shed light on these differences, it is helpful to examine weak processes in light nuclei, where calculations are better controlled than in the heavy nuclei we must eventually grapple with. Thus, while not experimentally viable for $0\nu\beta\beta$-decay, light nuclei are a practical option for benchmarking.

The purpose of this study is to calculate the NMEs (for $0\nu\beta\beta$-decays mediated by light Majorana-neutrino exchange) in the $A = 6$ system. Benchmarking different many-body methods and identify-

ing important features that affect the NMEs in these light nuclei will both test the approaches that we will apply in heavy nuclei and help us anticipate issues that may arise there. Assessing the convergence behavior of the decay NMEs with increasing model-space size is of particular importance, as it will help quantify uncertainties in heavier nuclei where more severe basis truncation is computationally required. Thus, we consider the ground-state-to-ground-state $0\nu\beta\beta$-decay of ^{6}He $\rightarrow$ ^{6}Be, which, while kinematically disallowed, involves the same decay operator that determines the allowed decay rates in heavy nuclei.

We employ two *ab initio* many-body approaches: the No-Core Shell Model (NCSM) and the Multi-Reference In-Medium Similarity Renormalization Group (MR-IMSRG). The NCSM is a large-scale diagonalization method that yields exact results in the limit of an infinitely large configuration space. On the other hand, the MR-IMSRG (a variation of the IMSRG in which the method's reference state contains explicitly built-in correlations) yields approximate solutions to the many-body Schrödinger equation within a systematically improvable truncation scheme. That is, where the NCSM includes all many-body correlations up to the given basis cutoff by construction, the MR-IMSRG only includes many-body correlations up to a cutoff in the many-body expansion. In exchange, the computational effort of the MR-IMSRG scales much more favorably with particle number and configuration space size, which makes it capable of modeling both light and heavy nuclei. While both methods treat all nucleons as active, they can also be used to generate effective interactions and operators for traditional Shell-model calculations in heavier nuclei [26–32].

For both the MR-IMSRG and NCSM calculations performed in this work, we assume good isospin symmetry to facilitate the comparison of their results, though it should be noted that we could drop this assumption at the cost of introducing more complex methods [33, 34]. For both approaches we adopt the next-to-next-to-next-to-leading chiral order (N3LO) Entem-Machleidt two-body potential with regulator cutoff $\Lambda = 500$ MeV (referred to as 'N3LO-EM500') [35, 36], to model the nucleon-nucleon (NN) interaction. The potential is expressed in the harmonic oscillator (HO) basis with energy scale $\hbar\Omega = 20$ MeV, and softened by SRG evolution to the scale of $\lambda = 2.0$ fm^{-1} (with the relative kinetic energy, T_{rel}, as the generator [37]) prior to many-body calculations.

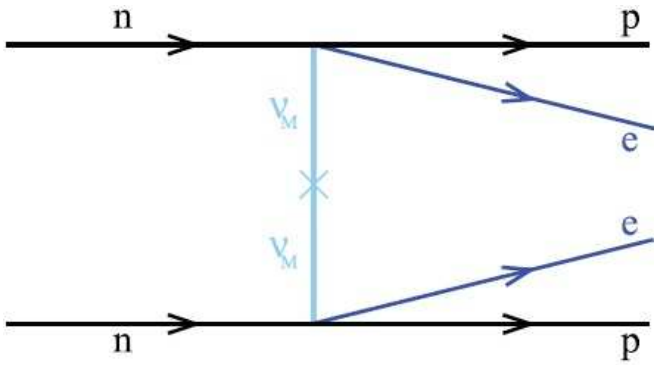

Figure 5.1 Feynman diagram (modified from Ref. [22]) for $0\nu\beta\beta$-decay mediated by light-neutrino exchange. Two neutrons (n) decay into two protons (p), emitting two electrons (e^-). No neutrinos are emitted, implying that they are Majorana particles (ν_M).

Our examination of the $A = 6$ system with the NCSM is similar to the studies in Refs. [38, 39], but differs from both in: the NN-interaction used, the extrapolations employed, our focus on $0\nu\beta\beta$-decay, and our comparison with the MR-IMSRG approach. Our study also offers a point of comparison to the computation of $0\nu\beta\beta$-decay NMEs arising from an array of LNV mechanisms in light nuclei by using *ab initio* Variational Monte-Carlo (VMC) techniques [40], though our study is distinguished by our use of a different NN-interaction and our focus solely on $0\nu\beta\beta$-decay mediated by light Majorana-neutrino exchange.

The rest of this paper is structured as follows: Section 5.3 briefly outlines the derivation of the $0\nu\beta\beta$-decay operator as defined in Refs. [22, 41, 42]. We provide a brief review of the NCSM in 5.4.1, and the MR-IMSRG in 5.4.2. Section 5.5 compares the ground-state energy and square radius (in 5.5.1), and analyzes the contributions to the total $0\nu\beta\beta$-decay NME (in 5.5.2). Finally, Section 5.6 reviews our findings and concludes the discussion. Additional details regarding our extrapolation methods and tables of calculated values are provided in Appendix 5.8.

5.3 $0\nu\beta\beta$ with light majorana-neutrinos

We consider $0\nu\beta\beta$-decay caused by the exchange of the three light Majorana neutrinos and the Standard-Model weak interaction as depicted in Fig. (5.1); all contributions from other LNV processes are neglected.

Drawing on Refs. [22, 41] and the approximations employed there, we write the $0\nu\beta\beta$-decay rate as

$$\left[T^{0\nu}_{1/2}\right]^{-1} = G_{0\nu}\left(Q,Z\right)\left|M_{0\nu}\right|^2\left|\sum_k m_k U^2_{ek}\right|^2 , \tag{5.1}$$

where Q is the difference between initial (i) and final (f) state energies, (i.e. $Q \equiv E_i - E_f$), Z is the proton number of the final nucleus, m_k is the Majorana mass eigenvalue, and U_{ek} is an element of the neutrino mixing matrix that connects neutrino flavor with mass eigenstate k. $G_{0\nu}\left(Q,Z\right)$ comes from the phase-space integral which has been evaluated with improved precision in Refs. [43, 44].

In this study, we focus on the ^{6}He $\rightarrow$ ^{6}Be ground-state-to-ground-state NME, $M_{0\nu}$ [42, 45, 46], obtained from the $0\nu\beta\beta$-decay many-body operator, $O_{0\nu}$, as

$$M_{0\nu} = \langle {}^6\mathrm{Be}|O_{0\nu}|{}^6\mathrm{He}\rangle. \tag{5.2}$$

Our notation follows that of Ref. [47] unless specified otherwise.

5.3.1 The $0\nu\beta\beta$-decay matrix elements

The many-body operator $O_{0\nu}$ is conventionally divided into three contributions, labeled Fermi, Gamow-Teller (GT), and tensor. We use the symbol O to generically denote any one of these contribution's corresponding two-body operator, which may always be written in second-quantized form as

$$O = \frac{1}{4}\sum_{\alpha\beta\gamma\delta}\langle\alpha\beta|O|\gamma\delta\rangle a^\dagger_\alpha a^\dagger_\beta a_\delta a_\gamma \tag{5.3}$$

where $a^\dagger$ and a create and annihilate nucleons, respectively, in single-particle states. A given single-particle state α is defined by the quantum numbers n_α, l_α, s_α, j_α, t_α, $m_{j\alpha}$, and $m_{t\alpha}$, which correspond to the radial, angular momentum, spin, total angular momentum, isospin, angular momentum projection, and isospin projection, respectively. Greek indices $\alpha, \beta, \gamma, \delta$ are used to denote single-particle states, while the corresponding Roman indices a, b, c, d refer to the reduced set of quantum numbers, such that $a^\dagger_\alpha \equiv a^\dagger_{a,m_{j\alpha},m_{t\alpha}}$. We define spherical tensor/isotensor versions of the annihilation operators as

$$\hat{a}_\delta \equiv (-1)^{j_\delta + m_{j\delta} + \frac{1}{2} + m_{t\delta}} \, a_{d,-m_{j\delta},-m_{t\delta}} \, , \tag{5.4}$$

such that

$$a_\delta a_\gamma = (-1)^{j_\gamma + j_\delta + m_{j\gamma} + m_{j\delta} + 1} \, \hat{a}_{c,-m_{j\gamma},-m_{t\gamma}} \hat{a}_{d,-m_{j\delta},-m_{t\delta}} \, . \tag{5.5}$$

For the ground-state-to-ground-state transition of ^{6}He $\rightarrow^6$ Be, we may narrow our scope to components of the two-body operators that contribute to $0^+ \rightarrow 0^+$ NMEs. Expanding Eq. (5.3) into doubly-reduced tensorial components in the JT-coupled two-body isospin representation yields for this transition

$$\begin{aligned} O^{0,2}_{0,-2} = -\frac{1}{4\sqrt{3}} \sum_{abcd} \sum_{J} & \left(\mathcal{N}_{ab}\left(J,1\right)\mathcal{N}_{cd}\left(J,1\right)\right)^{-1} \\ & \cdot \left(ab;J\,1|||O^{0,2}|||cd;J\,1\right) \\ & \cdot \left[\left[a^\dagger_a a^\dagger_b\right]^{J,1}\left[\hat{a}_c \hat{a}_d\right]^{J,1}\right]^{0,2}_{0,-2} \, , \end{aligned} \tag{5.6}$$

where brackets denote tensor products with tensor, isotensor couplings in superscripts and their corresponding projections in subscripts, $\mathcal{N}_{ij}(J,T) \equiv \sqrt{1-\delta_{ij}(-1)^{J+T}}/(1+\delta_{ij})$ is an antisymmetrization factor, and the triple lines '$|||$' denote doubly-reduced two-body matrix elements (TBMEs). In Eq. (5.6) we implicitly include only two-body states that satisfy the Pauli exclusion principle in the sum over nucleon states (or, effectively, we only consider values of i, j, J, and T such that $\mathcal{N}_{ij}(J,T) \neq 0$).

We express the total NME ($M_{0\nu}$) as the sum of the Fermi ($M^F_{0\nu}$), GT ($M^{GT}_{0\nu}$), and tensor ($M^T_{0\nu}$) contributions

$$M_{0\nu} = M^F_{0\nu} + M^{GT}_{0\nu} + M^T_{0\nu}\,. \tag{5.7}$$

These three NME contributions are developed for the many-body initial and final nuclear states from the doubly-reduced TBMEs of the three corresponding two-body operators. We evaluate the NMEs by summing over the two-body contribution from each unique pair of the system's nucleons. We calculate the TBMEs with the two-body operators

$$\begin{aligned}
O^F_{0\nu}(r) &= \frac{4R}{\pi g_A^2}\int_0^\infty |\mathbf{q}|d|\mathbf{q}|\frac{j_0(|\mathbf{q}|r)h_F(|\mathbf{q}|)}{|\mathbf{q}|+\bar{E}-(E_i+E_f)/2}\tau_1^+\tau_2^+\,,\\
O^{GT}_{0\nu}(r) &= \frac{4R}{\pi g_A^2}\int_0^\infty |\mathbf{q}|d|\mathbf{q}|\frac{j_0(|\mathbf{q}|r)h_{GT}(|\mathbf{q}|)\boldsymbol{\sigma}_1\cdot\boldsymbol{\sigma}_2}{|\mathbf{q}|+\bar{E}-(E_i+E_f)/2}\tau_1^+\tau_2^+\,,\\
O^T_{0\nu}(r) &= \frac{4R}{\pi g_A^2}\int_0^\infty |\mathbf{q}|d|\mathbf{q}|\frac{j_2(|\mathbf{q}|r)h_T(|\mathbf{q}|)\boldsymbol{S}_{12}}{|\mathbf{q}|+\bar{E}-(E_i+E_f)/2}\tau_1^+\tau_2^+\,,
\end{aligned} \tag{5.8}$$

where $\boldsymbol{q}$ is the momentum transfer, $r = |\boldsymbol{r}_1 - \boldsymbol{r}_2|$ is the magnitude of the inter-nucleon position vector, and $\hat{\boldsymbol{r}}$ is the corresponding unit vector. Additionally, $\boldsymbol{r}_{1\backslash 2}$, $\boldsymbol{\sigma}_{1\backslash 2}$, and $\tau^+_{1\backslash 2}$ respectively denote the labeled nucleon's position operator, spin operator, and isospin raising operator (transforming neutrons to protons), while $\boldsymbol{S}_{12} = 3\boldsymbol{\sigma}_1\cdot\hat{\boldsymbol{r}}\boldsymbol{\sigma}_2\cdot\hat{\boldsymbol{r}} - \boldsymbol{\sigma}_1\cdot\boldsymbol{\sigma}_2$ is the tensor operator. The NMEs contain r-dependence through the spherical Bessel functions j_0 and j_2 in Eq. (5.8), and, for several heavy parent nuclei, have been shown to vanish at small distances r, fall off like $1/r$ at large distance, and have a typical range of a few femtometers (fm) [48]. Hence, we expect good convergence with the basis space for these operators in our calculations.

The neutrino potentials, h, are defined in momentum space as

$$\begin{aligned}
h_F(|\boldsymbol{q}|) &\equiv -g_V^2(\boldsymbol{q}^2)\,,\\
h_{GT}(|\boldsymbol{q}|) &\equiv g_A^2(\boldsymbol{q}^2) - \frac{g_A(\boldsymbol{q}^2)g_P(\boldsymbol{q}^2)\boldsymbol{q}^2}{3m_N} + \frac{g_P^2(\boldsymbol{q}^2)\boldsymbol{q}^4}{12m_N^2} + \frac{g_M^2(\boldsymbol{q}^2)\boldsymbol{q}^2}{6m_N^2}\,,\\
h_T(|\boldsymbol{q}|) &\equiv \frac{g_A(\boldsymbol{q}^2)g_P(\boldsymbol{q}^2)\boldsymbol{q}^2}{3m_N} - \frac{g_P^2(\boldsymbol{q}^2)\boldsymbol{q}^4}{12m_N^2} + \frac{g_M^2(\boldsymbol{q}^2)\boldsymbol{q}^2}{12m_N^2}\,,
\end{aligned} \tag{5.9}$$

where $g_M(q^2) = (1+\kappa_1)\,g_V(q^2) \simeq 4.706 g_V(q^2)$ (with the anomalous nucleon isovector magnetic moment $\kappa_1 = 3.706$), and the Goldberger–Treiman relation $g_P(q^2) = 2m_N g_A(q^2)/(\boldsymbol{q}^2 + m_\pi^2)$

(with nucleon mass m_N and pion mass m_π) connects the pseudoscalar and axial terms [49, 22]. The conservation of the vector current implies that $g_V \equiv g_V\left(q^2\right)\big|_0 = 1$, while the value $g_A \equiv g_A\left(q^2\right)\big|_0 \simeq 1.27$ may be extracted from neutron β-decay measurements. Their momentum transfer dependence is $g_V\left(q^2\right) = g_V\left(1 + q^2/\Lambda_V^2\right)^{-2}$ and $g_A\left(q^2\right) = g_A\left(1 + q^2/\Lambda_A^2\right)^{-2}$ where $\Lambda_V = 850$ MeV and $\Lambda_A = 1040$ MeV are the vector and axial masses, respectively. The nuclear radius $R = 1.2A^{\frac{1}{3}} \approx 2.2$ fm is inserted by convention to make the matrix elements dimensionless, with a compensating factor absorbed into $G_{0\nu}$ in Eq. (5.1). Finally, $\bar{E}$ is an estimate of the average intermediate-state energy, the choice of which has been shown to have only a mild influence on the decay amplitude [41]. We employ the value $\bar{E} - (E_i + E_f)/2 \equiv 5\,\text{MeV}$ throughout this work.

In other prescriptions, the operators defined by Eq. (5.8) are sometimes multiplied by an additional radial function, $f(r)$, designed to take into account short-range correlations that are omitted by Hilbert-space truncations performed in the many-body calculations [50–54]. In this work, we assume all relevant nucleon-nucleon correlations are embedded in the many-body wavefunctions generated in our NCSM and MR-IMSRG model spaces and employ no additional radial function. We numerically integrate the inner products of the operators in Eq. (5.8) using relative HO states to obtain reduced matrix elements in the relative basis. These elements are then converted to M-scheme TBMEs via a Moshinsky transformation [55, 56] before being employed in many-body calculations.

5.3.2 $0\nu\beta\beta$-decay in ^{6}He with isospin symmetry

When considering isovector operators, a common challenge shared by many *ab initio* nuclear approaches (particularly those relying on finite matrix methods) arises when the initial and final nuclei are not the same, as the many-body spaces for the two will generally differ. In NCSM calculations, this problem usually requires the many-body eigenstate wavefunctions of the two systems to be calculated independently. In the MR-IMSRG, two different unitary transformation operators must be constructed, one for the initial nucleus and one for the final nucleus.

While solutions for overcoming this challenge have been developed for the NCSM and have been implemented for the MR-IMSRG [34], a careful choice of transition can circumvent the issue when isospin conservation is a good approximation. Thus, we assume that isospin symmetry is obeyed in the mirror nuclei ^{6}He and ^{6}Be.

The ground states of ^{6}Be and ^{6}He are characterized by total angular momentum $\mathcal{J} = 0$ and isospin $\mathcal{T} = 1$, with projections $\mathcal{T}_z = -1, +1$, respectively. If isospin symmetry is obeyed, the two-body density of Eq. (5.6) may be rewritten in terms of the ^{6}He two-body density alone as

$$\begin{aligned}&\langle {}^6\mathrm{Be}| \left[\left[a_a^\dagger a_b^\dagger\right]^{J,1} [\hat{a}_c \hat{a}_d]^{J,1}\right]^{0,2}_{0,-2} |{}^6\mathrm{He}\rangle \\ &= \sqrt{6}\langle {}^6\mathrm{He}| \left[\left[a_a^\dagger a_b^\dagger\right]^{J,1} [\hat{a}_c \hat{a}_d]^{J,1}\right]^{0,2}_{0,0} |{}^6\mathrm{He}\rangle. \end{aligned} \tag{5.10}$$

5.4 Benchmarked methods

Both the NCSM and MR-IMSRG can provide accurate results when applied in light nuclei. The MR-IMSRG has the advantage that, with suitable approximations, it can be applied in heavier systems [26, 29, 30]. For the NCSM one may envision applications in heavier systems by merging it with renormalization approaches or by introducing an inert core and deriving effective interactions for valence-space Shell model calculations (see e.g., Refs. [27, 31, 28, 32]). The approximations involved in these envisioned approaches to heavier nuclei will also require benchmarking.

Both methods consider the A-body nuclear Hamiltonian, H, consisting of a relative kinetic-energy term and interaction terms, i.e.

$$H = \frac{1}{2Am_N}\sum_{i<j}^{A} (p_i - p_j)^2 + V_{NN} + V_{NNN} + ... \tag{5.11}$$

where m_N is the average nucleon mass, V_{NN} is the NN-interaction, and p_i denotes the momentum of nucleon i. We follow the convention for two-body operators where summations over nucleon pairs are performed under the ordering given by $i < j$ to avoid counting the same pair twice. The term V_{NNN} denotes three-body interactions, also called 3-nucleon forces (3NFs), which may be followed

by higher-body interactions. Although studies have demonstrated that 3NFs can have a significant impact on calculated nuclear observables [56], their inclusion would greatly increase computational cost and is thus deferred to future efforts. We therefore consider here only the NN-interactions from N3LO-EM500 [35, 36], which is charge-dependent.

5.4.1 No-Core Shell Model

The NCSM [56] is a configuration-interaction (CI) approach in which the many-body basis states, $|\Phi\rangle$, are expressed as Slater determinants of single-particle states occupied by the system's nucleons, or

$$|\Phi\rangle = \mathcal{A}\left[\prod_i |\phi_{\alpha_i}\rangle\right], \tag{5.12}$$

where $|\phi_{\alpha_i}\rangle$ denotes a single-particle state with quantum numbers α_i occupied by nucleon i, and $\mathcal{A}$ is an antisymmetrization operator that carries both the sign permutations of the determinant as well as an overall normalization factor. Our NCSM approach features separate Slater determinants for the neutrons and protons, and the resulting many-body basis is specific to the nucleus under consideration. For a given application, we form total Slater determinants of fixed parity and fixed total angular momentum projection M_J.

The infinite HO basis (with energy scale fixed by the usual parameter $\hbar\Omega$) is the conventional choice of single-particle basis and is used in this work. Additional details on the HO basis functions may be found in Ref. [56].

The nuclear many-body wavefunctions, $\Psi(r_1, ..., r_A)$, satisfy the A-body Schrödinger equation and are obtained by solving the Hamiltonian matrix eigenvalue problem

$$H|\Psi\rangle = E|\Psi\rangle \tag{5.13}$$

where E is the eigenenergy of nuclear state $|\Psi\rangle$. Beginning with the kinetic-energy and interaction TBMEs in the HO basis, one constructs the A-body Hamiltonian matrix elements in the many-body basis as $\langle\Phi_\mu|H_A|\Phi_\nu\rangle$, where the indices μ and ν label the many-body basis states. The many-body

eigenstates are then linear combinations of many-body basis states:

$$|\Psi\rangle = \sum_{\mu}^{\infty} c_\mu |\Phi_\mu\rangle \tag{5.14}$$

where c_μ are the normalized coefficients of the many-body basis states $|\Phi_\mu\rangle$. For practical calculations, the infinite many-body basis requires truncation, which one controls by using a basis cutoff parameter. For NCSM calculations performed in this study, we employ the cutoff parameter $N_{\max}$, which denotes the maximum number of HO excitation quanta allowed in the many-body basis above the minimum number required by the Pauli principle [56].

Solving Eq. (5.13) with the resulting finite many-body Hamiltonian then becomes a large (but generally sparse) matrix eigenvalue problem. We calculate the solution with the hybrid OpenMP/MPI CI code Many Fermion Dynamics for nucleons (MFDn). The code is optimized for solving the large sparse matrix eigenvalue problem by using a Lanczos-like algorithm to determine the desired lowest-lying energy eigenvalues and corresponding eigenvectors. The eigenvectors are then used with other operator matrix elements to calculate that operator's expectation values during post-processing. For more details on MFDn, see Refs. [57–59].

By solving the system in a sequence of increasingly large bases, one can extrapolate to the result when using the complete basis (i.e. where the matrix dimension of H goes to infinity and the calculation becomes exact). Any other observable can also, in principle, be extrapolated to this limit, and such extrapolations are a distinguishing feature of No-Core Full-Configuration (NCFC) studies [60].

5.4.2 Multi-Reference In-Medium Similarity Renormalization Group

Here we provide a brief overview of the MR-IMSRG; a more complete description may be found in Refs. [61–63]. For an initial Hamiltonian H, the flow equation

$$\frac{dH(s)}{ds} = [\eta(s), H(s)]\,, \tag{5.15}$$

reflects a unitary transformation of the Hamiltonian. Here η is called the generator of scale transformations and s is the flow parameter, defined such that $H(s)\mid_{s=0}$ is just H. The ground-state energy is simply given by the expectation value of the evolved Hamiltonian $H(s)$ in the reference state. Instead of solving the set of differential equations for $H(s)$ in Eq. (5.7), one can solve a similar flow equation for the unitary transformation operator $U(s)$,

$$\frac{dU\left(s\right)}{ds}=\eta\left(s\right)U\left(s\right)\ , \tag{5.16}$$

whose solution can formally be written in terms of the $\mathcal{S}$-ordered exponential

$$U\left(s\right)=\mathcal{S}\exp\int_{0}^{s}ds'\eta\left(s'\right)\ , \tag{5.17}$$

which is short-hand for the Dyson series expansion of $U(s)$. As shown first by Magnus, it is possible to rewrite the unitary transformation operator as $U(s)\equiv e^{\Omega(s)}$, a step that transforms the equation for $U(s)$ into one for Ω [64]:

$$\frac{d\Omega\left(s\right)}{ds}=\sum_{n=0}^{\infty}\frac{B_{n}}{n!}\left[\Omega\left(s\right),\eta\left(s\right)\right]^{(n)}\ . \tag{5.18}$$

The nested commutators in this equation are given by

$$\left[\Omega\left(s\right),\eta\left(s\right)\right]^{(0)}=\eta\left(s\right)\ , \tag{5.19a}$$

$$\left[\Omega\left(s\right),\eta\left(s\right)\right]^{(n)}=\left[\Omega\left(s\right),\left[\Omega\left(s\right),\eta\left(s\right)\right]^{(n-1)}\right]\ , \tag{5.19b}$$

and $B_{n=0,1,2,\cdots}$ are the Bernoulli numbers $\{1,-1/2,1/6,\cdots\}$.

The expectation value of any operator O is then given by $\langle\Phi|O\left(s\right)|\Phi\rangle=\langle\Phi|e^{\Omega(s)}O^{-\Omega(s)}|\Phi\rangle$, and can be evaluated with the Baker-Campbell-Hausdorff formula:

$$e^{\Omega(s)}Oe^{-\Omega(s)}=\sum_{n=0}^{\infty}\frac{1}{n!}\left[\Omega\left(s\right),O\right]^{(n)}\ . \tag{5.20}$$

In the MR-IMSRG calculations performed here, we express all operators in normal-ordered form with respect to a reference state $|\Phi\rangle$ in order to control the proliferation of induced terms. We keep up to normal-ordered two-body operators throughout the calculation, in accordance with the MR-IMSRG(2) truncation described in Ref. [63]. We use particle-number-projected HFB quasiparticle vacua as reference states, and adopt the Brillouin generator [62]. We numerically solve the flow equation for values of s large enough so that the solutions are very close to their asymptotic limits. The underlying Hamiltonian that defines both the projected HFB reference state and the starting point for the flow equation is determined by using the same TBMEs in the single-particle HO basis that are used in our NCSM calculations. However, unlike the NCSM, the MR-IMSRG is formulated in the natural orbital basis of the reference state. Since the reference state results from a projected HFB calculation in a HO basis, the MR-IMSRG effectively explores a configuration space controlled by the cutoff parameter $e_{\max}$, which denotes the maximum number of energy quanta that the HO components of any natural orbital can have. In effect, for a given cutoff $e_{\max}$, the MR-IMSRG many-body basis will include single-particle excitations up to $e_{\max}$ (i.e. one-particle-one-hole, or 1p1h), two-particle excitations (i.e. 1p1h+1p1h or 2p2h) up to $2e_{\max}$, uncorrelated three-body excitations (i.e. 1p1h + 1p1h + 1p1h or 1p1h + 2p2h) up to $3e_{\max}$, and so on.

5.5 Results and discussion

Here we discuss the results of the NCSM and MR-IMSRG calculations. We provide graphical representations of the results, as functions of the basis cutoff parameters, to analyze the convergence of the operators at the chosen basis scale of $\hbar\Omega = 20$ MeV. Throughout, we use solid dots to represent NCSM results and open boxes to represent MR-IMSRG results. Similarly, we use solid lines to denote extrapolations of the NCSM results and dashed lines to denote extrapolations of the MR-IMSRG results.

In order to compare the convergence behavior of results from the NCSM and MR-IMSRG, the differences in their truncation schemes must be considered. We recall that the NCSM's cutoff parameter $N_{\max}$ denotes the total number of allowed *excitation* quanta in the system, and $e_{\max}$ denotes

the maximum number of allowed energy quanta possessed by any single nucleon. Since in ^{6}He at a given $N_{\max}$ the highest number of quanta possessed by any single-particle state will be $N_{\max}+1$, we equate the two cutoffs with the assignment $e_{\max} \equiv N_{\max}+1$ for our comparison. While this assignment is not exact, it ensures that for a given pair of matched cutoffs, identical single-particle bases (and by consolation TBMEs) are used by both truncation schemes. Moreover, our use of this assignment to compare the results does not preclude their examination from other perspectives. Instead, we merely offer this assignment as a reasonable means to present our comparison of the results and their convergence.

We extrapolate our results to obtain predictions of observables at the continuum limit and to better examine their convergence behavior; the functional forms and other details regarding these extrapolations are provided in Appendix 5.8. We extrapolate our results for energy and square radii with formulae (Eq. (5.22) and Eq. (5.23), respectively) inspired by those provided in Refs. [65, 60]. Meanwhile, as is the case for many nonscalar operator observables (with the exception of significant investigations on extrapolating E2 observables [66]), precision extrapolation approaches for $0\nu\beta\beta$-decay observables remain largely unexplored. Guided by the similarities of the observable's r-dependence seen in Ref. [48] to that of nuclear interactions, we employ the same simple exponential form applied for the energy to extrapolate the $0\nu\beta\beta$-decay contributions. While we acknowledge a thorough investigation of extrapolating $0\nu\beta\beta$-decay NMEs is warranted for refined predictions and accurate uncertainty estimates, we find this form provides an adequate fit and proves sufficient for this comparative study.

To facilitate our discussion of convergence, we refer to the speed (with respect to the cutoff parameters) at which an operator eigenvalue approaches its asymptotic value as the result's "convergence rate". We gauge the convergence rate with the value of $N_{\max}$ ($e_{\max}$) at which the extrapolation is within 5% of its value at the continuum limit, denoting this generally non-integer value $\widetilde{N}_{5\%}$ ($\widetilde{e}_{5\%}$). While this metric relies heavily on the validity of the extrapolation, it provides a functional estimate for both the relative convergence speeds between results and approximate cutoffs required for reaching well-converged values. In addition, there is good reason from a theoretical

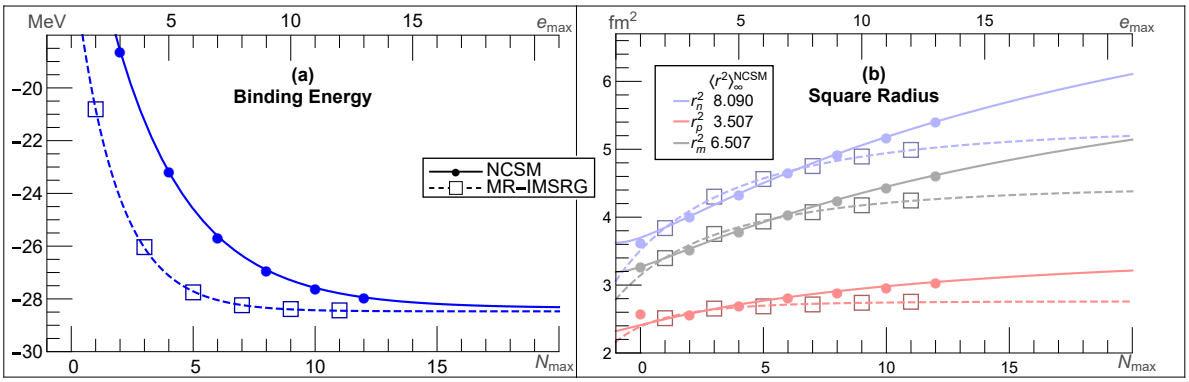

Figure 5.2 Ground-State energy (a) and neutron (light blue), proton (light red), and matter (gray) square radii (r_n^2, r_p^2, and r_m^2 respectively) (b) of ^{6}He with varying basis cutoff parameter from NCSM (solid circle) and MR-IMSRG(2) (open square) *ab initio* calculations. Solid and dashed lines denote the NCSM and MR-IMSRG extrapolations, respectively. The realistic N3LO-EM500 potential with energy scale $\hbar\Omega = 20$ MeV and SRG evolution scale $\lambda = 2.0$ fm^{-1} is used in all cases. The asymptotic fit parameter, $\langle r^2 \rangle_\infty$, of the NCSM square radius extrapolations are listed in the legend of (b) (see Eq. (5.23) for extrapolation definition). Fit parameters and plotted values are listed in Table (5.1) for energy, and in Table (5.2) for the square radii.

perspective to expect the same extrapolation forms effective for the NCSM will be effective for the results of IMSRG calculation [61].

Finally, in the interest of understanding what the differences between the extrapolated results of the two *ab initio* calculations signify, we briefly consider the general A-body system. For such a system, the untruncated MR-IMSRG calculation would include all many-body correlations, and would therefore provide identical results (within numerical noise) as the NCSM at the continuum limit. By performing only the MR-IMSRG(2) calculation, we expect the two approaches' results to converge to different values based on how significant the neglected three-body (up to A-body) correlations are to the observable in question. Thus, beyond the mild uncertainty introduced by the extrapolation, differences between the extrapolated results estimate the significance of many-body correlations neglected by the MR-IMSRG(2) calculation.

5.5.1 Ground-state energy and nuclear square radius

The initial system is the ^{6}He nucleus in its ground state. The calculated ground-state energy and neutron, proton, and matter square radii (r_n^2, r_p^2, and r_m^2 respectively) varying with basis truncation are shown in panels (a) and (b) of Fig. (5.2) respectively.

The NCSM ground-state energy extrapolation has converged to within 5% of its asymptotic value of -28.35 MeV by $\widetilde{N}_{5\%} \sim 8.1$. The MR-IMSRG(2) extrapolated energy converges somewhat faster by comparison, with $\widetilde{e}_{5\%} \sim 4.9$ and the asymptotic value of -28.47 MeV. We observe that the MR-IMSRG(2) results and extrapolation at a given $N_{\max}$ consistently match the NCSM results and extrapolation at roughly $2N_{\max}$, from $N_{\max} \sim 2$ onward. Considering how the $e_{\max}$ basis will include two-body excitations up to $2e_{\max}$ and the MR-IMSRG(2) truncation employed, this supports the observation that the energies of this system can be reproduced well with only up to 2p2h excitations. Both extrapolated ground-state energies are about 1 MeV greater than the experimental result of -29.27 MeV [67]. They are also about 1.7 MeV greater than the extrapolated results of -30.0(1) MeV and -29.87 MeV from two similar (but independent) NCFC calculations of the ^{6}He ground-state [68, 65] that used only the charge-independent parts of our strong-interaction Hamiltonian.

Unlike the ground-state energy, the MR-IMSRG(2) (NCSM) square radii converge much faster (slower), with $\widetilde{e}_{5\%} \sim 14$, 3.5, 12 ($\widetilde{N}_{5\%} \sim 71$, 30, 63) for neutron, proton, and matter square radii, respectively. This difference in convergence speed is primarily a result of the use of natural orbitals in the MR-IMSRG. Notably however, we observe the MR-IMSRG(2) results converge to a roughly 34%, 21%, and 32% smaller value than the NCSM results for the corresponding square radii. All radii share the slower convergence rate relative to the ground-state energy that is commonly associated with the r^2 operator; a consequence of coming from an effective operator with significant correlations outside the characteristic length scale of the chosen HO basis [56, 38, 69–71]. In the NCSM (and to a lesser degree MR-IMSRG), the slow convergence reflects the regularization of the infrared (IR) momentum region from the HO basis truncation. In effect, because the basis's length scale is chosen to favor convergence in energy, the basis requires higher cutoffs to fully capture the longer-range

correlations of the r^2 operator. The significantly faster convergence speed of the proton square radius (compared to those of the neutron and matter square radii) is a consequence of this effect, as the protons predominantly remain in the core of the ^{6}He ground-state halo structure [72]. That is, since the protons are only found in the four-nucleon core, the proton square radius operator correlations primarily only exist at the shorter distances pertinent to the core, and are thus better encompassed by the scales of the chosen basis.

The benefit of the MR-IMSRG's renormalization can be seen in the improved convergence observed in its results. In essence, the renormalization decouples the NN-correlations existing outside the scales encompassed by the basis, and distributes those correlations inside those scales. The drawback is that some induced many-body forces must be neglected in the process, an approximation that would explain the notable differences seen in the extrapolated square radii. We conjecture that the smaller MR-IMSRG(2) square radii reflect meaningful induced many-body correlations that are being lost through the MR-IMSRG(2) many-body truncation. Specifically, the fast convergence of the MR-IMSRG(2) results suggests that the 1p1h and 2p2h correlations relevant to the r^2 are well-accounted for by $e_{\max} = 12$ and 24, respectively, and that the remaining differences with the NCSM results are from higher many-body correlations omitted by the MR-IMSRG(2) approach.

5.5.2 $0\nu\beta\beta$ matrix element

We turn finally to the ground-state-to-ground-state ^{6}He $\rightarrow$ ^{6}Be $0\nu\beta\beta$-decay NME. As already mentioned, we assume isospin symmetry so that the initial and final state are described by the same wavefunction (except for an interchange of protons and neutrons). We present our results in Fig. (5.3), where we recall that discrete points represent results of many-body calculations while lines represent fits specified by Eq. (5.22). We decompose the total NME shown in (a) into its Fermi, GT, and tensor contributions from Eq. (5.7) in panels (b), (c) and (d), respectively. Insets provide estimates for the percent difference, $\Delta_{\%}$, between the results of the two methods within our mapping of their basis truncation schemes (we omit such estimates for the numerically less

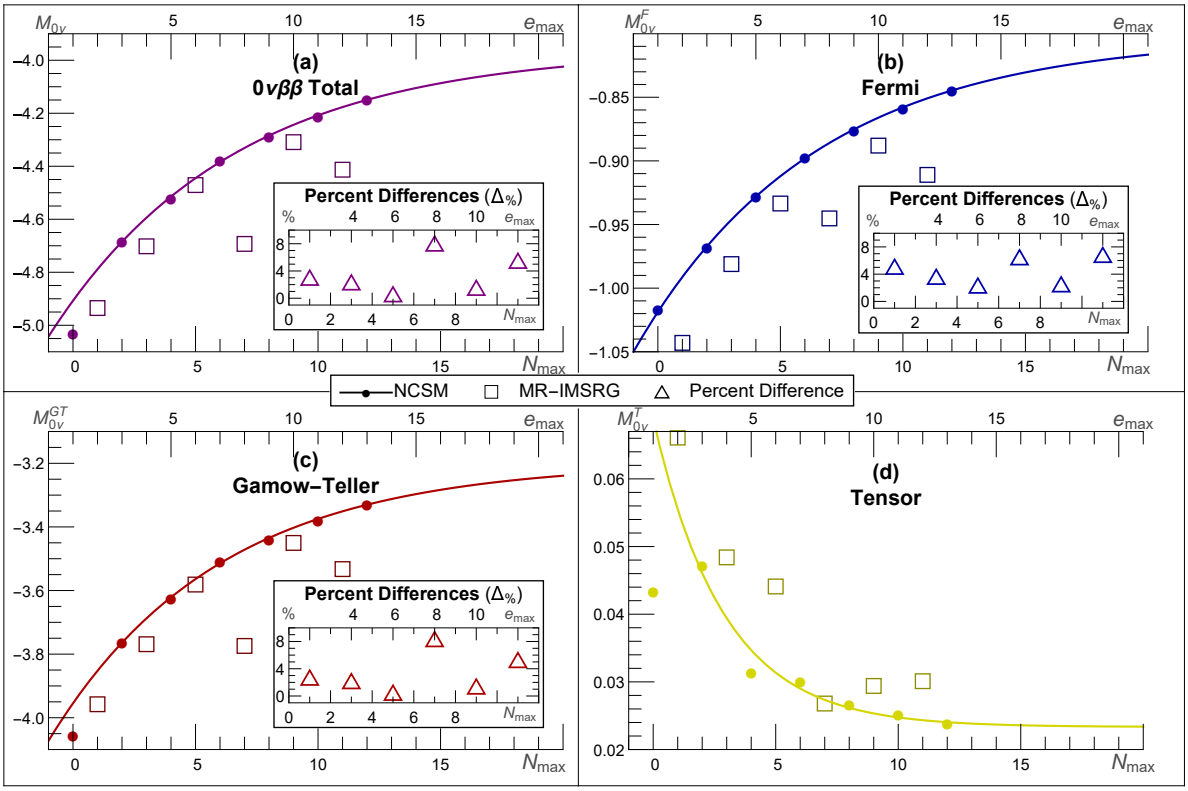

Figure 5.3 Ground-state-to-ground-state $0\nu\beta\beta$-decay NME (a) for ^{6}He $\rightarrow$ ^{6}Be , decomposed into its Fermi (b), GT (c), and tensor (d) contributions, as a function of the basis cutoff for NCSM (solid circle) and MR-IMSRG(2) (open square) *ab initio* calculations. Solid lines denote NCSM extrapolations. Each vertical axis is expanded for visibility. The three contributions add to the total as specified by Eq. (5.7)). Insets provide the percent difference in magnitude (open triangles) between the MR-IMSRG results and the NCSM extrapolation as described in the text. Plotted values and fit parameters are listed in Table (5.1).

significant tensor contribution). For a given $e_{\max}$, we calculate these values as

$$(\Delta_{\%})_{e_{\max}} = 200 \left| \frac{\left(M_{0\nu}^{\mathrm{IMSRG}}\right)_{e_{\max}} - f\left([N_{\max}]_{e_{\max}}\right)}{\left(M_{0\nu}^{\mathrm{IMSRG}}\right)_{e_{\max}} + f\left([N_{\max}]_{e_{\max}}\right)} \right| , \tag{5.21}$$

where $\left(M_{0\nu}^{\mathrm{IMSRG}}\right)_{e_{\max}}$ is the NME result of the MR-IMSRG(2) calculation with cutoff $e_{\max}$, and $f\left(N_{\max}\right)$ is the NCSM fit described by Eq. (5.22) evaluated at the mapped cutoff value $[N_{\max}]_{e_{\max}} = e_{\max} - 1$ (visualized in the figure by the intersection of a vertical line between each open square and the NCSM extrapolation). While, much like the mapping between cutoffs, these estimates require some level of arbitration, we nevertheless find them a reasonable and useful tool for gauging the differences between methods.

The $0\nu\beta\beta$-decay NMEs from the NCSM and MR-IMSRG approaches agree remarkably well. Although the results of the MR-IMSRG(2) calculations reflect significantly larger fluctuations with each step in the basis cutoff, those fluctuations consistently remain less than a few percent of the converged value, and the overall trends remain quite similar to those of the NCSM. More importantly, the contributions, especially the larger Fermi and GT contributions, show excellent agreement between approaches.

The relative magnitudes of the contributions agree between approaches. The GT contribution is around four times greater than the Fermi contribution, while the tensor contribution is roughly two orders of magnitude smaller and of opposite sign. The Fermi, GT, tensor, and total NME results have $\widetilde{N}_{5\%} \sim 12.4$, 10.7, 10.5, 11.7, respectively, which suggests only slightly slower convergence than that of the energy but still significantly faster than the NCSM square radii.

The MR-IMSRG $0\nu\beta\beta$-decay results resemble a saw-tooth pattern for results beyond $e_{\max} = 4$ that gradually decreases in magnitude as $e_{\max}$ increases. The maximum deviation of this pattern occurs in the GT contribution and reaches the order of a few percent. The deviations of the tensor contribution appear less systematic, though this may be a consequence of the contribution's relatively small magnitude. The deviations in the Fermi and GT results of the MR-IMSRG share a sign and are most visible at $e_{\max} = 8$, where they consistently deviate in the negative direction.

A mildly similar (though less pronounced) saw-tooth pattern is observed in the tensor contribution of the NCSM results at the lowest $N_{\max}$ cutoffs. Within NCSM calculations, such patterns (sometimes called "odd-even effects") are generally the consequence of alternating signs in the asymptotic tails of the HO basis wavefunctions that are introduced with each increment in $N_{\max}$ [73]. In such cases, as the tail region of the calculated wavefunction shifts with each increment, the tail begins to overlap a region in which the effective operator is particularly active (i.e., has dominant correlations). If the span of that active region is long enough to require multiple steps in $N_{\max}$ for the tail to pass through, the result is a visible contribution to the observable that alternates in sign. Naturally, the pattern disappears as $N_{\max}$ increases enough so that the effective operator's range is more completely encompassed by that of the basis.

Ostensibly, one might wonder if the pattern observed in the MR-IMSRG $0\nu\beta\beta$-decay results might reflect a similar effect. However, considering our MR-IMSRG(2) calculations employ natural orbitals and not HO wavefunctions, the pattern's similarity may be entirely circumstantial. Determining the origin of these deviations in the MR-IMSRG results will require further study.

Despite these fluctuations making it somewhat challenging to make more than qualitative observations, the trends of the NCSM and MR-IMSRG results are remarkably similar. Indeed, the differences in the asymptotic limits of the square radii in Fig. (5.2) do not appear indicative of similar differences in the $0\nu\beta\beta$-decay NME results. Similarly however, the more rapid convergence observed in the MR-IMSRG(2) ground-state energy and square radii compared to that of the NCSM does not appear to translate into a more rapid convergence of the $0\nu\beta\beta$-decay NMEs in Fig. (5.3). The differences between the two approach's $0\nu\beta\beta$-decay results appear to be of similar magnitudes as the saw-tooth deviations present in the MR-IMSRG(2) results, and does not exceed 5% for the total $0\nu\beta\beta$-decay NME at the maximum basis cutoff employed for each method.

If we compare our extrapolated $0\nu\beta\beta$-decay NMEs to those calculated in the VMC approach with 3N correlations included [40], we see that the magnitudes of both the GT and Fermi contributions agree to within about 15%, while those of the tensor contribution agree to within about 10%. For all three contributions, the VMC results are larger. These differences may suggest a modest correction

from 3N correlations, though other differences between our study and the VMC study may play a significant role as well.

5.6 Conclusion

We find significant agreement between the NCSM and MR-IMSRG results in our investigation of $0\nu\beta\beta$-decay in the $A = 6$ system. The difference in the calculated ground-state energy is only about $\sim 0.5\%$. We see measurable differences in the square radius results that offer an estimate for the effects of correlations that are omitted by the MR-IMSRG(2) truncation at the normal-ordered two-body level. It is interesting that these differences do not extend to the $0\nu\beta\beta$-decay NMEs, which are remarkably similar in the two approaches, differing by only $\sim 4.5\%$ in the total NME at the largest basis cutoffs considered. The convergence rate of the $0\nu\beta\beta$-decay NMEs appears to be comparable to that of the energies.

The GT contribution dominates the $0\nu\beta\beta$-decay NME, comprising $\sim$ 80% of its total. The Fermi contribution makes up most of the remainder, and the tensor contribution is roughly two orders of magnitude smaller and of opposite sign.

Our estimates of the differences in the total $0\nu\beta\beta$-decay NME between the two approaches do not exceed 9% for any of the basis cutoffs considered. Fluctuations in the MR-IMSRG results could pose a minor obstacle for extrapolation, though their consistent saw-tooth appearance may suggest these fluctuations are systematically correctable. Beyond these fluctuations, the two approaches result in qualitatively similar convergence for the $0\nu\beta\beta$-decay NME. This benchmark study lends support to the application of MR-IMSRG to $0\nu\beta\beta$-decay in heavier nuclei, where it is computationally more feasible than the NCSM. The good agreement between the two approaches for $0\nu\beta\beta$-decay NMEs is a promising sign.

5.7 Acknowledgements

We acknowledge fruitful discussions with Sofia Quaglioni, Peter Gysbers, Soham Pal, Shiplu Sarker, and Weijie Du. This work was supported in part by the US Department of Energy (DOE),

Office of Science, under Grant Nos. DE-FG02-87ER40371, DE-SC0018223 (SciDAC-4/NUCLEI), DE-SC0015376 (DOE Topical Collaboration in Nuclear Theory for Double-Beta Decay and Fundamental Symmetries), DE-SC0017887, and DE-FG02-97ER41019. Computational resources were provided by the National Energy Research Scientific Computing Center (NERSC), which is supported by the US DOE Office of Science under Contract No. DE-AC02-05CH11231.

5.8 Extrapolation methods

In this work, we perform all extrapolations by using a non-linear least-squares fit to a form that is specific to each observable and varies with cutoff parameter. The fitting process is iterated until all fit parameters have converged to at least 10 digits of precision. We apply forms identically for both NCSM and MR-IMSRG extrapolations, treating the former as functions of $N_{\max}$ and the latter as functions of $e_{\max}$. We use $X_{\max}$ to denote either cutoff parameter when defining the extrapolations provided below. Following a common NCFC practice, we do not include the $N_{\max} = 0$ result when performing fits to any of the NCSM data sets. The extrapolation for each data set is performed without regard to any other data sets or their extrapolations. The formulae for ground-state energy and square radius are applied identically to both NCSM and MR-IMSRG results. Extrapolations for $0\nu\beta\beta$-decay NMEs are only performed for the NCSM results because of fluctuations in the MR-IMSRG results.

It should be noted that the extrapolations described here were originally designed with the $N_{\max}$ truncation scheme in mind, and their effectiveness for extrapolating results in the $e_{\max}$ truncation scheme has not yet been fully explored. Nevertheless, the significant similarities of the two schemes and their quantization of the same underlying variable (i.e. the content of the many-body basis) suggest the same extrapolation forms may be effective; an expectation that is supported by the results of this work.

Motivated by the extrapolations proposed in Ref. [60], we extrapolate the ground-state energy to the form

$$f\left(X_{\max}\right) = a + b \cdot e^{-cX_{\max}} \tag{5.22}$$

where a, b, and c are fit parameters. We employ the same form for our extrapolations of the NCSM $0\nu\beta\beta$-decay results. Values of fit parameters calculated in this study for energy and $0\nu\beta\beta$-decay NMEs may be found in the right-most columns of Table (5.1) alongside their corresponding data set.

The simple exponential form depicted in Eq. (5.22) generally provides a poor prediction for the convergence behavior of square radius operator observables. Thus, inspired by the methods discussed in Ref. [65], we extrapolate square radii by fitting to the form

$$\langle r^2 \rangle = \langle r^2 \rangle_\infty - \left(c_0\beta + c_1\beta^3\right) e^{-\beta}\,, \tag{5.23}$$

where

$$\beta \equiv 2k_\infty \frac{\hbar}{m\Omega}\left[\sqrt{2X_{\max}+5} + 0.54437\left(2X_{\max}+5\right)^{1/6}\right].$$

Here $m = 938.92$ MeV is the average mass of a neutron and a proton, and $\langle r^2 \rangle_\infty$, c_0, and c_1 are fit parameters. Unlike the authors of Ref. [65] who determine k_∞ while extrapolating the ground-state energy with their theoretically-founded "IR formula", we treat k_∞ as an additional fit parameter when extrapolating each square radius. We provide our calculated values of the fit parameters for each square radius extrapolation alongside its corresponding data set in Table (5.2).

References

[1] Q. R. Ahmad et al. Measurement of the rate of $\nu_e + d \rightarrow p + p + e^-$ interactions produced by ^8B solar neutrinos at the Sudbury Neutrino Observatory. *Phys. Rev. Lett.*, 87:071301, 2001. doi: 10.1103/PhysRevLett.87.071301.

[2] K. Eguchi et al. First results from KamLAND: Evidence for reactor anti-neutrino disappearance. *Phys. Rev. Lett.*, 90:021802, 2003. doi: 10.1103/PhysRevLett.90.021802.

[3] Y. Fukuda et al. Evidence for oscillation of atmospheric neutrinos. *Phys. Rev. Lett.*, 81: 1562–1567, 1998. doi: 10.1103/PhysRevLett.81.1562.

[4] J. Martin-Albo et al. Sensitivity of NEXT-100 to Neutrinoless Double Beta Decay. *JHEP*, 05: 159, 2016. doi: 10.1007/JHEP05(2016)159.

[5] J. B. Albert et al. Search for Majorana neutrinos with the first two years of EXO-200 data. *Nature*, 510:229–234, 2014. doi: 10.1038/nature13432.

[6] T. Gilliss et al. Recent Results from the Majorana Demonstrator. *Int. J. Mod. Phys. Conf. Ser.*, 46:1860049, 2018. doi: 10.1142/S2010194518600492.

[7] A. Gando, Y. Gando, T. Hachiya, A. Hayashi, S. Hayashida, H. Ikeda, K. Inoue, K. Ishidoshiro, Y. Karino, et al. Search for Majorana Neutrinos near the Inverted Mass Hierarchy Region with KamLAND-Zen. *Phys. Rev. Lett.*, 117(8):082503, 2016. doi: 10.1103/PhysRevLett.117.109903, 10.1103/PhysRevLett.117.082503. [Addendum: Phys. Rev. Lett.117,no.10,109903(2016)].

[8] K. Alfonso et al. Search for Neutrinoless Double-Beta Decay of ^{130}Te with CUORE-0. *Phys. Rev. Lett.*, 115(10):102502, 2015. doi: 10.1103/PhysRevLett.115.102502.

[9] M. Agostini et al. Background-free search for neutrinoless double-β decay of ^{76}Ge with GERDA. 2017. doi: 10.1038/nature21717. [Nature544,47(2017)].

[10] C. E. Aalseth et al. Search for Neutrinoless Double-β Decay in ^{76}Ge with the Majorana Demonstrator. *Phys. Rev. Lett.*, 120(13):132502, 2018. doi: 10.1103/PhysRevLett.120.132502.

[11] S. Andringa et al. Current Status and Future Prospects of the SNO+ Experiment. *Adv. High Energy Phys.*, 2016:6194250, 2016. doi: 10.1155/2016/6194250.

[12] Y. Iwata, N. Shimizu, T. Otsuka, Y. Utsuno, J. Menèndez, M. Honma, and T. Abe. Large-scale shell-model analysis of the neutrinoless $\beta\beta$ decay of ^{48}Ca. *Phys. Rev. Lett.*, 116(11): 112502, 2016. doi: 10.1103/PhysRevLett.117.179902,10.1103/PhysRevLett.116.112502. [Erratum: Phys. Rev. Lett.117,no.17,179902(2016)].

[13] V. Cirigliano, W. Dekens, J. de Vries, M. L. Graesser, and E. Mereghetti. Neutrinoless double beta decay in chiral effective field theory: lepton number violation at dimension seven. *JHEP*, 12:082, 2017. doi: 10.1007/JHEP12(2017)082.

[14] L. Contessi, A. Lovato, F. Pederiva, A. Roggero, J. Kirscher, and U. van Kolck. Ground-state properties of ^{4}He and ^{16}O extrapolated from lattice QCD with pionless EFT. *Phys. Lett.*, B772: 839–848, 2017. doi: 10.1016/j.physletb.2017.07.048.

[15] L. Coraggio, L. De Angelis, T. Fukui, A. Gargano, and N. Itaco. Calculation of Gamow-Teller and two-neutrino double- β decay properties for ^{130}Te and ^{136}Xe with a realistic nucleon-nucleon potential. *Phys. Rev.*, C95(6):064324, 2017. doi: 10.1103/PhysRevC.95.064324.

[16] C. F. Jiao, J. Engel, and J. D. Holt. Neutrinoless double-beta decay matrix elements in large shell-model spaces with the generator-coordinate method. *Phys. Rev.*, C96(5):054310, 2017. doi: 10.1103/PhysRevC.96.054310.

[17] Brian C. Tiburzi, Michael L. Wagman, Frank Winter, Emmanuel Chang, Zohreh Davoudi, William Detmold, Kostas Orginos, Martin J. Savage, and Phiala E. Shanahan. Double-β Decay Matrix Elements from Lattice Quantum Chromodynamics. *Phys. Rev.*, D96(5):054505, 2017. doi: 10.1103/PhysRevD.96.054505.

[18] Phiala E. Shanahan, Brian C. Tiburzi, Michael L. Wagman, Frank Winter, Emmanuel Chang, Zohreh Davoudi, William Detmold, Kostas Orginos, and Martin J. Savage. Isotensor Axial Polarizability and Lattice QCD Input for Nuclear Double-β Decay Phenomenology. *Phys. Rev. Lett.*, 119(6):062003, 2017. doi: 10.1103/PhysRevLett.119.062003.

[19] Mihai Horoi and Andrei Neacsu. Towards an effective field theory approach to the neutrinoless double-beta decay. 2017.

[20] O. Cremonesi and M. Pavan. Challenges in Double Beta Decay. *Adv. High Energy Phys.*, 2014: 951432, 2014. doi: 10.1155/2014/951432.

[21] Stefano Dell'Oro, Simone Marcocci, Matteo Viel, and Francesco Vissani. Neutrinoless double beta decay: 2015 review. *Adv. High Energy Phys.*, 2016:2162659, 2016. doi: 10.1155/2016/2162659.

[22] Jonathan Engel and Javier Menèndez. Status and Future of Nuclear Matrix Elements for Neutrinoless Double-Beta Decay: A Review. *Rept. Prog. Phys.*, 80(4):046301, 2017. doi: 10.1088/1361-6633/aa5bc5.

[23] J. J. Gomez-Cadenas, J. Martin-Albo, M. Mezzetto, F. Monrabal, and M. Sorel. The Search for neutrinoless double beta decay. *Riv. Nuovo Cim.*, 35:29–98, 2012. doi: 10.1393/ncr/i2012-10074-9.

[24] Reyco Henning. Current status of neutrinoless double-beta decay searches. *Rev. Phys.*, 1:29–35, 2016. doi: 10.1016/j.revip.2016.03.001.

[25] P. Gysbers et al. Discrepancy between experimental and theoretical β-decay rates resolved from first principles. *Nature Phys.*, 15(5):428–431, 2019. doi: 10.1038/s41567-019-0450-7.

[26] S. K. Bogner, H. Hergert, J. D. Holt, A. Schwenk, S. Binder, A. Calci, J. Langhammer, and R. Roth. Nonperturbative shell-model interactions from the in-medium similarity renormalization group. *Phys. Rev. Lett.*, 113:142501, 2014. doi: 10.1103/PhysRevLett.113.142501.

[27] G. R. Jansen, J. Engel, G. Hagen, P. Navràtil, and A. Signoracci. Ab-initio coupled-cluster effective interactions for the shell model: Application to neutron-rich oxygen and carbon isotopes. *Phys. Rev. Lett.*, 113(14):142502, 2014. doi: 10.1103/PhysRevLett.113.142502.

[28] G. R. Jansen, M. D. Schuster, A. Signoracci, G. Hagen, and P. Navràtil. Open *sd*-shell nuclei from first principles. *Phys. Rev.*, C94(1):011301(R), 2016. doi: 10.1103/PhysRevC.94.011301.

[29] S. R. Stroberg, H. Hergert, J. D. Holt, S. K. Bogner, and A. Schwenk. Ground and excited states of doubly open-shell nuclei from ab initio valence-space Hamiltonians. *Phys. Rev.*, C93 (5):051301(R), 2016. doi: 10.1103/PhysRevC.93.051301.

[30] S. R. Stroberg, A. Calci, H. Hergert, J. D. Holt, S. K. Bogner, R. Roth, and A. Schwenk. A nucleus-dependent valence-space approach to nuclear structure. *Phys. Rev. Lett.*, 118(3): 032502, 2017. doi: 10.1103/PhysRevLett.118.032502.

[31] E. Dikmen, A. F. Lisetski, B. R. Barrett, P. Maris, A. M. Shirokov, and J. P. Vary. Ab initio effective interactions for sd-shell valence nucleons. *Phys. Rev.*, C91(6):064301, 2015. doi: 10.1103/PhysRevC.91.064301.

[32] Bruce R. Barrett, Erdal Dikmen, Pieter Maris, Andrey M. Shirokov, Nadya A. Smirnova, and James P. Vary. Microscopic Shell Model Calculations for sd-Shell Nuclei. *JPS Conf. Proc.*, 14: 021006, 2017. doi: 10.7566/JPSCP.14.021006.

[33] L. S. Song, J. M. Yao, P. Ring, and J. Meng. Nuclear matrix element of neutrinoless double-β decay: Relativity and short-range correlations. *Phys. Rev.*, C95(2):024305, 2017. doi: 10.1103/PhysRevC.95.024305.

[34] J. M. Yao, J. Engel, L. J. Wang, C. F. Jiao, and H. Hergert. Generator-coordinate reference states for spectra and $0\nu\beta\beta$ decay in the in-medium similarity renormalization group. *Phys. Rev.*, C98(5):054311, 2018. doi: 10.1103/PhysRevC.98.054311.

[35] D. R. Entem and R. Machleidt. Accurate charge dependent nucleon nucleon potential at fourth order of chiral perturbation theory. *Phys. Rev.*, C68:041001, 2003. doi: 10.1103/PhysRevC.68.041001.

[36] R. Machleidt and D. R. Entem. Chiral effective field theory and nuclear forces. *Phys. Rept.*, 503:1–75, 2011. doi: 10.1016/j.physrep.2011.02.001.

[37] S. K. Bogner, R. J. Furnstahl, and A. Schwenk. From low-momentum interactions to nuclear structure. *Prog. Part. Nucl. Phys.*, 65:94–147, 2010. doi: 10.1016/j.ppnp.2010.03.001.

[38] Chase Cockrell, James P. Vary, and Pieter Maris. Lithium isotopes within the ab intio no-core full configuration approach. *Phys. Rev.*, C86:034325, 2012. doi: 10.1103/PhysRevC.86.034325.

[39] Ik Jae Shin, Youngman Kim, Pieter Maris, James P. Vary, Christian Forssén, Jimmy Rotureau, and Nicolas Michel. Ab initio no-core solutions for ^{6}Li. *J. Phys.*, G44(7):075103, 2017. doi: 10.1088/1361-6471/aa6cb7.

[40] S. Pastore, J. Carlson, V. Cirigliano, W. Dekens, E. Mereghetti, and R. B. Wiringa. Neutrinoless double-β decay matrix elements in light nuclei. *Phys. Rev.*, C97(1):014606, 2018. doi: 10.1103/PhysRevC.97.014606.

[41] Frank T. Avignone, III, Steven R. Elliott, and Jonathan Engel. Double Beta Decay, Majorana Neutrinos, and Neutrino Mass. *Rev. Mod. Phys.*, 80:481–516, 2008. doi: 10.1103/RevModPhys.80.481.

[42] F. Simkovic, G. Pantis, J. D. Vergados, and Amand Faessler. Additional nucleon current contributions to neutrinoless double beta decay. *Phys. Rev.*, C60:055502, 1999. doi: 10.1103/PhysRevC.60.055502.

[43] J. Kotila and F. Iachello. Phase space factors for double-β decay. *Phys. Rev.*, C85:034316, 2012. doi: 10.1103/PhysRevC.85.034316.

[44] Sabin Stoica and Mihail Mirea. New calculations for phase space factors involved in double-β decay. *Phys. Rev.*, C88(3):037303, 2013. doi: 10.1103/PhysRevC.88.037303.

[45] Mihai Horoi and Sabin Stoica. Shell Model Analysis of the Neutrinoless Double Beta Decay of Ca-48. *Phys. Rev.*, C81:024321, 2010. doi: 10.1103/PhysRevC.81.024321.

[46] V. A. Rodin, A. Faessler, F. Simkovic, and P. Vogel. Assessment of uncertainties in QRPA $0\nu\beta\beta$-decay nuclear matrix elements. *Nucl. Phys.*, A766:107–131, 2006. doi: 10.1016/j.nuclphysa.2007.06.014,10.1016/j.nuclphysa.2005.12.004. [Erratum: Nucl. Phys.A793,213(2007)].

[47] Jouni Suhonen. *From Nucleons to Nucleus*. Theoretical and Mathematical Physics. Springer, Berlin, Germany, 2007. ISBN 9783540488613, 9783540488590. doi: 10.1007/978-3-540-48861-3. URL http://www-spires.fnal.gov/spires/find/books/www?cl=QC793.3.S8S84::2007.

[48] Fedor Simkovic, Amand Faessler, Vadim Rodin, Petr Vogel, and Jonathan Engel. Anatomy of nuclear matrix elements for neutrinoless double-beta decay. *Phys. Rev.*, C77:045503, 2008. doi: 10.1103/PhysRevC.77.045503.

[49] Fedor Simkovic, Amand Faessler, Herbert Muther, Vadim Rodin, and Markus Stauf. The 0 nu bb-decay nuclear matrix elements with self-consistent short-range correlations. *Phys. Rev.*, C79:055501, 2009. doi: 10.1103/PhysRevC.79.055501.

[50] Gerald A. Miller and James E. Spencer. A Survey of Pion Charge-Exchange Reactions with Nuclei. *Annals Phys.*, 100:562, 1976. doi: 10.1016/0003-4916(76)90073-7.

[51] R. Roth, H. Hergert, P. Papakonstantinou, T. Neff, and H. Feldmeier. Matrix elements and few-body calculations within the unitary correlation operator method. *Phys. Rev.*, C72:034002, 2005. doi: 10.1103/PhysRevC.72.034002.

[52] K. A. Brueckner. Many-Body Problem for Strongly Interacting Particles. 2. Linked Cluster Expansion. *Phys. Rev.*, 100:36–45, 1955. doi: 10.1103/PhysRev.100.36.

[53] Omar Benhar, Riccardo Biondi, and Enrico Speranza. Short-range correlation effects on the nuclear matrix element of neutrinoless double-β decay. *Phys. Rev.*, C90(6):065504, 2014. doi: 10.1103/PhysRevC.90.065504.

[54] H. Muther and A. Polls. Two-body correlations in nuclear systems. *Prog. Part. Nucl. Phys.*, 45:243–334, 2000. doi: 10.1016/S0146-6410(00)00105-8.

[55] W. Tobocman. A generalized Talmi-Moshinsky transformation for few-body and direct interaction matrix elements. *Nucl. Phys.*, A357:293–318, 1981. doi: 10.1016/0375-9474(81)90223-2.

[56] Bruce R. Barrett, Petr Navràtil, and James P. Vary. Ab initio no core shell model. *Prog. Part. Nucl. Phys.*, 69:131–181, 2013. doi: 10.1016/j.ppnp.2012.10.003.

[57] Pieter Maris, Masha Sosonkina, James P. Vary, Esmond Ng, and Chao Yang. Scaling of ab-initio nuclear physics calculations on multicore computer architectures. *Procedia Computer Science*, 1(1):97 – 106, 2010. ISSN 1877-0509. doi: https://doi.org/10.1016/j.procs.2010.04.012. URL http://www.sciencedirect.com/science/article/pii/S187705091000013X. ICCS 2010.

[58] Hasan M. Aktulga, Chao Yang, Esmond G. Ng, Pieter Maris, and James P. Vary. Improving the scalability of a symmetric iterative eigensolver for multi-core platforms. 26, 11 2014.

[59] Meiyue Shao, Hasan Metin Aktulga, Chao Yang, Esmond G. Ng, Pieter Maris, and James P. Vary. Accelerating nuclear configuration interaction calculations through a preconditioned block iterative eigensolver. *Computer Physics Communications*, 222, 9 2017. doi: 10.1016/j.cpc.2017.09.004.

[60] P. Maris, J. P. Vary, and A. M. Shirokov. Ab initio no-core full configuration calculations of light nuclei. *Phys. Rev.*, C79:014308, 2009. doi: 10.1103/PhysRevC.79.014308.

[61] H. Hergert, S. K. Bogner, T. D. Morris, A. Schwenk, and K. Tsukiyama. The In-Medium Similarity Renormalization Group: A Novel Ab Initio Method for Nuclei. *Phys. Rept.*, 621: 165–222, 2016. doi: 10.1016/j.physrep.2015.12.007.

[62] H. Hergert. In-Medium Similarity Renormalization Group for Closed and Open-Shell Nuclei. *Phys. Scripta*, 92(2):023002, 2017. doi: 10.1088/1402-4896/92/2/023002.

[63] Heiko Hergert, Jiangming Yao, Titus D. Morris, Nathan M. Parzuchowski, Scott K. Bogner, and Jonathan Engel. Nuclear Structure from the In-Medium Similarity Renormalization Group. *J. Phys. Conf. Ser.*, 1041(1):012007, 2018. doi: 10.1088/1742-6596/1041/1/012007.

[64] T. D. Morris, N. Parzuchowski, and S. K. Bogner. Magnus expansion and in-medium similarity renormalization group. *Phys. Rev.*, C92(3):034331, 2015. doi: 10.1103/PhysRevC.92.034331.

[65] R. J. Furnstahl, G. Hagen, and T. Papenbrock. Corrections to nuclear energies and radii in finite oscillator spaces. *Phys. Rev.*, C86:031301, 2012. doi: 10.1103/PhysRevC.86.031301.

[66] D. Odell, T. Papenbrock, and L. Platter. Infrared extrapolations of quadrupole moments and transitions. *Phys. Rev.*, C93(4):044331, 2016. doi: 10.1103/PhysRevC.93.044331.

[67] K. Riisager et al. First Observation of Beta Delayed Deuteron Emission. *Phys. Lett.*, B235: 30–34, 1990. doi: 10.1016/0370-2693(90)90091-J.

[68] S. K. Bogner, R. J. Furnstahl, P. Maris, R. J. Perry, A. Schwenk, and J. P. Vary. Convergence in the no-core shell model with low-momentum two-nucleon interactions. *Nucl. Phys.*, A801: 21–42, 2008. doi: 10.1016/j.nuclphysa.2007.12.008.

[69] R. J. Furnstahl, S. N. More, and T. Papenbrock. Systematic expansion for infrared oscillator basis extrapolations. *Phys. Rev.*, C89(4):044301, 2014. doi: 10.1103/PhysRevC.89.044301.

[70] R. J. Furnstahl, G. Hagen, T. Papenbrock, and K. A. Wendt. Infrared extrapolations for atomic nuclei. *J. Phys.*, G42(3):034032, 2015. doi: 10.1088/0954-3899/42/3/034032.

[71] Sidney A. Coon, Matthew I. Avetian, Michael K. G. Kruse, U. van Kolck, Pieter Maris, and James P. Vary. Convergence properties of *ab initio* calculations of light nuclei in a harmonic oscillator basis. *Phys. Rev.*, C86:054002, 2012. doi: 10.1103/PhysRevC.86.054002.

[72] K. Riisager. Halos and related structures. *Phys. Scripta*, T152:014001, 2013. doi: 10.1088/0031-8949/2013/T152/014001.

[73] James P. Vary, Robert A. M. Basili, Weijie Du, Matthew Lockner, Pieter Maris, Soham Pal, and Shiplu Sarker. Effective operators in two-nucleon systems. *Phys. Rev.*, C98(6):065502, 2018. doi: 10.1103/PhysRevC.98.065502.

Table 5.1 MR-IMSRG(2) and NCSM calculated observables and extrapolation parameters (see Eq. (5.22)). The ground-state energy (E) results correspond to the ^{6}He ground state, and are plotted in Fig. (5.2). The $0\nu\beta\beta$-decay NME ($M_{0\nu}$) results and their decomposition into Fermi (F), Gamow-Teller (GT), and tensor (T) contributions correspond to the $^6\text{He} \rightarrow {}^6\text{Be}$ ground-state-to-ground-state transition, and are plotted in Fig. (5.3). In all calculations of $M_{0\nu}$ and its contributions, isospin symmetry has been assumed. Extrapolations for the $0\nu\beta\beta$-decay NME were only performed using the NCSM results.

		$N_{\max}(e_{\max})$							Fit Parameters		
Observable	Method	0(2)	2(4)	4(6)	6(8)	8(10)	10(12)	12	a	b	c
E (MeV)	NCSM	-11.748	-18.595	-23.1531	-25.639	-26.904	-27.581	-27.929	-28.345	18.438	0.3182
	MR-IMSRG	-20.810	-26.037	-27.752	-28.240	-28.385	-28.435		-28.472	24.375	0.5784
$M^F_{0\nu}$	NCSM	-1.0165	-0.9674	-0.9279	-0.8973	-0.8759	-0.8587	-0.8440	-0.8022	-0.2165	0.1358
	MR-IMSRG	-1.0430	-0.9811	-0.9335	-0.9452	-0.8880	-0.9110				
$M^{GT}_{0\nu}$	NCSM	-4.0553	-3.7632	-3.6246	-3.5087	-3.4368	-3.3775	-3.3284	-3.1975	-0.7570	0.1451
	MR-IMSRG	-3.9576	-3.7688	-3.5812	-3.7742	-3.4503	-3.5326				
$M^T_{0\nu}$	NCSM	0.0435	0.0473	0.0314	0.0302	0.0267	0.0252	0.0239	0.0233	0.0455	0.3474
	MR-IMSRG	0.0661	0.0484	0.0441	0.0268	0.0294	0.0301				
$M_{0\nu}$	NCSM	-5.0283	-4.6834	-4.5212	-4.3758	-4.2860	-4.2110	-4.1485	-3.9588	-0.9484	0.1337
	MR-IMSRG	-4.9346	-4.7016	-4.4706	-4.6927	-4.3089	-4.4134				

Table 5.2 MR-IMSRG(2) and NCSM neutron, proton, and matter square radii (r_n^2, r_p^2, and r_m^2, respectively) and corresponding square radius extrapolation parameters (see Eq. (5.23)) for the ^{6}He ground state. The extrapolated fits are plotted alongside their respective results in Fig. (5.2).

		$N_{\max}(e_{\max})$							Fit Parameters			
Observable	Method	0(2)	2(4)	4(6)	6(8)	8(10)	10(12)	12	$\langle r^2\rangle_\infty$	c_0	c_1	k_∞
r_n^2 (fm^2)	NCSM	3.6286	4.0128	4.3401	4.6669	4.9244	5.1738	5.4098	8.0900	10.911	0.9936	0.1241
	MR-IMSRG	3.8389	4.3023	4.5616	4.7524	4.8929	4.9903		5.3226	10.601	0.2827	0.2235
r_p^2 (fm^2)	NCSM	2.5918	2.5767	2.7139	2.8274	2.9029	2.9791	3.0489	3.5073	3.0974	0.1956	0.1510
	MR-IMSRG	2.5125	2.6540	2.6870	2.7149	2.7394	2.7543		2.7598	8.9888	0.0807	0.3546
r_m^2 (fm^2)	NCSM	3.2830	3.5340	3.7982	4.0538	4.2506	4.4424	4.6229	6.5066	8.1260	0.7268	0.1287
	MR-IMSRG	3.3970	3.7527	3.9367	4.0733	4.1751	4.2448		4.4563	8.4272	0.2028	0.2326

CHAPTER 6. FUTURE WORK, SUMMARY, AND CONCLUSION

Throughout this work, we have established the context of modern Nuclear Structure in both a broad sense and as it pertains to NCSM calculation in particular. Beginning from a brief historical review, we introduced the role of *ab initio* approaches in the greater scope of Nuclear Structure, and introduced the NMBP and the formidable challenge it poses. From there, we narrowed our consideration to the NCSM, defined our many-body formalism, identified the computational challenges NCCI calculations involve, and considered some of the techniques by which they are overcome. From there we switched to the relative 2N system, established our treatment, and considered how the problem simplifies to allow the testing of effective tools. With this formalism, we defined the concept of basis regulation, and explored NCFC extrapolation, OLS renormalization, and SRG renormalization as practical tools. This provided the background information useful for properly considering the 2N OLS study performed in Ref. [1], and the NCSM and MR-IMSRG benchmark study performed in Ref. [2].

In the broader sense, we have identified the matters of scale that are a major source of what makes the NMBP so challenging, and have described the contemporary perspective of seeking a UNEM to overcome them. If such a treatment exists, the first step of developing such an approach is to define the realistic, effective inter-nuclear interaction, and modern *ab initio* approaches like the NCSM provide a well-understood method of benchmarking these interactions. Nevertheless, the success of a UNEM will be highly dependent on possessing well-defined and meaningful uncertainty assessment.

At the same time, developing new effective methods and extrapolation approaches to solve the NMBP is critical for modeling heavier nuclei, where the full problem vastly out-scales the development of modern computational resources. Such methods may allow the NCSM or (effective approaches based on it) to explore larger systems, and may also enable the development of entirely

new many-body approaches (like the MR-IMSRG). To this end, their implementation in NCSM calculation and the validation of other approaches require development and benchmarking, for which the works discussed here represent an early step forward. Subsequent steps include expanding both OLS and SRG renormalization to the three-body level, which will be critical for any attempt at their implementation in both light and heavy nuclei, as well as the implementation of a consistent χEFT treatment for both the interaction and operators.

The paths to both bridging QCD to the nuclear scale and the accurate description of 3N forces are open, and we stand in the midst of a whirlwind of development throughout Nuclear Physics that is only growing in intensity. Other pressing research in Physics including, among other examples, the need to calculate from first principles neutrinoless double-beta decay in nuclei of experimental interest, only add to the evolving atmosphere. While there remains a great deal to learn, new methods to develop, and techniques to master in the path ahead, the future of Nuclear Structure appears extremely promising.

References

[1] James P. Vary, Robert A. M. Basili, Weijie Du, Matthew Lockner, Pieter Maris, Soham Pal, and Shiplu Sarker. Effective operators in two-nucleon systems. *Phys. Rev.*, C98(6):065502, 2018. doi: 10.1103/PhysRevC.98.065502.

[2] R. A. M. Basili, J. M. Yao, J. Engel, H. Hergert, M. Lockner, P. Maris, and J. P. Vary. Benchmark neutrinoless double-beta decay matrix elements in a light nucleus. 2019.

APPENDIX. HARMONIC OSCILLATOR MATRIX ELEMENTS

For posterity, we provide analytical expressions for the relative HO matrix elements $\langle\alpha|O|\alpha\rangle$ (for basis states α and α') of the operators (generically denoted here as O) considered in Chapter 4. In most cases these may be considered to reflect the LO contribution for the operator in the χEFT expansion. We use the formalism as described in Section 2.2. For brevity, we consider only quantum numbers relevant to each operator wherever possible, and employ the shorthand $\sum_{\alpha} = \sum_{m_l, m_s} (l\, m_l\, s\, m_s | j\, m_j)$ to denote a summation of Clebsch-Gordan coefficients associated with the change to the good j HO basis, where α also stands for a state's quantum numbers.

It is worth noting that the electric and magnetic multipole expansion terms may be derived generally in regards to the multipole term. However, for the sake of clarity we narrow our view here only to the electric quadrupole and magnetic dipole operators to avoid confusion. Since only the deuteron channel is relevant to this study, for the sake of brevity we define just the static magnetic dipole matrix elements for the ${}^3s_1 - {}^3d_1$ coupled channel (and do not include any corrections from meson exchange).

The analytical expressions provided here commonly rely on the following generalized Laguerre function identities:

$$xL_n^k(x) = (2n+k+1)L_n^k(x) - (n+1)L_{n+1}^k(x) - (n+k)L_{n-1}^k(x)\,, \tag{A.1}$$

$$xL_n^k(x) = (n+k)L_n^{k-1}(x) - (n+1)L_{n+1}^{k-1}(x)\,, \tag{A.2}$$

$$\int_0^\infty x^k e^{-x} L_n^k(x) L_m^k(x) dx = \frac{\Gamma(n+k+1)}{n!}\delta_{n,m} = \frac{(n+k)!}{n!}\delta_{n,m}\,, \tag{A.3}$$

which are derived in Ref. [1]. We also make use of the Wigner-Eckart theorem for tensor operator T_{LM}

$$\langle\alpha'|T_{LM}|\alpha\rangle = (-1)^{j'-m'_j} \begin{pmatrix} j' & L & j \\ -m'_j & M & m_j \end{pmatrix} \left(\alpha'||Y_L||\alpha\right)\,, \tag{A.4}$$

as well as the reduced matrix element for a spherical harmonic

$$\left(\alpha'||Y_L||\alpha\right) = (-1)^{l'} \frac{\hat{l}'\hat{L}\hat{l}}{\sqrt{4\pi}} \begin{pmatrix} l' & L & l \\ 0 & 0 & 0 \end{pmatrix}, \tag{A.5}$$

as provided by Ref. [2].

r^2 and p^2

We solve the $r^2 = b^2\rho$ matrix elements in coordinate space, where $b \equiv \sqrt{\frac{\hbar}{\mu\Omega}}$. Beyond the angular part of the wavefunction requiring $l = l'$, we need only consider the spatial part of the wavefunction

$$\begin{aligned} \langle r^2 \rangle =& N_{nl} N_{n'l} \frac{b}{2} b^2 \int \rho^{l+\frac{1}{2}} e^{-\rho} (\rho L_n^{l+\frac{1}{2}}) L_{n'}^{l+\frac{1}{2}} d\rho \,, \\ (A.1, A.3) \stackrel{\rightarrow}{=}& b^2 \left[(2n + l + \frac{3}{2})\delta_{n,n'} - \sqrt{n(n+l+\frac{1}{2})}\delta_{n,n'+1} - \sqrt{(n+1)(n+l+\frac{3}{2})}\delta_{n,n'-1} \right] . \end{aligned} \tag{A.6}$$

In the given formalism, the rms radius r_{rms} is calculated as

$$r_{rms} = \frac{1}{2}\sqrt{\langle r^2 \rangle} \,. \tag{A.7}$$

Naturally, the p^2 HO matrix elements will be similarly given by Eq. A.6, but with the substitution $b \equiv \sqrt{\frac{\mu\Omega}{\hbar}}$.

Electric quadrupole

The general multipole operator may be expressed in the provided two-body relative frame as

$$Q_{LM} = \left(\frac{r}{2}\right)^L Y_{LM} \,. \tag{A.8}$$

So the matrix elements in the relative HO basis are

$$\begin{aligned}\langle\alpha'|Q_{LM}|\alpha\rangle &= \frac{1}{2^L}\int R_{n'l'}R_{nl}r^{L+2}dr\sum_{\alpha}\sum_{\alpha'}\int Y_{l'm_l'}Y_{LM}Y_{lm_l}d\Omega \\ &= \frac{1}{2^L}\langle n'\,l'|r^L|n\,l\rangle\langle l'\,s'\,j'\,m_j'|Y_{LM}|l\,s\,j\,m_j\rangle \\ &\equiv \frac{1}{2^L}\langle r^L\rangle\langle Y_{LM}\rangle\,, \end{aligned} \tag{A.9}$$

where the third line shows the shorthand notation $\langle r^L\rangle$ and $\langle Y_{LM}\rangle$ we will use.

We first consider the angular part

$$\langle Y_{LM}\rangle = \sum_{m_l,m_s,m_l',m_s'}\left(l'\,m_l'\,s'\,m_s'|j'\,m_j'\right)\left(l\,m_l\,s\,m_s|j\,m_j\right)\int Y_{l'm_l'}Y_{LM}Y_{lm}d\Omega\,. \tag{A.10}$$

We require $m_s = m_s'$ and employ Wigner-Eckart Theorem:

$$\begin{aligned}\langle Y_{LM}\rangle &= \sum_{m_l,m_l',m_s}\hat{l}'^{-1}\left(l'\,m_l'\,s\,m_s|j'\,m_j'\right)\left(l\,m_l\,s\,m_s|j\,m_j\right)\left(l\,m_l\,L\,M\,|l'\,m_l'\right)(l'||Y_L||l) \\ &\overset{(A.5)}{=}(-1)^{l'}\frac{\hat{L}\hat{l}}{\sqrt{4\pi}}\begin{pmatrix} l' & L & l \\ 0 & 0 & 0\end{pmatrix}\sum_{m_l,m_l',m_s}\left(l'\,m_l'\,s\,m_s|j'\,m_j'\right)\left(l\,m_l\,s\,m_s|j\,m_j\right)\left(l\,m_l\,L\,M\,|l'\,m_l'\right)\,. \end{aligned} \tag{A.11}$$

From triangularity we may use the substitutions $m_l = m_j - m_s$ and $m_l' = m_j' - m_s$ to get the final expression

$$\begin{aligned}\langle Y_{LM}\rangle =&(-1)^{l'}\frac{\hat{L}\hat{l}}{\sqrt{4\pi}}\begin{pmatrix} l' & L & l \\ 0 & 0 & 0\end{pmatrix}\sum_{m_s}\left(l'\,(m_j'-m_s)\,s\,m_s|j'\,m_j'\right)\left(l\,(m_j-m_s)\,s\,m_s|j\,m_j\right) \\ &\times\left(l\,(m_j-m_s)\,L\,(m_j'-m_j)\,|l'\,(m_j'-m_s)\right)\,. \end{aligned} \tag{A.12}$$

For the radial part, we focus on just the quadrupole moment, i.e. $L = 2$ and $\langle r^2 \rangle \equiv \langle n'\, l' | r^2 | n\, l \rangle$. The expression becomes

$$\begin{aligned} \langle r^2 \rangle &= \frac{N_{n'l'} N_{nl}}{2} b^3 \int \left(\frac{r^2}{b^2}\right)^{\frac{l+l'+3}{2}} e^{-\frac{r^2}{b^2}} L_n^{l+\frac{1}{2}} \left(\frac{r^2}{b^2}\right) L_{n'}^{l'+\frac{1}{2}} \left(\frac{r^2}{b^2}\right) \frac{2r}{b^2} dr \\ &= \frac{N_{n'l'} N_{nl}}{2} b^3 \int \rho^{\frac{l+l'+3}{2}} e^{-\rho} L_n^{l+\frac{1}{2}}(\rho)\, L_{n'}^{l'+\frac{1}{2}}(\rho)\, d\rho\,. \end{aligned} \tag{A.13}$$

We now consider the three cases of $\Delta L = 0, \pm 2$ and denote each case $\langle r^2 \rangle_{\Delta L}$. Beginning with $\Delta L = l' - l = 0$ (i.e.$\langle r^2 \rangle_0$), we have

$$\begin{aligned} \langle r^2 \rangle_0 =& \frac{N_{n'l'} N_{nl}}{2} b^3 \int \rho^{l+\frac{3}{2}} e^{-\rho} L_n^{l+\frac{1}{2}}(\rho)\, L_{n'}^{l+\frac{1}{2}}(\rho)\, d\rho \\ (A.1, A.3) \overset{\rightarrow}{=}& b^2 \left[(2n + l + \frac{3}{2}) \delta_{n,n'} - \sqrt{n(n + l + \frac{1}{2})}\, \delta_{n,n'+1} - \sqrt{(n+1)(n + l + \frac{3}{2})}\, \delta_{n,n'-1} \right]. \end{aligned} \tag{A.14}$$

For the case of $l' = l + 2$, Eq. A.13 becomes

$$\begin{aligned} \langle r^2 \rangle_{+2} =& \frac{N_{n'l'} N_{nl}}{2} b^3 \int \rho^{l+\frac{5}{2}} e^{-\rho} L_n^{l+\frac{1}{2}}(\rho)\, L_{n'}^{l+\frac{5}{2}}(\rho)\, d\rho \\ (A.1, A.2) \overset{\rightarrow}{=}& \frac{N_{n'l'} N_{nl}}{2} b^3 \int \rho^{l+\frac{3}{2}} e^{-\rho} \left(L_n^{l+\frac{3}{2}} - L_{n-1}^{l+\frac{3}{2}} \right) \left((n' + l + \frac{5}{2}) L_{n'}^{l+\frac{3}{2}} - (n'+1) L_{n'+1}^{l+\frac{3}{2}} \right) d\rho \\ (A.3) \overset{\rightarrow}{=}& b^2 \left[\sqrt{(n + l + \frac{5}{2})(n + l + \frac{3}{2})}\, \delta_{n,n'} - 2\sqrt{n(n + l + \frac{3}{2})}\, \delta_{n,n'+1} + \sqrt{n(n-1)}\, \delta_{n,n'+2} \right]. \end{aligned} \tag{A.15}$$

Naturally, the $\Delta L = -2$ case will be the same, but with n and l exchanged with n' and l', respectively:

$$\langle r^2 \rangle_{-2} = b^2 \left[\sqrt{(n' + l' + \frac{5}{2})(n' + l' + \frac{3}{2})}\, \delta_{n,n'} - 2\sqrt{n'(n' + l' + \frac{3}{2})}\, \delta_{n+1,n'} + \sqrt{n'(n'-1)}\, \delta_{n+2,n'} \right]. \tag{A.16}$$

Putting Eqs. (A.12), (A.14), (A.15) and (A.16) together, the electric quadrupole matrix elements is expressed

$$\langle \alpha' | Q_{LM} | \alpha \rangle = \langle Y_{2M} \rangle \cdot \frac{1}{4} \begin{cases} \langle r^2 \rangle_0 & \text{if } l' = l \,, \\ \langle r^2 \rangle_{+2} & \text{if } l' = l+2 \,, \\ \langle r^2 \rangle_{-2} & \text{if } l' = l-2 \,. \end{cases} \tag{A.17}$$

Note that when calculating the quadrupole moment (as opposed to an E2 transition matrix element), one also must include the factor $\sqrt{\frac{16\pi}{5}}$.

Magnetic dipole

The full derivation of the conventional magnetic dipole operator can be found in Refs. [3, 4]. For the purposes of this study, only the deuteron channel is required, for which the matrix elements may be calculated as (in implicit units of the Bohr magneton $\mu_B = \frac{e\hbar}{2m_p}$)

$$\langle \alpha' | \mu_{1M} | \alpha \rangle = \delta_{n,n'} \delta_{l,l'} \left[(K_p + K_n) m_j + (K_p + K_n - \frac{1}{2}) \sum_{\alpha} \sum_{\alpha'} \right] , \tag{A.18}$$

where $K_p = 2.792763 \pm 3.0 \cdot 10^{-5}$ and $K_n = -1.913148 \pm 6.6 \cdot 10^{-5}$ are the proton and neutron spin magnetic moments, respectively [5].

Allowed Gamow-Teller β^--decay

We express the many-body allowed GT β^--decay transition operator

$$\mathcal{M}_{GT}^{1\mu} = g_A \sum_{i}^{N} \hat{\tau}_+(i) \hat{\sigma}_\mu(i) \,, \tag{A.19}$$

with axial coupling constant $g_A = 1.25$, isospin raising operator $\hat{\tau}_+$ and spin operator $\hat{\sigma}_\mu$ operating on neutron i. Naturally, β^+-decay operator may be similarly defined for protons, though isn't necessary for our purposes.

Thus, we calculate allowed GT transition elements for the 2N system as

$$\langle \alpha' | M^{1\mu}_{GT} | \alpha \rangle = \delta_{n,n'} \delta_{l,l'} \delta_{m_l,m'_l} \frac{g_A}{\sqrt{4\pi}} \sum_{\alpha} \sum_{\alpha'} \langle s' m'_s | \langle t' m'_t | \left(\sum_{k}^{2} \hat{\sigma}_\mu(k) \hat{\tau}(k) \right) | t\, m_t \rangle | s\, m_s \rangle \,, \tag{A.20}$$

where the spin and isospin wavefunctions are expressed using Slater determinants as described in Section 2.2.

$0\nu\beta\beta$-decay from χEFT at NLO

We consider the $0\nu\beta\beta^-$-decay up to NLO under the χEFT-treatment defined in Ref. [6]. In the case of a ${}^1s_0$ di-neutron decaying to a ${}^1s_0$ di-proton, we express the relative 2N coordinate space operator as

$$O_{0\nu\beta\beta} = -6r \left(m_\pi r - 2 \right) e^{-m_\pi r} \,, \tag{A.21}$$

where m_π is the pion rest mass. Unlike the former operators, we evaluate the matrix elements in the HO basis through numerical integration.

References

[1] George Arfken. *Mathematical Methods for Physicists*. Academic Press, Inc., San Diego, third edition, 1985.

[2] Jouni Suhonen. *From Nucleons to Nucleus*. Theoretical and Mathematical Physics. Springer, Berlin, Germany, 2007. ISBN 9783540488613, 9783540488590. doi: 10.1007/978-3-540-48861-3. URL http://www-spires.fnal.gov/spires/find/books/www?cl=QC793.3.S8S84::2007.

[3] A. Bohr and B. Mottelson. *Nuclear Structure*, volume 1. World Scientific, Singapore, 1998.

[4] J.M. Eisenberg and W. Greiner. *Nuclear theory: Microscopic theory of the nucleus*. Cambridge University Press, North-Holland, 1976.

[5] Peter J. Mohr, David B. Newell, and Barry N. Taylor. CODATA Recommended Values of the Fundamental Physical Constants: 2014. *Rev. Mod. Phys.*, 88(3):035009, 2016. doi: 10.1103/RevModPhys.88.035009.

[6] Gary Prezeau, M. Ramsey-Musolf, and Petr Vogel. Neutrinoless double beta decay and effective field theory. *Phys. Rev.*, D68:034016, 2003. doi: 10.1103/PhysRevD.68.034016.